

**Electrically and Optically Detected
Electron Paramagnetic Resonance
in Blue Organic Light Emitting Diodes**

by

Rebecca Jane Sutton

A thesis
submitted to the Victoria University of Wellington
in fulfilment of the requirements for the degree of
Master of Science
in Physics

Victoria University of Wellington
2013

Abstract

Organic light emitting diodes (OLEDs) are an emerging technology based on electrically conducting polymer films, with great promise for large area lighting and flexible ultra-thin displays. However, despite the rapid technological development, there is still a poor understanding of the degradation and spin-dependent recombination processes that take place inside an OLED. In this thesis, Electron Paramagnetic Resonance (EPR) was used to investigate these processes in blue-emitting OLEDs.

A successful procedure was developed and refined for fabricating OLEDs with the structure ITO/PEDOT:PSS/emissive layer/Al/Ag, with and without the PEDOT:PSS hole-transporting layer. The organic emissive layer was either F8BT, PFO, or PVK:OXD-7:FIrpic (PB). These OLEDs were fabricated in air and with a geometry optimised for EPR experiments. Critical features for satisfactory devices were found to be a sufficiently thick organic layer and minimal exposure to the air.

A compact apparatus was developed for simultaneous light output, current, and voltage measurements on the OLEDs while in an inert glove box environment. Electroluminescence and current-voltage parameters measured for these devices showed predominantly trap-controlled space-charge-limited conduction.

OLEDs with PFO as the emissive layer and with a PEDOT:PSS layer were investigated with conventional, electrically-detected (ED) and optically-detected (OD) EPR techniques. EDEPR and ODEPR signals were observed at ~ 9.2 GHz and in the low (< 50 mT) and high (~ 330 mT) magnetic field regimes and were found to change markedly with time during operation as the device degraded. The low field signals initially showed a composite broad quenching and superimposed narrow enhancing response centred around zero field strength. These signals were attributed to magneto-resistance (MR) and magneto-electroluminescence (MEL). Following operational ageing, a third, narrow quenching line was observed in the MR and the ratio of the initial two MR responses changed substantially. These effects are tentatively attributed to a hyperfine interaction. For both EDEPR and ODEPR, quenching high field resonances with a g -value (gyromagnetic ratio) of 2.003 ± 0.001 were observed. The current-quenching resonance gradually diminished during operation and after 4–5 hours was replaced by a current-enhancing resonance. The appearance of this latter resonance could be explained by chemical changes in the OLED due to the diffusion of oxygen through the device from the oxygen-plasma-treated ITO. A working model is proposed which can explain this observed change as spin-dependent trapping and recombination at free radicals, although the model requires further experimentation to test its validity.

Acknowledgements

I would like to express my very great appreciation to my supervisors Associate Professor Dr. Andy Edgar and Dr. Natalie Plank for their invaluable advice, patient guidance, and constructive critiques of this research.

I would also like to thank Dr. Justin Hodgkiss for valuable discussions and insight. I am particularly grateful for the assistance provided by Rod Brown, Peter Coard and David Stead, and the excellent workshop team at the School of Chemical and Physical Sciences. Special thanks are extended to Peter Moore for redrawing the chemical structures found in this thesis, and to Nicola Winch and Laura Dixie and my colleagues in the cleanroom for useful discussions and helpful tips.

I wish to acknowledge the researchers at the Technical University of Darmstadt, who provided yellow and red OLEDs, specifically Prof. Heinz von Seggern, Gabi Andrees, and Dr. Andrea Gassmann. I am also grateful to Prof. Seggern for informative and inspiring discussions.

I am especially grateful to my family and friends for their constant love and encouragement, and to my gracious God for the strength and wisdom needed to overcome the many challenges encountered in this project.

This project was funded by Victoria University of Wellington and The MacDiarmid Institute for Advanced Materials and Nanotechnology.

Contents

1	Introduction	1
2	Spin-Dependent Charge Transport in Organic Light Emitting Diodes	7
2.1	Operating Principle and Charge Transport Mechanisms	7
2.1.1	Charge Injection and Transport	8
2.1.2	Exciton Formation	10
2.1.3	Exciton Recombination	11
2.2	Spin-dependent Recombination Models	12
2.2.1	Models Developed for Inorganic Semiconductors	13
2.2.2	Models Proposed for Organic Semiconductors	18
3	Background to Electron Paramagnetic Resonance (EPR)	23
3.1	Conventional EPR	23
3.2	Electrically- and Optically-Detected EPR	25
3.3	Effects at Low Magnetic Fields	27
3.4	Previous Studies using EPR Techniques	29
3.4.1	Electrically- and Optically-Detected EPR Studies of Polymer OLEDs	30
3.4.2	Studies on Blue-Emitting PFO OLEDs	32
3.5	Degradation in OLEDs	33
4	Equipment	37
4.1	Light-Current-Voltage Tracer	37
4.1.1	The Electronic Circuit	38
4.1.2	LabVIEW Program	40
4.1.3	Capabilities of the LIV Tracer	41

4.2	Electroluminescence, Current, and Voltage Measurements . . .	44
4.3	EPR Spectrometer	45
5	OLED Fabrication and Characterisation	53
5.1	A Brief Overview of OLED Fabrication	53
5.2	Device Fabrication	56
5.2.1	Substrate and Anode Preparation	58
5.2.2	Hole-Transporting Layer	59
5.2.3	Emissive Layers	60
5.2.4	Cathode	65
5.2.5	Comments on OLED Fabrication	66
5.3	OLED Characterisation	66
5.3.1	Electroluminescence	66
5.3.2	Current-Voltage Characteristics	69
5.3.3	Electroluminescence-Voltage Characteristics	72
5.3.4	Time-dependent Decay	74
5.4	Chapter Summary	76
6	Electrically and Optically Detected Electron Paramagnetic Resonance in PFO OLEDs	77
6.1	Results	78
6.1.1	Comparison of EPR Techniques	78
6.1.2	Effect of Microwave Power	80
6.1.3	Effect of Ageing	82
6.1.4	Electroluminescence of the Aged OLED	86
6.1.5	Analysis of the Low Field Signals	87
6.1.6	Summary	88
6.2	Discussion	89
6.2.1	The High Field Signal at $g = 2$	89
6.2.2	A Possible Spin-Dependent Mechanism	90
6.2.3	The Low Field Signal Near $B = 0$	92
7	Conclusions	95
7.1	Summary	95

7.2	Further Work	98
7.3	Outlook	101
A	LIV Tracer: Design Details	103
A.1	Sample Holder Design	103
A.2	Electronic Circuit Block Diagram	105
A.3	LabVIEW Program for the LIV Tracer	105
B	OLED Fabrication: Spin Coating, Problem Solving and Final Process	109
B.1	Spin-Coating	109
B.2	Problem Solving	110
B.3	OLED Fabrication Process	110
B.3.1	Substrate Preparation	111
B.3.2	Hole Transport Layer	112
B.3.3	Emissive Layer	112
B.3.4	Cathode	113
B.3.5	Contacts	113

List of Figures

1.1	Simplified schematic of operation of organic light-emitting diodes (OLEDs)	2
1.2	Theory of electron paramagnetic resonance	3
2.1	More detailed schematic of OLED operation	8
2.2	A configuration-coordinate diagram for exciton formation	11
2.3	Lépine's spin-dependent recombination mechanism	13
2.4	Kaplan, Solomon and Mott's spin-dependent recombination mechanism	15
2.5	Spin-dependent Shockley-Read-Hall recombination mechanism	17
2.6	Electron-hole binding energy as a function of separation distance	19
2.7	Boehme and McCamey's recombination mechanism	20
3.1	Example EPR spectrum	24
3.2	Experimental set-up for EDEPR and ODEPR	26
4.1	Photographs of the Light-Current-Voltage (LIV) Tracer	38
4.2	The electronic circuit used in the LIV tracer	39
4.3	The interactive front panel of the LIV Tracer LabVIEW program	41
4.4	Simultaneous electroluminescence- (EL-) and current-voltage data collected by the LIV Tracer	42
4.5	Experimental set-up for point-by-point simultaneous measurements of EL intensity, current density, and voltage	45
4.6	Experimental set-up for time-dependent measurements of EL intensity and current density	45
4.7	Photograph of EPR spectrometer.	46

4.8	Photograph of EPR cavity	47
4.9	A block diagram for the EPR spectrometer	50
4.10	Determination of quenching nature of electrically- and optically- detected EPR signal	52
5.1	Chemical structures for the emissive materials	55
5.2	OLED layers: top view	57
5.3	Photograph of finished OLED	57
5.4	OLED layers: cross section	58
5.5	PEDOT:PSS chemical structure	59
5.6	PEDOT:PSS ridge	60
5.7	Energy level diagram for the phosphorescent OLED	62
5.8	Determination of film thickness for the phosphorescent material	63
5.9	Energy level diagram for the fluorescent OLEDs	64
5.10	Determination of film thickness for the fluorescent materials . .	64
5.11	Cathode patterns	65
5.12	Electroluminescence spectra	67
5.13	Possible keto defect formation	68
5.14	Photographs of blue-emitting OLEDs	68
5.15	Photograph of a yellow-emitting OLED	68
5.16	Current-voltage data for the blue-emitting OLEDs	69
5.17	Electroluminescence-voltage and simultaneous current-voltage data for the blue-emitting OLEDs	73
5.18	Decays of the current density and EL intensity over time, with constant driving voltage	75
6.1	Spectra of a PFO OLED with various EPR techniques	79
6.2	EDEPR and ODEPR signals for different microwave powers . .	80
6.3	Microwave power dependence of EDEPR and ODEPR signal magnitudes for a PFO OLED	81
6.4	Time-sequence of EDEPR spectra during operational ageing of a PFO OLED	82

6.5	Electrically-detected peak-to-peak magnitudes and widths, and integrated area during operational ageing.	83
6.6	EDEPR and ODEPR spectra of a PFO OLED post operational ageing	84
6.7	EDEPR and ODEPR spectra of an operationally aged PFO OLED post one week of storage in a nitrogen glove box	85
6.8	Electroluminescence spectra of new and aged PFO OLEDs.	86
6.9	Fits to Low Field Signal	87
6.10	A possible spin-dependent recombination mechanism	91
A.1	A mechanical design for the LIV Tracer OLED holders	104
A.2	The light collection geometry for the LIV Tracer	104
A.3	Photographs of the LIV Tracer OLED holders	105
A.4	Block diagram for the LIV Tracer electrical circuit	105
A.5	A block diagram of the LabVIEW program for the LIV Tracer	106
B.1	Spin-Coater	109

List of Tables

1.1	Typical operating lifetimes of OLEDs	4
4.1	Experimental settings for EPR, EDEPR and ODEPR.	49
5.1	Fitting parameters for J-V data to trap-limited conduction	71
5.2	Fitting parameters for EL-V data to trap-limited conduction . .	73
6.1	Lorentzian decomposition of low field signal	88
B.1	Device fabrication trouble-shooting	110

Glossary

B	Magnetic field, in Tesla
Bipolaron	Bound pair of two polarons with like charge and their associated lattice distortion
EDEPR	Electrically-detected EPR; the resonance is detected as a change in conductivity
EL	Electroluminescence; light emission in response to electric current in a material
EPR	Electron paramagnetic resonance spectroscopy; a measurement technique that uses the resonance of microwave energy with the Zeeman splitting of unpaired electrons
F8BT	Poly[(9,9-dioctylfluorenyl-2,7-diyl)-co-(1,4-benzo-(2,1,3)-thiadiazole)]; A fluorescent yellow-emitting polymer which is a close relative of PFO
Firpic	(Bis-(3,5-difluoro-2-(2-pyridyl)phenyl-(2-carboxypyridyl)-iridium(III)); A phosphorescent blue-emitting dopant molecule
Hole	The absence of an electron which behaves like a positive charge
HOMO	Highest (energy) occupied molecular orbital, analogous to the conduction band in inorganic semiconductors
IPA	Isopropyl alcohol or isopropanol, a solvent commonly used for cleaning
ISC	Inter-system crossing (for example transitions between singlet and triplet spin states)
ITO	Indium tin oxide, a transparent conductor

LIV Tracer	A measurement apparatus developed in this project to simultaneously measure light output (L), current (I), and voltage (V)
LUMO	Lowest (energy) unoccupied molecular orbital, analogous to the valence band in inorganic semiconductors
MEL	Magneto-electroluminescence; Changes in the electroluminescence due to changes in the magnetic field
MR	Magneto-resistance; Changes in the sample resistance due to changes in the magnetic field
ODEPR	Optically-detected EPR; here the resonance is detected as a change in the light output
OLED	Organic light emitting diode
OXD-7	(1,3-bis((4-tert-butyl-phenyl)-1,3,4-oxiadiazolyl)phenylene); An electron-transporting molecule
PB	A phosphorescent blue-emitting polymer solution containing Flrpic, OXD-7 and PVK
PEDOT:PSS	Poly(2,3-dihydrothieno-1,4-dioxin)-poly(styrenesulfonate); A conducting polymer used to improve hole-injection into the light-emitting layer
PFO	Poly(9,9-di-n-octylfluorenyl-2,7-diyl); A fluorescent blue-emitting polymer in the polyfluorene family
PL	Photo-luminescence; light emission in response to incident light on a material
Polaron	A charged species (electron or hole) and its lattice distortion
PPV	Poly(<i>p</i> -phenylene vinylene); A normally yellow light-emitting fluorescent polymer with many derivatives, including red- and green-emitting polymers
PVK	Poly-(9-vinylcarbazole); A hole-transporting blue-emitting polymer commonly used as a host material in phosphorescent OLEDs
VUW	Victoria University of Wellington, New Zealand

Chapter 1

Introduction

Organic Light Emitting Diodes (OLEDs) are a class of electroluminescent device in which the light-emitting material is an organic thin film sandwiched between two conducting electrodes. A schematic of OLED operation is presented in Figure 1.1. When an appropriate voltage is applied across an OLED, electrons are injected into the Lowest Unoccupied Molecular Orbital (LUMO) of the organic molecule, analogous to the conduction band in an inorganic semiconductor LED, and holes¹ are injected into the Highest Occupied Molecular Orbital (HOMO), which is analogous to the valence band in an inorganic semiconductor LED. The process of electron-hole recombination releases the excess energy as visible light and/or heat.

This thesis is concerned with the application of electron paramagnetic resonance (EPR) measurement techniques to OLEDs. In particular it addresses the question of whether EPR can reveal any information about the ageing processes which result in reduction of the level of light emission in OLEDs.

EPR involves the interaction between the magnetic moment (or 'spin') of an

¹A hole is defined as the absence of an electron.

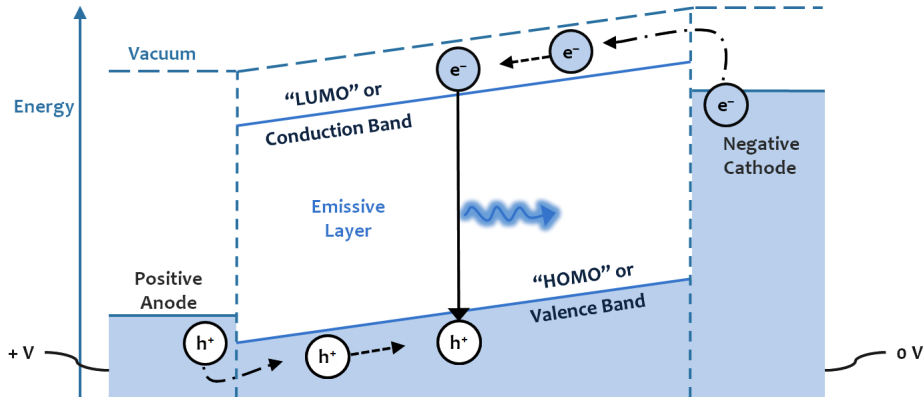


Figure 1.1: A schematic of OLED operation. See text for details.

electron in a magnetic field and incident microwave radiation. The simplest example is the resonance of a single unpaired spin, as illustrated in Figure 1.2. In the presence of a static magnetic field B , the electron spin aligns either parallel or antiparallel with the field. There is an energy difference ΔU between these two alignments, which depends on the magnetic field strength. When the energy of the microwave radiation matches this difference, the electron may absorb some of the microwave energy and switch between the spin alignments, i.e. undergo a 'spin flip transition'. This occurs when the resonance condition is satisfied, as follows:

$$\Delta U = U_{\downarrow} - U_{\uparrow} = g\beta_e B_r = h\nu \quad (1.1)$$

where g is the gyromagnetic ratio (Zeeman splitting constant or more commonly " g -value") of the unpaired electron, $\beta_e = |e|\hbar/2m_e$ is the Bohr magneton, B_r is the resonant magnetic field, h is Planck's constant, and ν is the frequency of microwave radiation. In an EPR experiment, these spin flip transitions are detected and may be analysed to reveal information about the environment surrounding the unpaired electrons.

Conventional EPR measures changes in microwave absorption. This method of detection requires a minimum of 10^{11} unpaired electron spins for a 1 Gauss

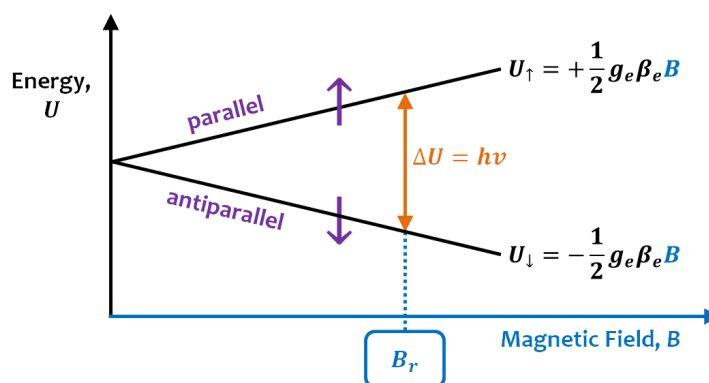


Figure 1.2: Energy-level splitting and resonant microwave absorption of a single electron in an applied magnetic field. Mathematical symbols are explained in the text. Adapted from [1]

(100 μT) wide EPR line with a signal to noise ratio of 1:1 [2]. A typical OLED is made of a thin film of organic material which contains $\sim 6 \times 10^{11}$ molecules², some of which contain an unpaired spin. Hence conventional EPR lacks the sensitivity required for studying OLEDs.

However the particular processes which are of interest, specifically the radiative and non-radiative recombination processes, are spin-dependent. Changes in these processes due to EPR lead to changes in the current and light emission, which may be detected electrically and optically. This thesis makes use of these alternative techniques to study OLEDs and their degradation.

The degradation of blue-emitting OLEDs is of significant scientific and practical interest, as understanding the processes limiting the OLED lifetime is of key importance in developing longer-lasting OLEDs. Blue OLEDs have the shortest lifetime of any of the available colours, and are the limiting factor in polychromatic displays.

OLED research is leading to increased lifetimes but these are still below the performance required for general lighting applications, which is 100 lm/W with 50,000+ hour lifetimes [3,4]. Lifetimes reported by leading OLED dis-

²For a polymer with molecular weight of 10^6 and density of $\sim 1\text{--}2 \text{ g cm}^{-3}$ in a film with dimensions $100 \text{ nm} \times 10 \text{ mm} \times 1 \text{ mm}$.

play companies Cambridge Display Technology (CDT) and Universal Display Corporation (UDC) are presented in Table 1.1.

Colour	CDT (2011)	UDC (2012)
Deep Red	352	250
Red	200	900
Green	200 (F), 236	400
Light Blue	34 (N)	20
Deep Blue	21 (N)	–

Table 1.1: Operating lifetimes in thousands of hours to half brightness from 1,000 cd/m². (F) fluorescent emitter, (N) not specified, all others are phosphorescent emitters. From [5,6].

The colour of OLED emission is determined by the chemical structure of the emitting organic molecules. With the great range of organic molecules available, OLEDs have been fabricated for every colour in the whole visible spectral range [7]. ‘White’ emission is then possible with the combination of several molecules, such as blue, green and red emitters, or blue and orange emitters, either in the same OLED or in neighbouring OLED pixels. However, as illustrated by Table 1.1, the lifetime performance of blue OLEDs is significantly lower than that of red and green OLEDs. The limited lifetimes are in part due to the susceptibility of the organic materials to degradation by oxygen and water. Hence designing effective protective encapsulation layers is an area of ongoing research, especially for flexible devices [3].

Despite this current limitation, OLEDs are an emerging technology with many advantages over rival technologies for lighting and display applications. For example OLED displays have excellent colour resolution, are brighter than the competing LCD and plasma technologies and have much better on-off contrast. This is in part due to the ‘true’ black: absolutely no light is emitted when a pixel is black, giving a deep black and consuming no power. In contrast, a backlit LCD display makes use of the imperfect polarisation of liquid

crystals and cannot block the light completely, limiting the light-dark contrast. Further, OLED displays require no background illumination, and few (if any) filters. OLED displays have response times “1,000 times faster than LCD” [8]. They are also thin and light, and have a viewing angle of nearly 180° [3,7].

There are two types of OLED which differ in their theoretical efficiency: fluorescent OLEDs can convert up to 25% of the electrical energy into light, whereas phosphorescent materials have the potential to convert up to 100% (any remaining energy is lost as heat in the device) [9]. Compared to other light sources, OLEDs are power- and cost-efficient³, which makes them ideal for large-scale lighting and displays [10,11]. OLED displays can consume “substantially less power” than current LCDs in cellphone and TV applications [5,12] and are already being used by several companies⁴. Also, the organic materials are non-toxic and environmentally-friendly [5].

Two promising features of OLEDs are that they can be made on flexible substrates which can be bent, or even rolled up into a tube, and they can be made virtually transparent [3,5,12]. In addition, these transparent OLEDs could be coupled with organic photovoltaic technology to provide a display that harvests sunlight during the day, and then provides lighting during the night. These two technologies are closely related, and easily compatible, as an organic photovoltaic device is effectively an OLED in reverse.

With these exciting applications of OLEDs, the investigation of degradation processes is an important and fascinating area of research. This thesis shows that EPR techniques may be used to study the degradation of blue OLEDs and

³The cost of OLED production is predicted to decrease as the technology matures [5].

⁴This year (2013) LG is offering a 55” high-definition OLED TV with 100,000,000:1 contrast ratio and which is 4 mm thick and 3.5 kg in weight [8,12]. This TV is based on a white OLED backlight with colour filters. In competition, Samsung has promised to release a 55” ‘Real’ OLED TV with red, green and blue OLED pixels. OLED displays are already used in some mobile phones, for example the 5.5” Samsung Galaxy Note 2 [13].

provides valuable insight into these degradation processes. The application of the EPR technique to OLEDs relies on spin-dependent charge transport and recombination in the OLEDs, which will be discussed in Chapter 2. Chapter 3 provides a more detailed discussion of the electron paramagnetic resonance technique and a review of the relevant literature. The experimental apparatus is presented in Chapter 4; details of the development of OLED fabrication, a task which had not previously been undertaken at VUW, and the subsequent device characterisation are provided in Chapter 5. Chapter 6 then presents the results of an EPR study on fluorescent polymer bilayer OLEDs. The thesis concludes with a summary of the results and suggestions for further work in Chapter 7.

Chapter 2

Spin-Dependent Charge Transport in Organic Light Emitting Diodes

This chapter outlines the principles of OLED operation, with a particular focus on spin-dependent transport. The discussion which follows draws on recent reviews of OLED operation, for example the “Organic Electronics Primer” [14], and of spin-dependent charge transport, including reviews and/or books by Schworer and Wolf [7], Lupton, Boehme and McCamey [15,16], Shinar *et. al.* [17], and Spaeth and Overhof [18].

2.1 Operating Principle and Charge Transport Mechanisms

There are four fundamental processes occurring within the OLED during operation. These are summarised in the energy-level diagram in Figure 2.1 and discussed further in the text.

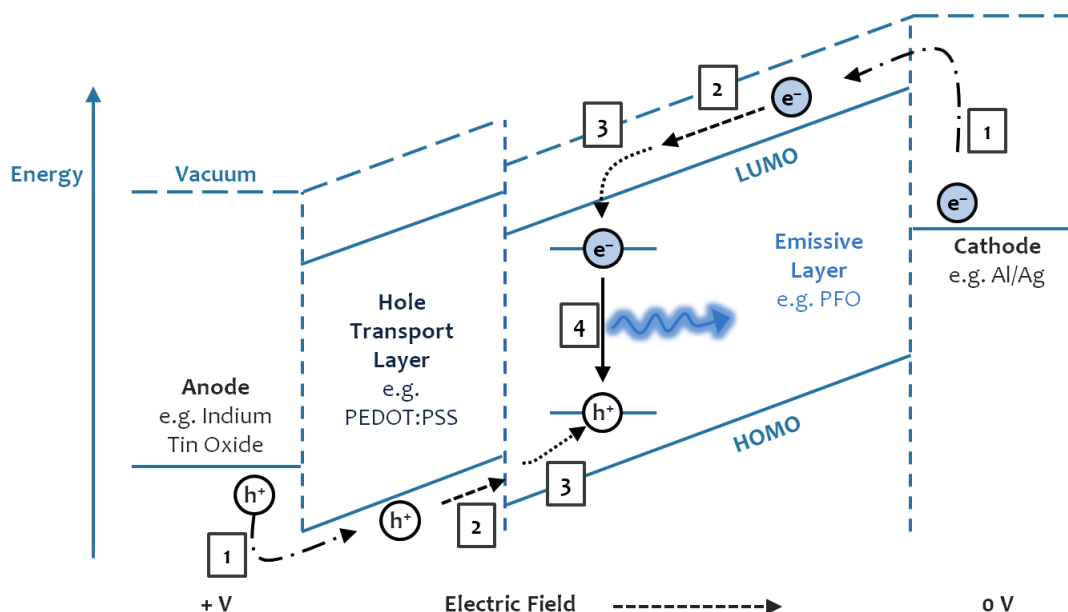


Figure 2.1: The structure and schematic energy diagram of a working (forward biased) two-layer OLED showing the four processes of 1 charge injection and 2 transport, 3 binding to form excitons, and 4 recombination accompanied by light emission. This diagram was adapted from [7].

The energies of the HOMO (Highest Occupied Molecular Orbital) and LUMO (Lowest Unoccupied Molecular Orbital) relative to the vacuum level depend upon the work functions of the metal electrodes, and the applied electric field, and so depend upon position within the emissive layer, as shown in Figure 2.1. The example materials are those used for the two-layer fluorescent blue-emitting OLED fabricated at VUW. Other layers of electron-transporting, electron-blocking, hole-transporting, and/or hole-blocking materials may also be included to improve the charge transport, and thus the OLED performance.

2.1.1 Charge Injection and Transport

To inject charge (electrons and holes) into the organic layers, an operating voltage sufficient to overcome any potential energy barriers at the organic-metal interfaces is required. Given this voltage, electrons and holes are then injected

into¹ and driven through the organic polymer layers by the electric field between anode and cathode. Within a molecule, charges move relatively freely due to π -conjugation. However the polymer layer is mostly disordered so the charges must 'hop' from one molecule to another. The coupling between molecules is material-dependent, but generally weak (van der Waals) for polymers, resulting in low hopping mobilities. Electron and hole mobilities are typically 10^{-5} to 10^{-2} $\text{cm}^2 \text{V}^{-1} \text{s}^{-1}$ [19], which are much smaller than those for typical inorganic semiconductors (e.g 1500 and 450 $\text{cm}^2 \text{V}^{-1} \text{s}^{-1}$ for electrons and holes in silicon respectively [20]).

As the electrons and holes move through the organic polymer material, each charge forms an electronic polarisation around it which distorts the lattice. This localisation of the charge causes a local upward shift of the HOMO and downward shift of the LUMO energy levels corresponding to the elastic energy of the distortion. Together the charge with its lattice distortion is known as a 'polaron' [7,21].

A pair of like charges and their local lattice distortion may come together to form a 'bipolaron'. A bipolaron is thus analogous to the Cooper pair in BCS theory [21]. Bipolaron formation requires the Coulomb repulsion to be less than the energy gained by the additional lattice distortion. The combination of two spin- $1/2$ particles forms spin-0 and spin-1 bipolarons; spinless (spin-0) bipolarons have a lower energy so are the dominant form. Note that microwave radiation can have no effect on a spinless bipolaron.

Electrons or holes may also become trapped in regions where the polarisation energy is relatively high, for example at defects or impurities such as dopant molecules. These are known as shallow or deep traps, where the captured

¹Electrons and holes are injected at the same rate for steady state conditions, in a fully bipolar device [7]

charges can or cannot escape by thermal activation respectively [7]. The energies of these traps may lie slightly above the HOMO or slightly below the LUMO energy levels, corresponding to the acceptor and donor levels in inorganic semiconductors.

2.1.2 Exciton Formation

The association of an electron and a hole and the surrounding lattice distortion form an elementary excitation called an 'exciton'. The exciton has a binding energy due to the Coulomb attraction between the electron and hole; the exciton energy states lie within the HOMO-LUMO gap, as shown in Figure 2.1.

For organic semiconductors the electron and hole tend to be localised on individual molecules [22], and often at defect or impurity molecules, forming 'bound' excitons. These highly localised excitons are known as Frenkel excitons. When the bound charges are delocalised over adjacent molecules this is known as a charge transfer exciton [19]. The location of exciton formation in an OLED device depends on the relative electron and hole mobilities and layer thicknesses, and can be near the cathode (high hole mobility) or near the anode (high electron mobility) or somewhere in between [7].

In the absence of a magnetic field there are equal populations of spin-up and spin-down electrons, and likewise for holes. Thus weakly bound excitons are formed in roughly equal combinations of parallel and antiparallel spins. The two spin- $1/2$ polarons of opposite charge may form excitons in the singlet spin-0 or triplet spin-1 states, so named because there is one spin-0 state and three spin-1 substates. Hence the population of triplet excitons is typically three times the singlet exciton population.

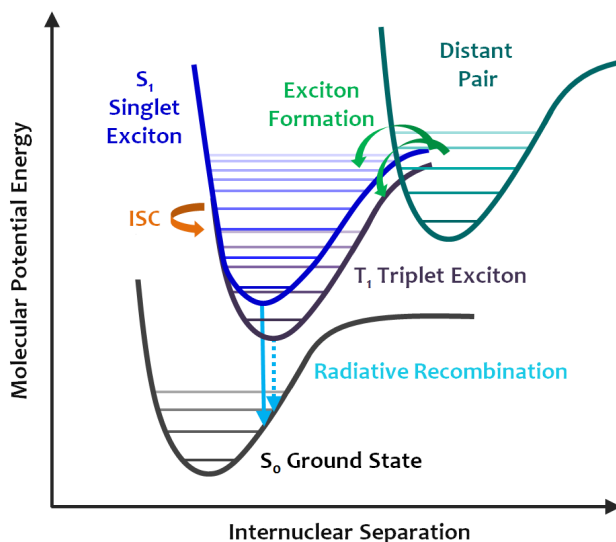


Figure 2.2: A configuration-coordinate diagram showing exciton formation from two distant charges, then subsequent radiative decays as per the Franck-Condon principle (see [23] and [24]). Intersystem crossing (ISC) transitions between triplet and singlet excitonic states are possible in cases of large spin-orbit coupling.

2.1.3 Exciton Recombination

The key transition for OLEDs is exciton recombination, where the electron recombines with the hole and gives off the excess energy as (at least) one photon. The radiative processes are illustrated in Figure 2.2. There are also many non-radiative recombination pathways (internal conversion processes) which are not shown, for example energy loss as heat through vibrational modes in the organic polymer.

Recombination from the singlet state (solid arrow) is permitted by the Pauli principle and is known as fluorescence. This process is the main radiative process for most π -conjugated polymers, such as the polyfluorenes. As fluorescence is spin allowed, this process occurs rapidly, with typical fluorescence lifetimes of $\sim 10^{-9}$ s [17].

Recombination from the triplet exciton state to the singlet ground state (dashed arrow) is known as phosphorescence. This radiative pathway is usually forbid-

den due to spin conservation. However spin-orbit interactions can cause some mixing of singlet states into the triplet states so that there is a small probability of a triplet-singlet transition [25]. Phosphorescence is therefore much slower than fluorescence, with phosphorescent lifetimes of at least $\sim 10^{-4}$ s [7].

The magnitude of spin-orbit coupling increases with increasing nuclear charge, Z [26]. Hence for some materials with large Z , the spin-orbit coupling is sufficiently large that phosphorescence is partially allowed. An important example is the heavy metal atom chelates, such as Ir(III) complexes. These chelates have extremely high (nearly 100%) inter-system crossing (ISC) efficiency from the singlet excitonic state to the triplet excitonic state, so phosphorescence is the dominant radiative process [17]. The efficiency of this phosphorescent radiation is the primary reason for the concerted research effort on phosphorescent OLEDs.

2.2 Spin-dependent Recombination Models

Excitonic recombination is intrinsically spin-dependent and therefore can be affected by any process such as electron paramagnetic resonance which changes the relative spin populations prior to recombination. How these processes cause changes in measurable properties such as the light emission and overall conductivity of an OLED was first discussed in the context of inorganic semiconductors. Hence several models of spin-dependent recombination that were developed for inorganic semiconductors will be briefly summarised here as they form the basis for a subsequent discussion of related models for organic materials.

2.2.1 Models Developed for Inorganic Semiconductors

The Lépine Model

Lépine² proposed a model of spin-dependent recombination in the early 1970's, based on a previous Shockley-Read-Hall model [28,29]. His model considers a recombination centre with an unpaired electron which can first capture a conduction electron, and then a hole, or vice versa. The initial capture of an electron (or hole) depends on the relative orientation of the conduction electron spin and the recombination centre spin, as the final state must be a singlet state, according to Pauli's principle. The second capture process is spin-independent since the result of the first capture is a singlet state. This mechanism is illustrated in Figure 2.3. The capture cross section Σ for an electron should then be of the form $\Sigma = \Sigma_0(1 - pP)$ where Σ_0 is the spin-independent capture cross-section, and p and P are the relative spin polarisations³ of the conduction electron and recombination centre respectively.

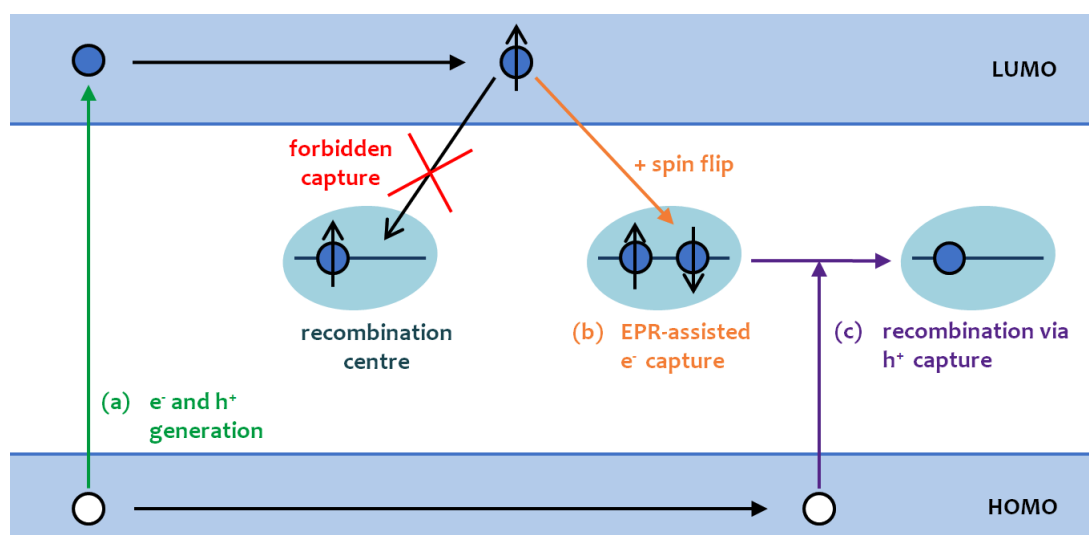


Figure 2.3: A schematic of the spin-dependent recombination mechanism proposed by Lépine. Adapted from [18].

²Lépine observed a decrease in the photoconductivity of a pure silicon sample at ~ 330 mT with ≈ 9.3 GHz microwaves (see [27]).

³The spin polarisation is defined as the difference in (field induced) spin state populations, divided by the total spin population.

In the presence of an external magnetic field, most of the conduction and recombination centre electrons orient themselves parallel with the field, corresponding to the lowest energy Zeeman levels. In the limiting case of zero Kelvin, *all* of the conduction electrons and the recombination centres are parallel spin oriented and so the capture cross section is small. Electron paramagnetic resonance then pumps the populations of one spin or the other, depending on the resonant field strength, into an antiparallel spin configuration. Thus the capture cross section increases, which reduces the population of conduction electrons and so decreases the conductivity, giving rise to an EPR signal which may be detected by measuring the conductivity.

Detailed analysis shows that Lépine's model predicts that the relative change in conductivity will be proportional to $(B_0/T)^2$, where B_0 is the strength of the external magnetic field and T is the absolute temperature in Kelvin [18]. However for organic as well as inorganic materials neither the field dependence nor the temperature dependence have been experimentally realised, and the relative changes tend to be one to two orders of magnitude larger than predicted by this model [30,31].

The Kaplan, Solomon and Mott (KSM) Model

In 1978 Kaplan, Solomon and Mott [31] presented an 'intermediate pair' model that assumes the electrons and holes are captured at recombination centres *independent of their spin orientation* to form electron-hole pairs. Recombination is then only allowed for pairs with antiparallel spins, i.e. pairs in the singlet configuration, so these pairs will be short-lived and in the steady state most electron-hole pairs will be in the triplet configuration. These triplet pairs can only recombine if an external stimulus such as microwave radiation causes a

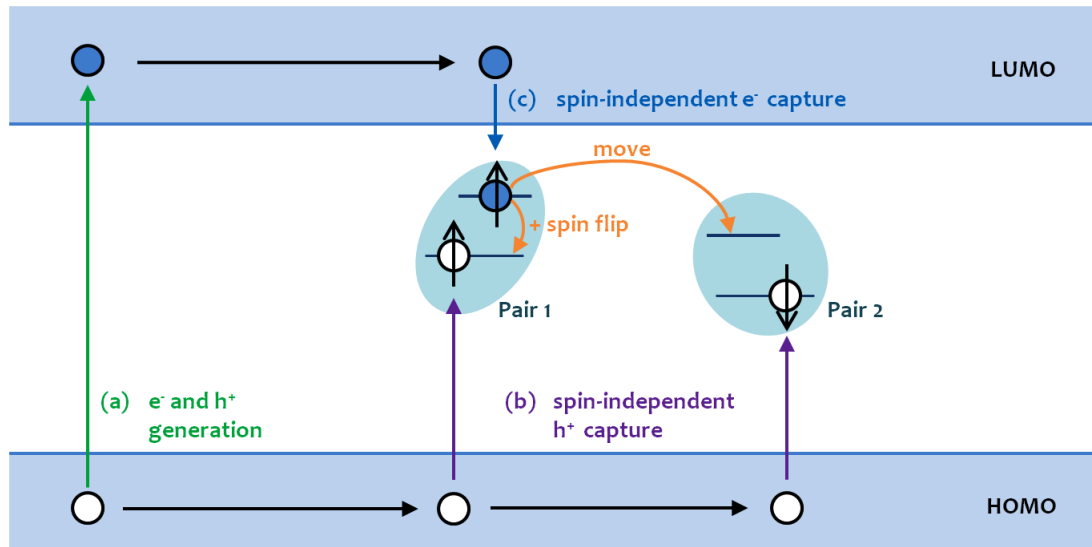


Figure 2.4: A schematic of the KSM model of spin-dependent recombination. The electron and hole at Pair 1 require a spin transition of either the electron or the hole in order to recombine. Alternatively the electron could move to another recombination centre, e.g. to form Pair 2 with a hole of antiparallel spin such that recombination is permitted. Adapted from [30] and [18].

spin flip transition, or if the pair dissociates and finds another electron or hole with which to recombine. This is illustrated in Figure 2.4.

A key assumption of this model is that the recombination rate is much faster than the spin lattice relaxation rate, so that the triplet state population is relatively large. The overall recombination rate depends only on the relative populations of singlet and triplet electron-hole pairs, and is not dependent on the polarisation of the electrons or holes. The recombination rate is also field independent, in agreement with experiment [18]. Indeed, Kaplan, Solomon and Mott noted that “the relative variation [in conductivity] can be as large as 10%, and is field independent as confirmed by experiment” [31].

A further investigation of pair formation in this model shows some possible problems [32]. Spaeth [18] comments that the observation of (ground state) EDEPR is inconsistent with electron-hole recombination at a single defect, since this would involve (excited state) excitons. However Solomon later clarified that the electron would be trapped at a donor and the hole at an acceptor to

form a close-proximity electron-hole pair, and so this is essentially a donor-acceptor recombination model [33]. But neither the electron nor the hole can be at a shallow trap, as emission rates in silicon are much faster than commonly-observed recombination rates [32]. Rather, the electron and hole must be trapped at a deep donor and acceptor in close proximity with one another in order for the electron-hole pair to recombine. Depending on the degree of proximity, this may lead to a large exchange interaction energy separating the singlet and triplet states, which will typically be larger than that provided by standard microwave frequencies [32]. However we note that this argument may not apply to polymeric materials where the spins may be located on neighbouring but distinct molecules with quite different exchange interactions to 'single molecule' silicon.

The Spin-Dependent Shockley-Read-Hall Model

A refined model was later proposed by Rong *et. al.* in 1991 [32] to avoid some of the inconsistencies of the KSM model. Like the Lépine model, the Spin-Dependent Shockley-Read-Hall model involves a recombination centre with an unpaired spin, and, like the KSM model, spin-independent capture of an electron and hole occurs at this recombination centre. However, here the electron is first captured in a spin-independent way into an excited state of the recombination centre (possibly a charge transfer state). The recombination with the unpaired spin of the recombination centre is then spin-dependent, as this process is subject to the Pauli principle. The recombination process is completed by the subsequent spin-independent capture of a hole. In contrast to the previous models, Rong *et. al.* introduce the idea of a 're-adjustment time', $t_{readjust}$, which is the time the conduction electron spends in the excited

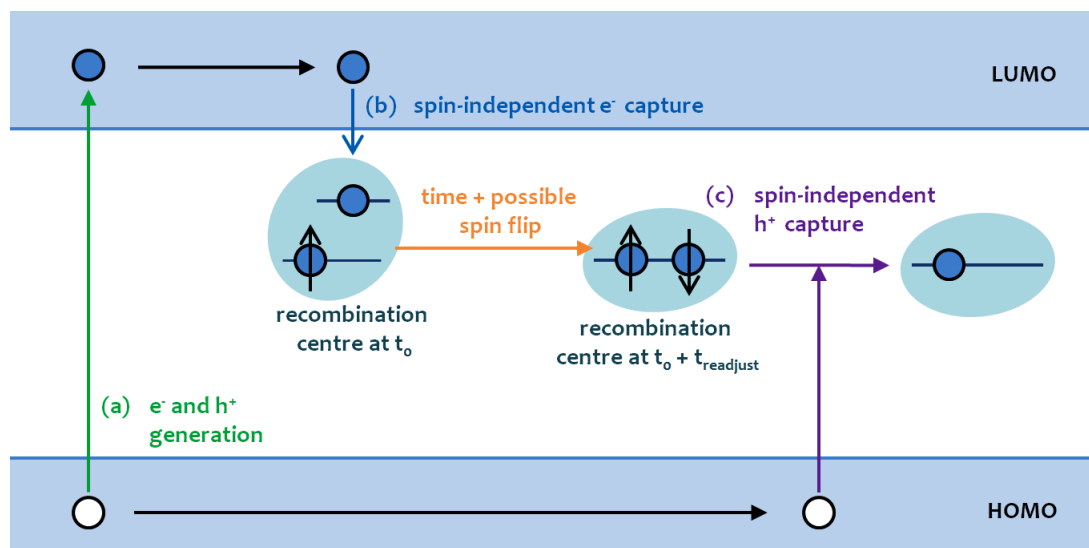


Figure 2.5: A schematic of the Spin-Dependent Shockley-Read-Hall model of spin-dependent recombination. See text for details. Adapted from [32] and [18].

state of the recombination centre before spin-dependent recombination into the ground state. This model is shown in Figure 2.5.

Note that the readjustment time depends on the relative spin orientations of the recombination centre and the captured electron. A captured electron of parallel spin to the unpaired electron in the recombination centre has a significantly longer readjustment time than one with antiparallel spin. As for the triplet electron-hole pair in the KSM model, during this longer readjustment time the captured electron may undergo a spin flip transition, e.g. due to microwave absorption, or be released back into the conduction band.

A significant aspect of this model is that both electron and hole capture occur at the same defect or impurity site without the potential inconsistencies of the KSM model.

In principle, the trapped conduction electron in the excited state of the recombination centre should have a characteristic spin resonance. However this has not been observed experimentally. Rong *et. al.* suggest that this may be due to

fast spin-lattice relaxation such that the overall resonance would be too broad for individual resonances to be observed.

2.2.2 Models Proposed for Organic Semiconductors

A key difference between inorganic and organic semiconductors is the formation of bipolarons in organic semiconductors. This opens up many more recombination mechanisms, such as spin-dependent bipolaron formation and annihilation of triplet and singlet excitons by bipolarons. Many models have been proposed for spin-dependent recombination in organic semiconductors, of which two currently favoured models will be presented here. The first model is similar to the models above for inorganic semiconductors and is based on polaron pair formation and spin-dependent recombination. The second model is more complicated and involves mechanisms such as the formation of bipolarons and annihilation of singlet and triplet excitons.

Boehme and McCamey's Model

Boehme and McCamey [15,34] present "a general model for spin-dependent transitions via exclusive pairs of paramagnetic electron states". In this model excitons are formed from polaron pairs (one positive and one negative charge) in a gradual, multi-step process. Polaron pairs as precursors for exciton formation were first described by Frankevich *et. al.* [35] in 1992.

Initially the charges in the polaron pair move slowly towards each other due to Coulomb attraction. In this well-separated state the spin interaction of the pair is negligible as both the spin-exchange and spin-dipolar coupling energies are significantly smaller than the Coulomb energy. As the charges move closer

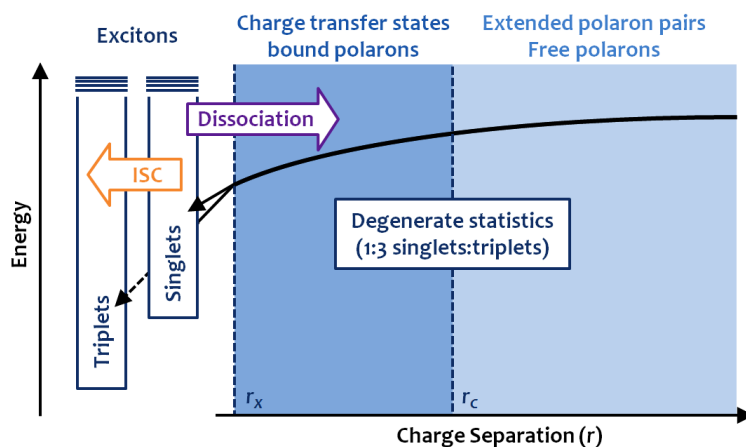


Figure 2.6: Binding energy of electrons and holes as a function of separation distance, showing the characteristic length scales r_c and r_x for which the Coulomb and exchange interactions become significant. Adapted from [15].

together the nature of the pair interaction changes as shown in the binding energy diagram in Figure 2.6. It is only when the pair has a small separation distance that a strongly spin-exchange-coupled exciton state is formed, with a defined singlet or triplet nature.

An important departure from the models for inorganic materials is that in organic materials these two charges are likely to be on different polymer chains. The charges move along the chains by Coulomb attraction to the point of minimal distance between the chains, to form a 'charge transfer' state: exciton formation from this state requires an intermolecular charge transfer. The charge transfer state is strongly Coulomb-coupled but weakly spin-coupled. In contrast the exciton is strongly exchange-coupled, with either singlet or triplet nature depending on the spin dynamics of the charge transfer state.

A schematic of the polaron pair and exciton formation processes is presented in Figure 2.7. Transitions are possible between the polaron pair states, e.g. by intersystem crossing or spin mixing, or by resonant absorption of microwave energy. From these polaron pair states the corresponding singlet and triplet exciton states are populated at rates of k_S and k_T respectively. Dissociation of the polaron pairs to form free charge carriers is a competing process.

Note that the radiative exciton decay to the singlet ground state is rapid, so

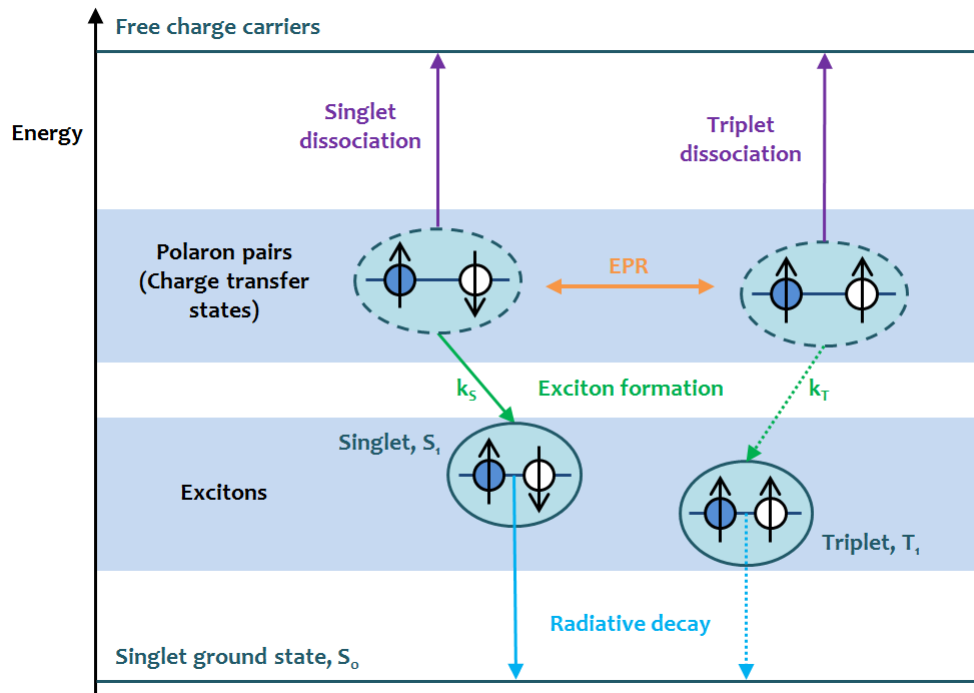


Figure 2.7: Pairs of oppositely charged polarons may bind to form an exciton or may dissociate. EPR affects the spin states of polaron pairs and hence changes the relative rates of singlet and triplet exciton formation. Adapted from [15].

the recombination rate in this model is fully determined by the polaron pair to exciton transition rates. In the case of constant rate coefficients, the light emission will then be governed by the relative polaron pair populations, which may in turn be manipulated by EPR. Similarly the conductivity of a sample is determined by the free charge carrier density, which may in turn be affected by the relative populations of polaron pairs through the dissociation rates.

Boehme and McCamey also include another exclusive-pair formation process in their model, that of spin-dependent bipolaron pair formation (see Sec. 2.1.1). A pair of like charges has a different hopping mobility, so bipolaron formation mainly affects the conductivity and contributes to magnetoresistance effects. Electroluminescence is affected only indirectly, for example if luminescence rates change due to changes in the overall current density.

Shinar's Model

Shinar [17] proposes that non-radiative quenching (destruction) processes of singlet and triplet excitons may in fact be the most significant bimolecular interactions in operational OLEDs. He presents several quenching processes for singlet excitons which result in reduced fluorescence, but as these processes are independent of spin they are of no direct interest here. Ref. [17] may be consulted for further details.

Shinar also proposes a strongly spin-dependent process, specifically the quenching of triplet excitons by polarons:



where TE is a triplet exciton, p is a negative or positive polaron (typically trapped), GS is the ground state of the molecule, and p^* is a high energy polaron (e.g. a transport state). Note that the initial triplet and polaron are in one of six composite spin states: there are four spin sublevels in the $S = (1 + 1/2) = 3/2$ quadruplet manifold and two sublevels in the $S = (1 - 1/2) = 1/2$ doublet manifold. However the final state has total spin of $1/2$ from the polaron, as the ground state is spinless. Hence quenching can only occur from the two doublet sublevels due to spin conservation. Shinar claims that this process is

“the central bimolecular interaction in photoexcited luminescent π -conjugated materials and electrically excited (biased) OLEDs”.

This process is especially important for EDEPR because (under typical operating conditions for fluorescent OLEDs) the relative steady state populations of triplet excitons and polarons are roughly 6×10^5 times the singlet exciton population [17]. With such large triplet and polaron populations a small increase

in the rate of triplet-polaron quenching leads to a large decrease in the polaron population, which may be directly observed as a decrease in conduction.

The effect on light emission depends on whether the OLED is fluorescent or phosphorescent. Quenching of triplet excitons in a phosphorescent OLED directly affects the light emission whereas in fluorescent OLEDs the decreased concentrations of triplet excitons and polarons indirectly affect the singlet exciton population and hence the light emission.

Summary

The operation of an OLED involves charge injection, charge transport, exciton formation and recombination. Several models have been developed for the spin-dependent recombination process in inorganic semiconductors. However, the interpretation of spin-dependent recombination in organic semiconductors is still a topic of debate and few of the models proposed are supported by incontrovertible evidence. Of the two models presented here for organic semiconductors, the former model from Boehme and McCamey is adapted for the discussion in this thesis.

Chapter 3

Background to Electron

Paramagnetic Resonance (EPR)

The previous chapter presented mechanisms by which the absorption of microwaves could change the relative electron-hole recombination and dissociation rates, and hence influence the overall conductivity and/or light emission of an OLED. This chapter outlines how an electron paramagnetic resonance (EPR) experiment can detect these changes, and presents some of the techniques available that make use of the EPR effect. A brief discussion of some of the relevant literature will also be presented, with a focus on EPR studies of operational degradation in OLEDs.

3.1 Conventional EPR

In a conventional continuous-wave electron paramagnetic resonance (EPR) experiment, a sample is placed in a microwave cavity and exposed to continuous, fixed-frequency microwaves. Some microwave power is absorbed by the sam-

ple when resonance occurs; this results in changes in the reflected power which are recorded as the sample is subjected to a slowly sweeping DC magnetic field strength. To allow detection of very small changes in microwave power, the magnetic field is modulated and a Lock-In Amplifier (LIA) is used to detect changes at the modulation frequency. This method produces a first-derivative spectrum as depicted in Figure 3.1.

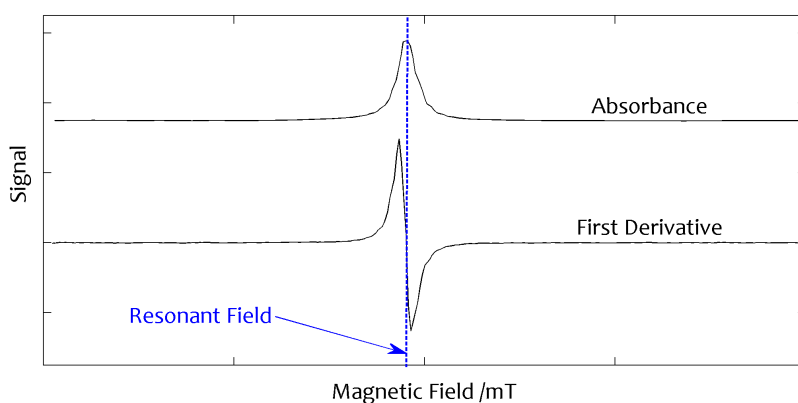


Figure 3.1: Comparison between lineshapes of absorbance and first derivative spectra, for the case of an increase in absorbance (or other relevant parameter, e.g. current or light intensity). The absorbance spectrum is the integrated first derivative spectrum with respect to the magnetic field. Data from room temperature EPR measurement of DPPH with microwave frequency ν of 9.10357 GHz.

From this first derivative spectrum the following information of interest can be extracted:

- The g -value of a resonance may be calculated from the resonant field (shown by the vertical dashed line) and the resonance condition $h\nu = g\beta_e B_r$. For a free electron the g -value is known precisely to be 2.0023 [1]; for typical organic molecules, the g -values are very close to that of the free electron. The g -value provides information about the environment surrounding the resonant electron(s); this environment results in a small anisotropy in the g -value which may be used to infer structural aspects such as molecular geometry.

- Although not visible in this spectrum, for some materials a hyperfine structure may be observed as a splitting of the resonance into two or more lines. Hyperfine structure arises from the interaction of an unpaired electron with nuclear dipole moments; an electron interacting with a proton, for example in the hydrogen atom, gives rise to a pair of lines¹. The hyperfine structure is broadened by spatial averaging in a solid sample and is seldom seen at room temperature in amorphous materials. However in liquid samples electrons in the rapidly tumbling molecules experience an averaged magnetic environment and so the hyperfine structure is more easily resolved.

The power absorbed in a resonance transition scales with $\omega^2 f(\omega) B^2 / T$ where $f(\omega)$ is a 'shape function' and is normalised by $\int_0^\infty f(\omega) d\omega = 1$ [2]. Taking into account the mechanism of detection, this leads to a sensitivity limit of $\sim 10^9 T$ spins at temperature T , or $\sim 10^{11}$ spins at room temperature [2,15]. As mentioned in the Chapter 1, a typical thin film of organic material contains fewer spins than this, so conventional EPR is unsuitable for studying many organic semiconductors in thin film form. However, there are other methods of detection with much greater sensitivity that may be used to study OLEDs, some of which will be discussed in the following section.

3.2 Electrically- and Optically-Detected EPR

For OLEDs, the EPR may be detected with high sensitivity using electrical and/or optical detection methods. For electrically-detected electron paramag-

¹Each of the two electron spin states are split into two states according to the proton spin by the hyperfine interaction. However of the four transitions between these states, two require simultaneous proton spin flips which are much less likely. Hence only the two electronic spin transitions are observed.

netic resonance (EDEPR) measurements on an OLED, the microwave-induced change in the conductivity (σ) of the OLED is measured as the magnetic field strength is swept. This is also known as σ -detected EPR or conductivity-detected magnetic resonance (CDMR) [36]. For optically-detected electron paramagnetic resonance (ODEPR) a photomultiplier is used to detect small changes in the light output or electroluminescence (EL) of the OLED. This is also referred to as EL-detected EPR or electroluminescence-detected magnetic resonance (ELDMR). The experimental arrangement for electrically- and optically-detected EPR, as used here, is illustrated in Figure 3.2.

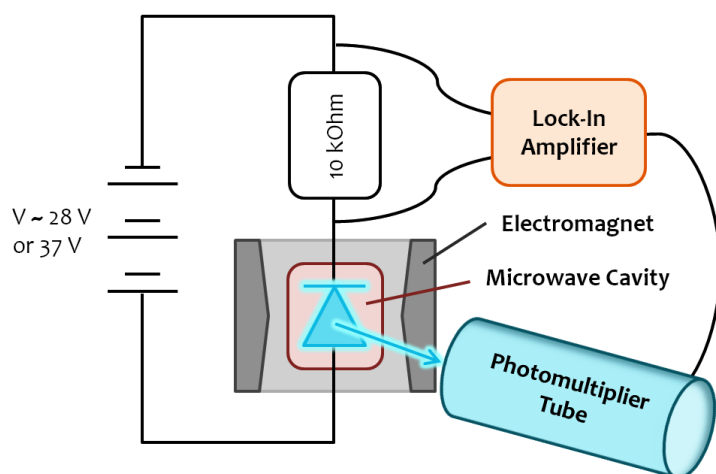


Figure 3.2: Experimental set-up for electrically-detected (ED) and/or optically-detected (OD) EPR. A constant voltage is provided by batteries, and the current through the diode is measured as a voltage across the 10 k Ω resistor. The diode is in a microwave cavity (in red) and in a magnetic field created by an electromagnet (in grey). Light is detected by a photomultiplier tube for ODEPR via a light guide. The magnetic field is modulated by auxiliary coils and the frequency of modulation is used as the reference frequency for the lock-in amplifier.

Some of the advantages of EDEPR and ODEPR over conventional EPR are:

- EDEPR and ODEPR can be observed for small volume samples, for which the sensitivity of EPR is inadequate.
- Only spins that directly impact spin-dependent recombination rates are observed.

- Resonance depends on spin selection rules (not spin polarisation) so resonances may be detected in experimental conditions such as low magnetic fields or high temperatures, where polarisation is low and so conventional EPR is inapplicable.

It should be noted that spin pairs observed optically may not be observed electrically, and vice versa [15], i.e. the effects may be independent of each other.

As for conventional EPR, these methods generally use magnetic field modulation and a lock-in amplifier to increase the signal-to-noise ratio, and therefore produce spectra with first-derivative line-shapes. Alternatively the microwave power may be chopped at a known frequency, e.g. with a PIN diode, but this method was not used here [17].

3.3 Effects at Low Magnetic Fields

There are also some interesting effects that occur at small magnetic fields that are independent of the microwave radiation and thus are not true EPR effects. Two of these effects are magneto-electroluminescence (MEL) and magneto-resistance (MR). MEL and MR may be defined by the following functions of the magnetic field B [37]:

$$\begin{aligned} MEL &= \frac{EL_B - EL_{B=0}}{EL_{B=0}} \\ MR &= \frac{R_B - R_{B=0}}{R_{B=0}} \end{aligned} \tag{3.1}$$

MEL is significant because it means that a small applied magnetic field can significantly affect the electroluminescence. Similarly the resistance and hence the resistive heating of organic devices may be manipulated with the applica-

tion of a small magnetic field. Many papers on MEL and MR effects may be found in the literature (see for example [38–40]). Two key studies are discussed here as a background to low field measurements of the OLEDs in this project.

A particularly insightful study of the MEL was presented by Nguyen and colleagues [37]. Nguyen's group synthesised the polymer poly(dioctyloxy)-phenylenevinylene (DOO-PPV) and a variant where every hydrogen atom attached to a benzene ring or C–C double bond of the polymer backbone was replaced by a deuterium atom. They found a clear overall enhancement of the MEL with increasing magnetic field strength, but with a distinct low-field component of opposite sign. The widths of both components were smaller for the deuterated polymer, a result which led Nguyen *et. al.* to conclude that the MEL effect is mainly due to a hyperfine interaction.

In the second and somewhat controversial study, the MR was measured for a variety of OLED structures by Hu and Wu [41]. Hu and Wu were able to tune the MR from negative (current-enhancing) to positive (current-quenching), for example by increasing the thickness x of a charge-blocking PMMA layer in OLEDs with the structures ITO/PVK(60 nm)/PMMA(x nm)/Al and ITO/PMMA(x nm)/Alq₃(60 nm)/Al. Hu and Wu attributed the negative MR to dissociation dominated by singlet electron-hole pairs and the positive MR to an exciton + charge reaction dominated by triplets. These dissociation and charge reaction processes generate secondary charge carriers that form space charge at the organic-electrode interfaces. This space charge affects the charge injection and thus the resistance. Therefore this scenario gives magnetic-field dependent resistance if the singlet and triplet ratios, and hence the dominant charge reaction and space charge formation process, can be changed by an external magnetic field.

However, Hu and Wu's paper was criticised by Lupton and Boehme (see [42, 43]), and other research by Sheng and Nguyen *et. al.* [44] discounts an excitonic pair mechanism model.

Boehme and McCamey state that of the many current models that predict the MEL and MR effects in organic semiconductors [15], there is general agreement that the effects are related to spin-dependent electronic transitions that change the relative spin populations and hence the overall conductivity and electroluminescence. Their hypothesis regarding the specific process is that the hyperfine interaction influences these spins by changing the spin mixing rate, depending on the ratio of the external magnetic field to the hyperfine field.

3.4 Previous Studies using EPR Techniques

Electron paramagnetic resonance studies have been carried out on a wide variety of OLEDs, with the full range of EPR techniques available. Studies using optical electroluminescence- (EL-), and electrical conductivity- (σ -) detected EPR have revealed both quenching and enhancing resonances, with a myriad of interpretations. An excellent review of such studies was published in 2012 by Joseph Shinar [17]. Some of the key results of these and other studies on polymer OLEDs are discussed in the first part of this section for comparison with the optically- (EL-) and electrically- (σ -) detected study of PFO presented in this thesis².

EL- and σ -detected studies were not found in the literature for the blue-emitting

²Many of the recent studies have focussed on Alq₃-based small-molecule OLEDs. These studies will not be discussed here; for more information the reader is referred to references [45–50].

PFO OLED studied with these techniques in this thesis. Hence the second part of this section presents some studies of these devices with other EPR techniques.

3.4.1 Electrically- and Optically-Detected EPR Studies of Polymer OLEDs

The first EL-detected ODEPR study was reported in 1992, by Swanson and colleagues (including Joseph Shinar) [36]. The study found quenching EL- and σ -detected EPR resonances of PPV-based OLEDs at $g \approx 2.0023$. They concluded that polaron pair to singlet exciton conversion is responsible for the electroluminescence itself, while the EL-quenching resonance was attributed to spin-dependent formation of bipolarons (from two polarons)³. The intensity of these EL- and σ -detected quenching resonances decreased with increasing current, which suggested saturation of specific sites which induce and stabilise bipolaron formation [17].

A subsequent study by Swanson, Shinar and colleagues involved EL- and σ -detected EPR of PPA derivatives [51]. The g -values and lineshapes were similar for the $g \approx 2.0023$ PPV and PPA resonances, and were attributed to an enhancement of singlet exciton generation by polaron-polaron or triplet-triplet fusion. These two studies were both at low temperature ($T \leq 20$ K).

An EDEPR study by Castro and colleagues [52] on MEH-PPV OLEDs in the temperature range 145–300 K found a σ -quenching resonance with $g \approx 2.0022$.

This resonance could be decomposed into two lineshapes: a narrow Lorentzian-

³An alternative mechanism of spin-dependent non-radiative trapping by interface defects would also give the quenching resonances, but would be expected to also give an EPR or light-induced EPR signal, neither of which was observed. However this relies on the sensitivity of EPR to detect these traps.

like component, assigned to the fusion of two positive polarons to a spinless bipolaron, and a broader Gaussian-like component, assigned to the fusion of two negative polarons.

Wang and Yang *et. al.* [53,54] also studied the $g \approx 2$ resonance in MEH-PPV OLEDs. At 10 K and under forward bias, they found EL-enhancing and σ -enhancing in-phase signal components at low microwave modulation frequency, which both reversed to quenching signals at some higher frequency. These resonances were attributed to an increase in current density at resonance caused by enhanced polaron pair effective recombination in the device. Wang and Yang *et. al.* claim that their data are in disagreement with models such as polaron-electroluminescence quenching and triplet-polaron interaction.

Shinar comments in his review that in all of the small molecule and polymer OLEDs that his group has studied, the EL- and σ -detected spin- $1/2$ resonances have been quenching. Although direct evidence is lacking, he claims that the “universally accepted” mechanism is as follows: The magnetic resonance enhances spin-dependent formation of spinless bipolarons, which have a double charge and so are likely to cause strong singlet exciton quenching, which reduces the electroluminescence. Bipolaron formation also reduces the current as two charge carriers are now trapped at some lattice site. Recent pulsed EDEPR results are consistent with this mechanism [55]. Shinar further concludes that the enhancing spin- $1/2$ resonances are due to the triplet-polaron quenching mechanism discussed in Section 2.2.2; EPR increases triplet-polaron quenching, which reduces the polaron and triplet exciton populations, and so reduces quenching of singlet excitons and increases the electroluminescence.

Overall it appears that there is no consensus on the mechanisms by which EDEPR and ODEPR effects occur. Superficially similar results have been at-

tributed to triplet-polaron quenching, polaron-polaron interactions such as bipolaron formation and/or triplet-triplet fusion, and it may be that different mechanisms operate in devices with different materials and structures.

3.4.2 Studies on Blue-Emitting PFO OLEDs

Of particular interest are EPR studies on OLEDs made with the same blue-emitting polymer, PFO, that was studied with EPR techniques in this thesis. More information about this material will be provided in Chapter 5. EPR studies of PFO were found for several techniques not used in this thesis, such as photoinduced absorption detected EPR, light-induced EPR and electron-nuclear double-resonance (ENDOR), but not EDEPR or ODEPR. Key results from two studies are presented here without a discussion of the specifics of these techniques.

Marumoto and colleagues [56] studied the light-induced EPR and electron-nuclear double-resonance (ENDOR) of PFO and a PFO-C₆₀ composite, as powder and spin-cast film samples respectively. They found an EPR signal at $g = 2.003$ below 60 K which, when combined with the transient response and excitation spectrum, indicated that the observed spins were photogenerated polarons on PFO. The spin concentration was evaluated as one spin per 3.5×10^7 PFO-repeat units, and the peak-to-peak linewidth (ΔH_{pp}) was approximately 0.30 mT. The HOMO-LUMO gap was estimated as 3.55-3.68 eV by x-ray photoelectron spectroscopy (XPS) and cyclic voltammetry. They also used light-induced ENDOR to determine that the spatial extent of these polarons is ~ 3 monomer units of PFO. This measurement was made using the PFO-C₆₀ composite as this technique was not sensitive enough to detect a signal from pure PFO due to the low spin concentration.

Photoinduced absorption detected EPR of PFO has been measured by a number of groups. In particular, Wohlgenannt *et. al.* [57] attributed absorption-enhancing (and hence emission-enhancing) resonances to decreases in polaron and triplet exciton populations. They also found that the ratio of formation cross-sections for singlet and triplet excitons in PFO was roughly four. They conclude that the polarons in PFO recombine bimolecularly.

Electrically- and EL-detected EPR on PFO as presented in this thesis thus provides complementary information about these recombination dynamics.

3.5 Degradation in OLEDs

Degradation in OLEDs may occur due to operation or due to exposure to the atmosphere. Kondakov and colleagues [58] define operational degradation as a “monotonic loss of luminance efficiency during operation”, and state that this is one of the most serious problems hindering widespread application of OLED technology commercially. Many mechanisms for OLED degradation have been proposed, for both operational and atmospheric degradation. A general review of OLED degradation by So and Kondakov [59] presents some intrinsic degradation mechanisms in polymer OLEDs, such as trap formation, interface degradation and electrode instability. However the review concludes that the particular degradation mechanisms involved depend on the materials used and the device architecture.

Conventional and electrically-detected EPR techniques have been useful tools for investigating these degradation mechanisms. Two studies of operational degradation that make use of these techniques are discussed here, followed by a few specific comments related to PEDOT:PSS degradation.

Kondakov and colleagues [58] investigated operational degradation in fluorescent and phosphorescent OLEDs based on carbazole derivatives, and found degradation products using analytical techniques, i.e. the chemical composition changed during operation. They used conventional EPR to determine the concentration of radical species in the OLEDs, by comparison with a calibrated standard. The concentration of radicals (relative to the original OLED) grew to over 0.1% in 20 hours of operation. They proposed a free-radical mechanism of operational degradation consisting of excited-state homolytic-bond dissociation followed by radical additions. OLED operation then leads to accumulation of long-lived π -radical species (charged or neutral), which act as non-radiative recombination centres and quench electroluminescence.

Pawlik *et. al.* [60] undertook a quantitative EPR study of internal charging in OLED devices and charge transfer at the cathode for a range of OLED structures, including some devices which they 'deliberately constructed' with a short lifetime. They found that the EPR-detected charge rapidly increases above the turn-on voltage such that it is much greater than expected for space-charge limited conduction regime, and also greater than the expected total accumulated charge in the device due to bipolar conduction. They suggest that trapping of charge due to local disorder might be a cause for the difference, and present results at negative bias showing that trapped charges were released below 100 K, indicating a shallow trap state.

In addition, Pawlik *et. al.* found that annealing increased the formation of radical ion species, and comment that the electron-injection layer of Li as a metal salt (e.g. LiF) is actually a radical-generating reagent. Hence they suggested degradation was due to the migration of Li^+ ions into the organic layer, providing the organic layer is such that Li cations can bind to it (e.g. BPhen).

However, Pawlik *et al.* also comment that there was an order of magnitude difference in the EPR-detected radical concentration between samples evaporated at 5×10^{-6} torr and 2×10^{-7} torr, which suggests possible contamination of the evaporated surfaces with oxygen and/or water may be contributing to the formation of radical ion species.

In their review, So and Kondakov [59] present some specific degradation mechanisms for PEDOT:PSS, which was used in the devices in this thesis as a hole-transporting layer. These degradation mechanisms are (a) water could form H^+ and OH^- ions upon entering through a pinhole in the cathode, and these H^+ ions can chemically reduce the PEDOT:PSS layer, (b) bombardment of PEDOT:PSS with 3 eV electrons releases oxygen and sulphur, which results in changes in conductivity and work function, and (c) these processes and others could form a resistive interfacial layer between the PEDOT:PSS and light-emitting layer. All of these degradation mechanisms in the PEDOT:PSS layer lead to a reduction in hole injection and hence an increase in the operating voltage of the OLED.

In summary, there are a number of degradation mechanisms which have been proposed, of which this discussion presents only a few. One common theme is the generation of radicals and charge trapping, and these effects will form the basis for an interpretation of the results to be presented here. The area of operational degradation in OLEDs is still an active focus of research, with commercial as well as theoretical interest, and the EPR techniques discussed in this chapter provide a useful analytical tool for this research. An investigation of the operational degradation of blue-emitting PFO OLEDs using electrically and optically detected EPR techniques is thus a valuable addition to the literature presented in this chapter.

Chapter 4

Equipment

This chapter describes the instrumentation developed or already available for this project.

4.1 Light-Current-Voltage Tracer

One of the aims of this project was to develop a measurement system to simultaneously measure the voltage, current and light output of the OLEDs. The data from this system would guide the choice of operating parameters and circuit arrangements for the EDEPR and ODEPR experiments. Due to the possible oxygen and water vapour sensitivity of the materials being tested, it was essential that the OLEDs could be characterised *inside a glove box* to maximise the OLED's lifetime, requiring a compact, battery-powered system. The 'LIV Tracer' (Light-Current-Voltage) discussed in this section was designed to meet these criteria.

The physical apparatus consists of a National Instruments data acquisition device (USB-6009) and interface electronics enclosed in a box whose top surface

features two holders for OLEDs, one for those fabricated at VUW and one for red and yellow PPV-based OLEDs provided by researchers at TUV Darmstadt. The finished hardware is shown in Figure 4.1 and designs for the OLED holders and light collection arrangement are provided in Appendix A.

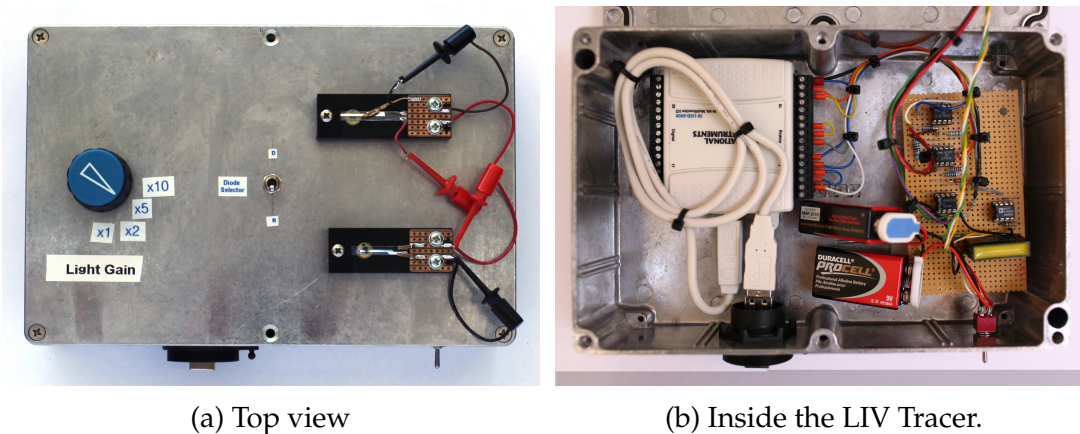


Figure 4.1: The LIV Tracer. (a) Top view showing the adjustable photodiode gain and holders for two types of OLED (Darmstadt upper and VUW lower), each with a silicon photodiode (Hamamatsu S1223) under the light-emitting area of the OLED. The USB connection and ON-OFF switch are on the side. (b) On the left is the National Instruments USB-6009 which is connected to the battery-powered circuit by several analog input and output pins. Connections to the OLEDs and photodiodes pass through the box lid.

A detailed description of the circuit is provided in Section 4.1.1. To control the voltage output and data acquisition, a LabVIEW program was written by the author. This program allows for precise control and automation of the data collection and is presented in overview in Section 4.1.2, and in detail in Appendix A.3.

4.1.1 The Electronic Circuit

The circuit diagram is presented in Figure 4.2, and has three main parts: an I-V circuit, a photodiode circuit, and a power supply, which will be discussed in turn in this section. The circuit was designed by Dr A. Edgar, built by Mr R. Brown and modified by the author.

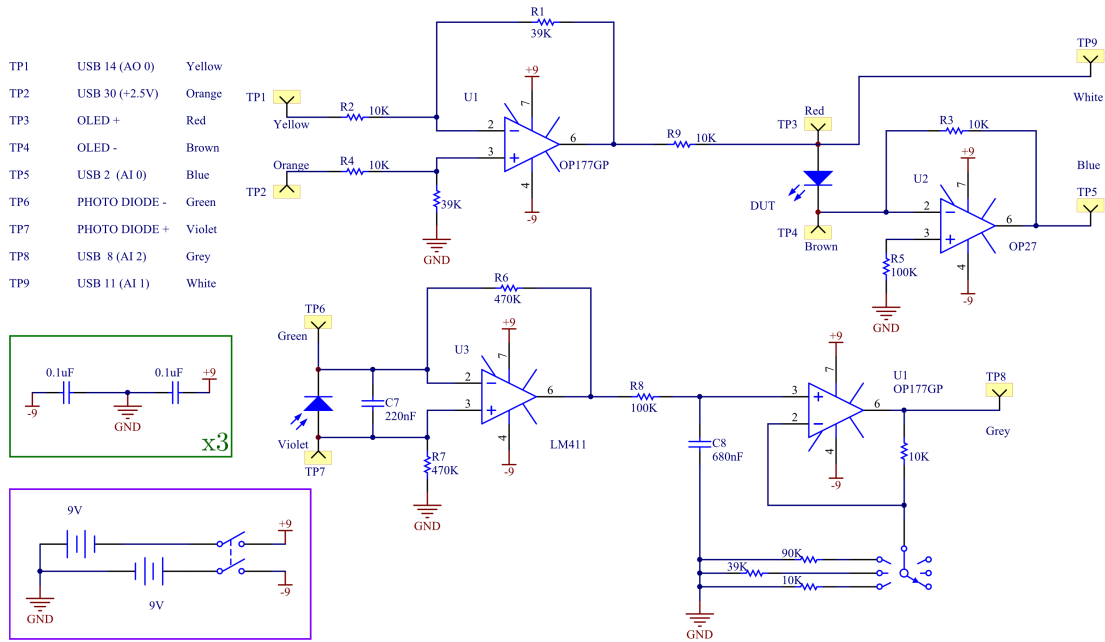


Figure 4.2: The electronic circuit used in the LIV tracer. Connection details for the OLED, photodiode and USB data acquisition device are shown in the table at top left. Top: the diode voltage and current circuit. Bottom: the photodiode circuit. Green frame: capacitors across each of the operational amplifiers. Purple frame: the battery power supply. A block diagram is provided in Appendix A.2.

The diode voltage and current circuit (upper right) measures the voltage across, and the current through, the diode. A small, precise voltage difference in the range -2.5 V to $+2.5\text{ V}$ is generated across TP1 and TP2 by fixing one DAC output of the USB-6009 at 2.5 V and allowing the second output to range between 0 and 5 V . The voltage difference V_{IN} is then amplified by U1 in a difference amplifier circuit configuration, with an output given by $V_{OUT} = -\frac{R1}{R2}V_{IN}$. The voltage across the diode (TP3–TP4) is then sufficiently large and may be measured at TP9 by an analogue input pin of the USB-6009.

The diode current is simultaneously converted to a voltage by using U2 in a current to voltage converter configuration where $V_{OUT} = -R3 I_{IN}$. The diode current is then measured at TP5 by a second analogue input pin of the USB-6009. The values for the resistors chosen for these operational amplifiers were based on typical OLED current densities of $1\text{--}10\text{ mA mm}^{-2}$.

The circuit in the lower right corner of Figure 4.2 measures the OLED light output as detected by a silicon photodiode. Here U3 is used in a current to voltage converter circuit configuration, where $V_{OUT} = -R6 I_{IN}$, so that the photodiode current is measured as a voltage at TP8 by a third analogue input pin of the USB-6009. A selection of resistors and a multipole switch was added by the author as an adjustable gain to give better detection of low light intensities.

As shown in the purple frame, two 9 V batteries were used to power the operational amplifiers in preference to a mains-powered supply unit which would have consequent 50 Hz noise and other interference. Capacitors in the configuration shown in the green frame were included across the supply to each of the operational amplifiers to further minimise electrical noise. The construction inside a die-cast box also helps to minimise noise and interference.

4.1.2 LabVIEW Program

Data acquisition was controlled by LabVIEW software. The LabVIEW program was written by the author and consists of a 'front panel' with which the user interacts to control a measurement, and a 'block diagram' which contains the program in pictorial form.

The program generates a triangle waveform of the desired range and step size, so that the measurement will start and finish at 0 V to avoid leaving a bias voltage across the OLED. A sequence of voltages is then generated by the USB-6009 analogue outputs, and amplified by the circuit so that the desired voltages are applied across the OLED. For each of these applied voltages the USB-6009 records voltages corresponding to the OLED current, OLED voltage, and photodiode current. These are then converted into the true current, voltage and photodiode current values and displayed on real-time graphs.

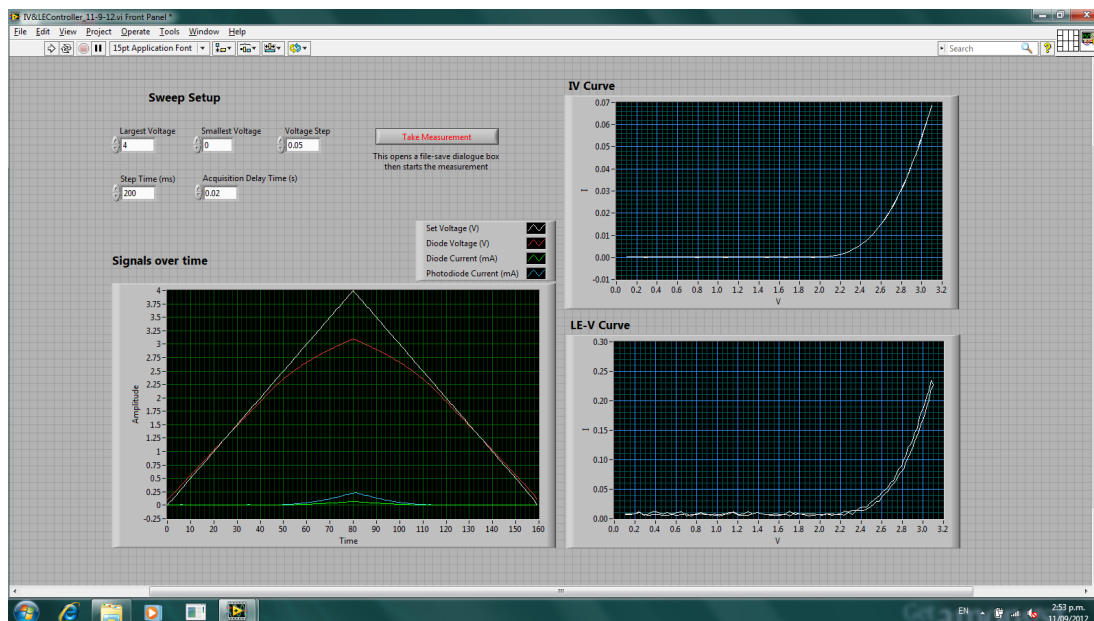


Figure 4.3: A screenshot of the 'interactive' front panel of the LabVIEW program. The set-up boxes show the input parameters of a previous measurement, and the corresponding outputs are visible on the graphs.

The front panel, shown in Figure 4.3 consists of boxes for numeric inputs, control buttons to run the measurement, and graphs displaying the measured signals. As well as the standard plots of current and light emission against voltage, a graph plotting the signals against time was included so that the user can check that the measurement is progressing as expected and diagnose the cause of any problems as they occur.

The block diagram contains the program instructions in pictorial form. The block diagram for the LIV Tracer and a detailed discussion of the LabVIEW program may be found in Appendix A.3.

4.1.3 Capabilities of the LIV Tracer

The LIV tracer was used to successfully measure simultaneous light emission, current and voltage data for super-yellow and red PPV OLEDs from TUV Darmstadt. Samples of data collected from two of these OLEDs are given in

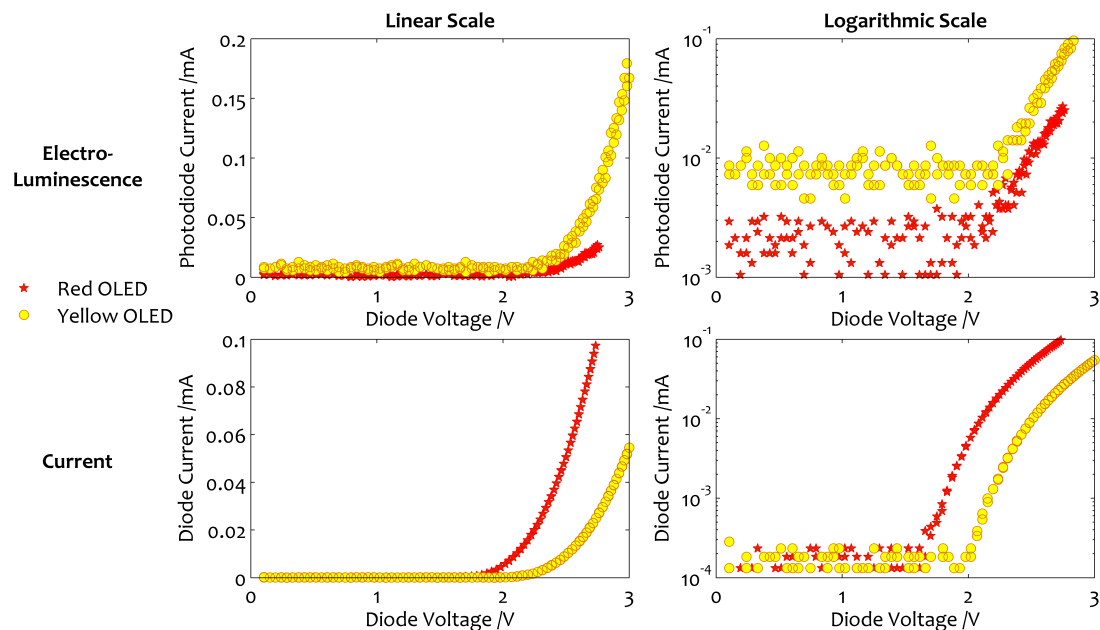


Figure 4.4: Electroluminescence intensity (top) and current (bottom) as a function of applied voltage with linear (left) and logarithmic (right) y-axes, for devices fabricated in Darmstadt with 10×1 mm active areas. Measurements at low applied voltage are limited by the resolution of the USB-6009.

Figure 4.4, with both linear and logarithmic current and light-intensity axes. It is interesting to note the relative turn-on voltages compared to the light intensity. The red OLED has a higher current for the same voltage, but the reverse is true for light intensity. The photodiode was not calibrated for spectral sensitivity, which may account for this result.

The turn-on voltages for the blue-emitting OLEDs fabricated at VUW were significantly higher than anticipated. Hence the maximum output voltage of 9 V, which is ample for the Darmstadt PPV OLEDs, is insufficient to produce a measurable light output from the VUW PFO and PB OLEDs. However, sufficiently large output voltages could be produced with changes to the battery arrangement so that the operational amplifier U_1 runs off +27 V and -9 V. Measuring large OLED voltages would require attenuating resistors to bring the diode voltage into the range of the USB-6009.

The resolution of the LIV tracer is dependent on the measurement range and

USB-6009 DAQ resolution (n bits) according to $\frac{\text{Full Scale}}{2^n - 1}$. For the 12 bit analog output voltages over the range 0–5 V, the resolution is $\frac{5 \text{ V}}{2^{12} - 1} = 1.2 \text{ mV}$. For the analog input measurements, the signal input range may be set separately for each of the three measured parameters and for each measurement (by using a ‘DAQ Assistant’ in the LabVIEW program). For a measurement as shown in Figure 4.4 with 14 bit differential inputs the following input resolutions could be obtained:

- Voltage resolution $\sim \frac{3 \text{ V}}{2^{14} - 1} = 0.18 \text{ mV}$
- Current resolution $\sim \frac{0.1 \text{ mA}}{2^{14} - 1} = 6.1 \text{ nA}$.
- Photodiode current resolution $\sim \frac{0.2 \text{ mA}}{2^{14} - 1} = 12 \text{ nA}$

Hence a higher resolution could be obtained for the smaller voltages and currents by reducing the measurement range, e.g. by measuring up to 1 V only. (The USB-6009 has internal gain selection from 1–20 which means that the 14 bit resolution is retained over a selection of input voltage ranges.)

The step time is dependent on the settling time and hence the time constant $\tau = R8 \times C8 = 0.068 \text{ s}$ of the photodiode circuit (Fig. 4.2), where the noise-reducing capacitor $C8 = 680 \text{ nF}$ and current-limiting resistor $R8 = 100 \text{ k}\Omega$. Allowing five time constants for settling (to within 1% of stable value) limits the step rate to one step every 0.34 s, or roughly three steps per second. A shorter time of 3τ for settling would allow five steps per second with stability to within 5% of the stable value.

4.2 Electroluminescence, Current, and Voltage Measurements

Provision was also made for measurements outside the glove box, for example in combination with EDEPR and ODEPR measurements.

Electroluminescence spectra were measured in air using an Ocean Optics USB-2000+ spectrometer. The spectrometer was calibrated for wavelength by the manufacturer to within 1 nm and for intensity using a standard black-body radiation source (HL-2000-CAL from Ocean Optics).

High-precision current-voltage curves were measured with an Agilent 4156C Precision Semiconductor Parameter Analyser. Advantages over the LIV Tracer include the ability to provide bias voltages of at least 40 V, and to measure currents of order femtoamps. However with this instrument the devices were measured in air, and the electroluminescence intensity could not be measured simultaneously.

Hence simultaneous measurements of the luminous intensity, current density, and voltage were made using a point-by-point method with the set-up as shown in Figure 4.5. In this set-up the device was under a flow of nitrogen in the EPR microwave cavity (to be discussed in Section 4.3). Electroluminescence intensity was measured as a voltage from a photomultiplier tube, with light collected through slits in the microwave cavity. Device current was measured as a voltage across a 10.0 k Ω resistor.

Changes in luminous intensity and current over time were measured with the experimental set-up shown in Figure 4.6; again the device was in a flow of nitrogen during operation. The oscilloscope used as a data logger could record data on up to four channels which could be saved via USB for later analysis.

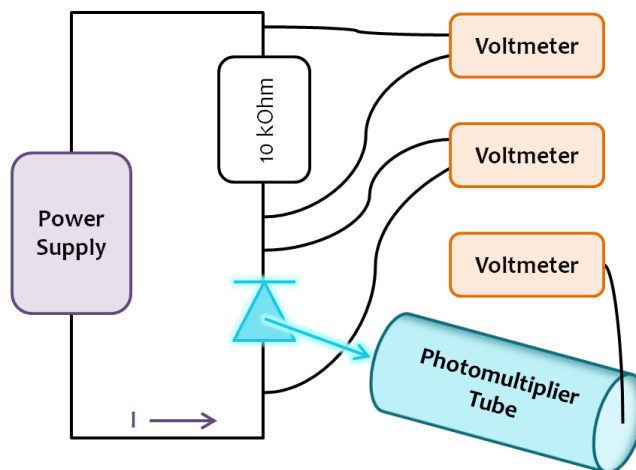


Figure 4.5: Experimental set-up with a high voltage power supply, a photomultiplier tube (900 V operating bias), and three 4^{1/2} digit digital voltmeters.

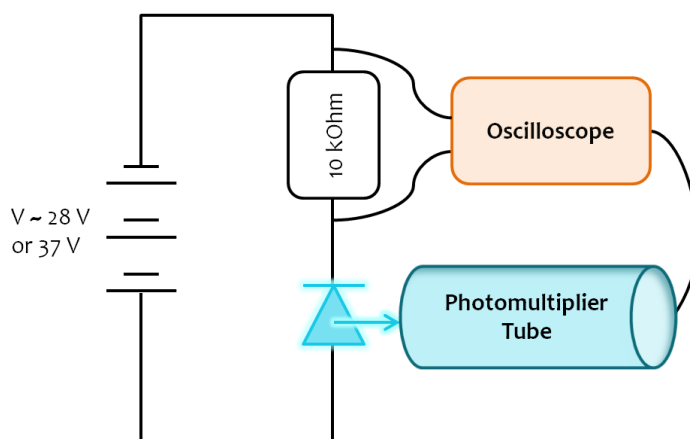


Figure 4.6: Circuit used for time-decay measurements.

4.3 EPR Spectrometer

This section describes the technical details of the custom-built spectrometer used for electron paramagnetic resonance studies. A photograph of the EPR spectrometer is provided in Figure 4.7 and the spectrometer operation is discussed below.

X-band microwaves of approximately 9 GHz¹ are excited in a Varian TE₁₀₂ cavity by a Gunn diode², with maximum attainable power at the cavity of

¹i.e. a wavelength of ~3.3 cm

²A Gunn diode is an N-doped semiconductor diode that has negative differential resistance above some threshold bias voltage. This cancels the positive resistance of a load resonator, creating a circuit with zero differential resistance which produces spontaneous oscillations. The

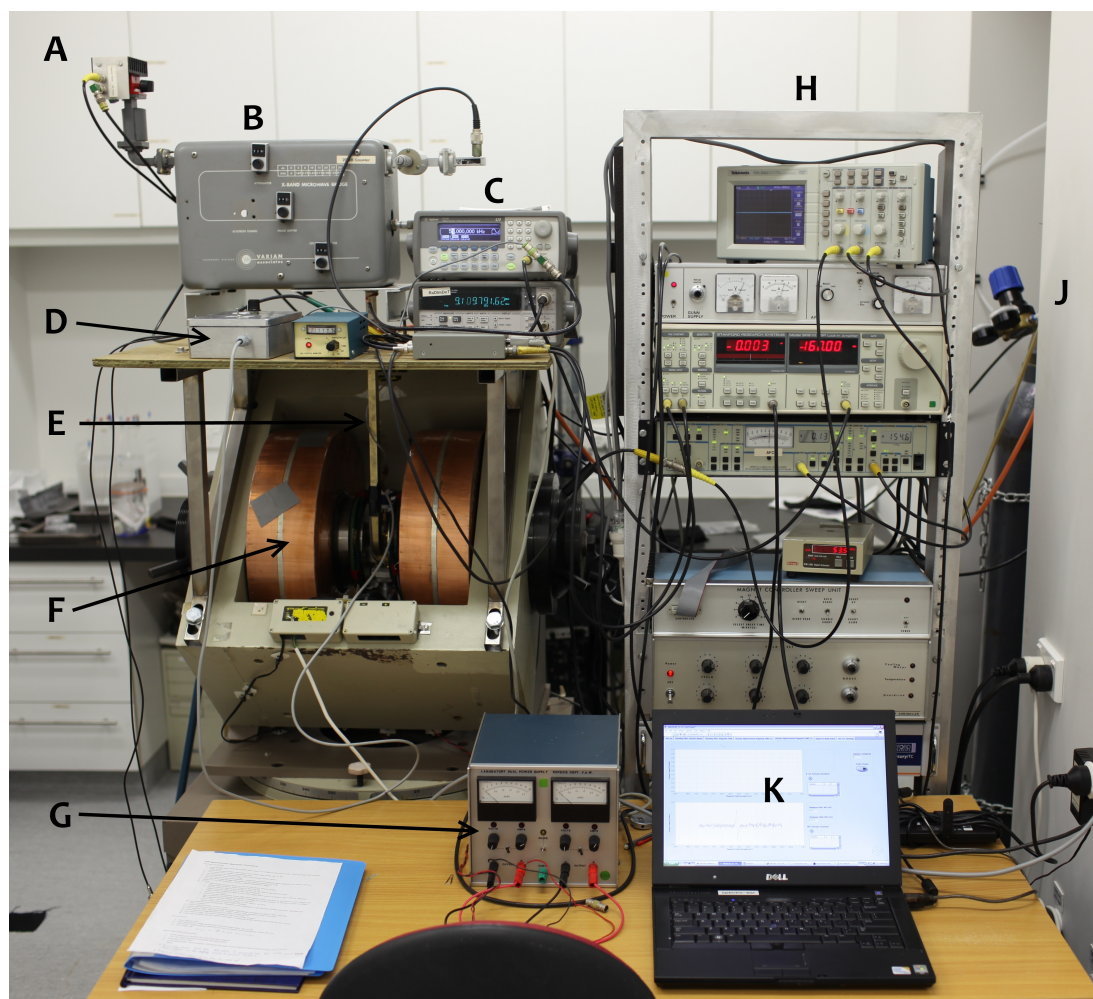


Figure 4.7: Photograph of EPR spectrometer.

- | | |
|--|--|
| <p>A. Gunn diode</p> <p>B. Attenuator and other microwave components</p> <p>C. Stacked electronics (top to bottom):</p> <p style="padding-left: 20px;">Magnetic field modulation controller</p> <p style="padding-left: 20px;">Microwave frequency counter</p> <p>D. (On platform, from left) OLED circuit; Microwave power detector diode; Signal preamplifier</p> <p>E. Microwave waveguide to cavity</p> <p>F. Electromagnet with cavity at centre</p> <p>G. Low-field coil power supply</p> <p>H. Equipment rack containing (top</p> | <p>to bottom):</p> <p>Oscilloscope</p> <p>Gunn diode bias adjustment</p> <p>Signal-detecting lock-in amplifier</p> <p>Lock-in amplifier for microwave automatic frequency control</p> <p>Hall probe magnetometer</p> <p>Magnetic field repeat-sweep controller^a</p> <p>Magnetic field midpoint and range set control.</p> <p>J. Nitrogen supply for flow tube</p> <p>K. Computer with LabVIEW data acquisition program.</p> |
|--|--|

The photomultiplier tube (PMT) is on the bench behind the electromagnet.

^aEither this or the LabVIEW control program may be used to control the magnetic field sweep. This controller is better for rapid repeat scans when all of the data is needed, e.g. during OLED aging. The LabVIEW program is better if an average over several scans is desired.

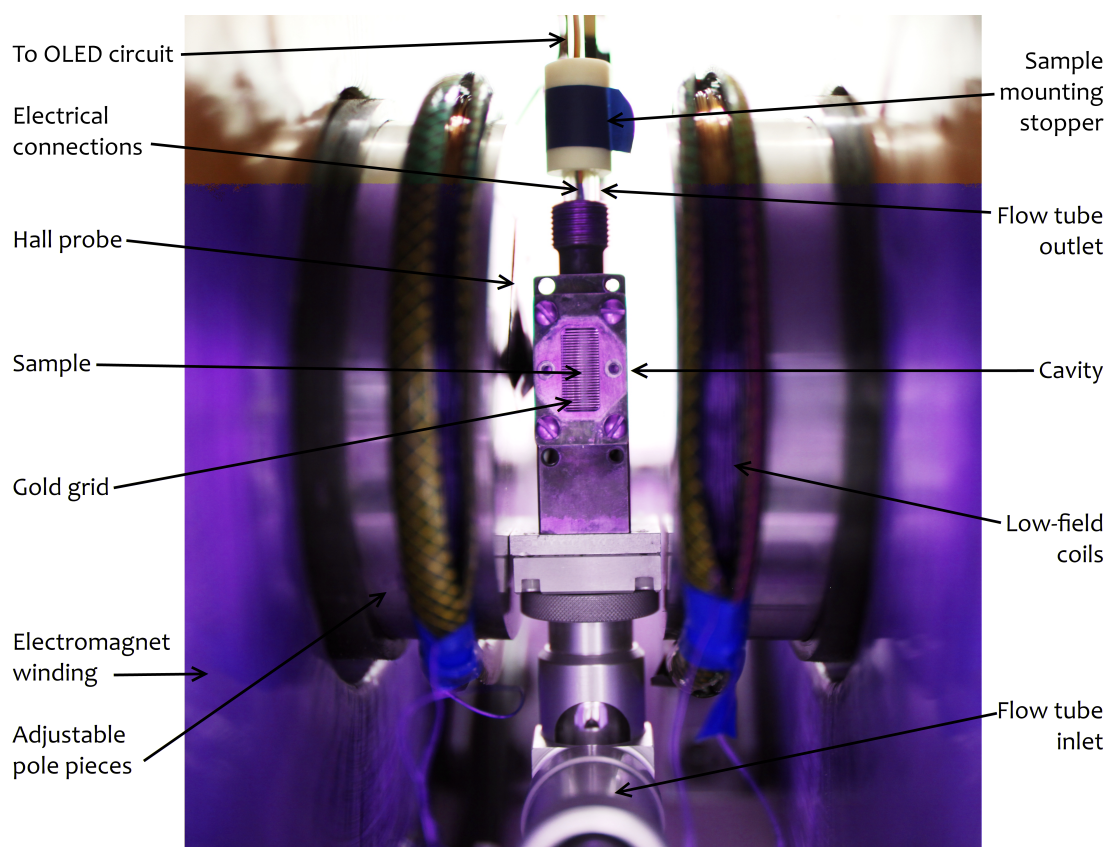


Figure 4.8: Annotated photograph of EPR cavity showing the semi-transparent gold grid and the position of the magnetometer probe.

~ 80 mW. A variable and calibrated attenuator allows the incident microwave power to be reduced by up to 30 dB. The cavity frequency is measured precisely and accurately by an Agilent frequency counter (53181A 12.4 GHz). The cavity has a side wall with a gold grid which gives optical access into the cavity without affecting the cavity resonance. A photograph of the cavity is provided in Figure 4.8.

A double-walled quartz gas flow tube passes through the centre of the cavity, into which the sample is inserted. The gas flow in the tube is a rising stream of oxygen-free nitrogen gas which may be cooled to enable low-temperature measurements. The gas flows around the sample then through a small hole into the room in an open system so small eddies or back-streaming of air may

resonating cavity controls the frequency of the oscillations, and may be tuned mechanically (e.g. by inserting a dielectric rod into the cavity) and/or electronically (e.g. with a varactor) [61].

be present in the top of the flow tube. The position of OLED samples inserted into this flow tube in the cavity is such that the microwave electric field is at a minimum and the microwave magnetic field is at a maximum. This reduces perturbations from the conducting surfaces of the OLED and maximises the magnetic resonance. Also, the tube is unsilvered to avoid interference with the cavity microwave resonance, as well as to aid sample positioning and to allow detection of luminescence from the sample.

Magnetic fields of 5–600 mT are provided with a large water-cooled electromagnet. Two smaller coils are used to extend this field range to -6 mT by powering them from a separate adjustable bipolar power supply. Separate cavity-mounted coils provide field modulation of up to 1 mT over the range 270 Hz to 51 kHz. The magnetic field is measured by a Hall probe magnetometer located outside the cavity. As the probe cannot be placed within the cavity, the true field experienced by the sample is slightly different to the probe field.

The magnetometer is calibrated for the field at the sample in the following way. To determine the true field at the sample location, a sample of 2,2-diphenyl-1-picrylhydrazyl (DPPH) is used as it has a strong paramagnetic resonance (near ~ 320 mT at X-band) with a precisely measured g -value of 2.0036 ± 0.0002 [62]. For zero field, the probe is inserted into a zero Gauss (0 mT) magnetic shield and the magnetometer is 'zeroed' in this condition. A linear interpolation is assumed for the full range of -6 mT to $+0.6$ T. The DPPH resonance is measured as a matter of routine to check the high field calibration, as the sample field depends on the relative positions of the cavity and the pole pieces of the electromagnet, which are moved from time to time to permit extraction and insertion of the cavity.

The OLED is connected in series with a resistor and batteries, as a pseudo-

constant voltage circuit. Batteries are used in this circuit to minimise electrical noise; for the same reason all leads are shielded. For electrically-detected EPR the magnetic field induced modulation of the DC electrical current flowing through the OLED is detected by a lock-in amplifier as modulation in the resistor voltage. A pre-amplifier (Stanford Model SR552) is required for these measurements. A computer with a custom-built LabVIEW program is used to control the acquisition of spectra.

The OLED sample is oriented at right angles to the magnetic field direction so that electroluminescence from the OLEDs is directed through the cavity's semi-transparent grid. This electroluminescence is then guided by a Perspex (PMMA) light-guide to a photomultiplier tube (EMI 9658QB). No optical filtering has been used in this work but could be easily added. Field-induced modulation of the electroluminescence and hence the photomultiplier voltage is detected by the lock-in amplifier. The anode voltage on the photomultiplier tube is 900 V; a grounded lock-in amplifier input is used to reduce noise from the power source of the photomultiplier.

Figure 4.9 shows a block diagram of the spectrometer and how it is adapted for each of the methods of detection. The settings used for each of the detection methods are given in Table 4.1.

Parameter	EPR	EDEPR	ODEPR
Typical microwave attenuation	6 dB	0 dB	0 dB
Magnetic field modulation frequency	51 kHz	51 kHz	270 Hz
Magnetic field modulation amplitude	4 V _{pp}	4 V _{pp}	4 V _{pp}
Lock-in amplifier phase	-160°	60°	-6.1°
Typical lock-in sensitivity	10 mV	1-5 mV	5 μV
Pre-amplifier	Yes	Yes	No

Table 4.1: Experimental settings for EPR, EDEPR and ODEPR.

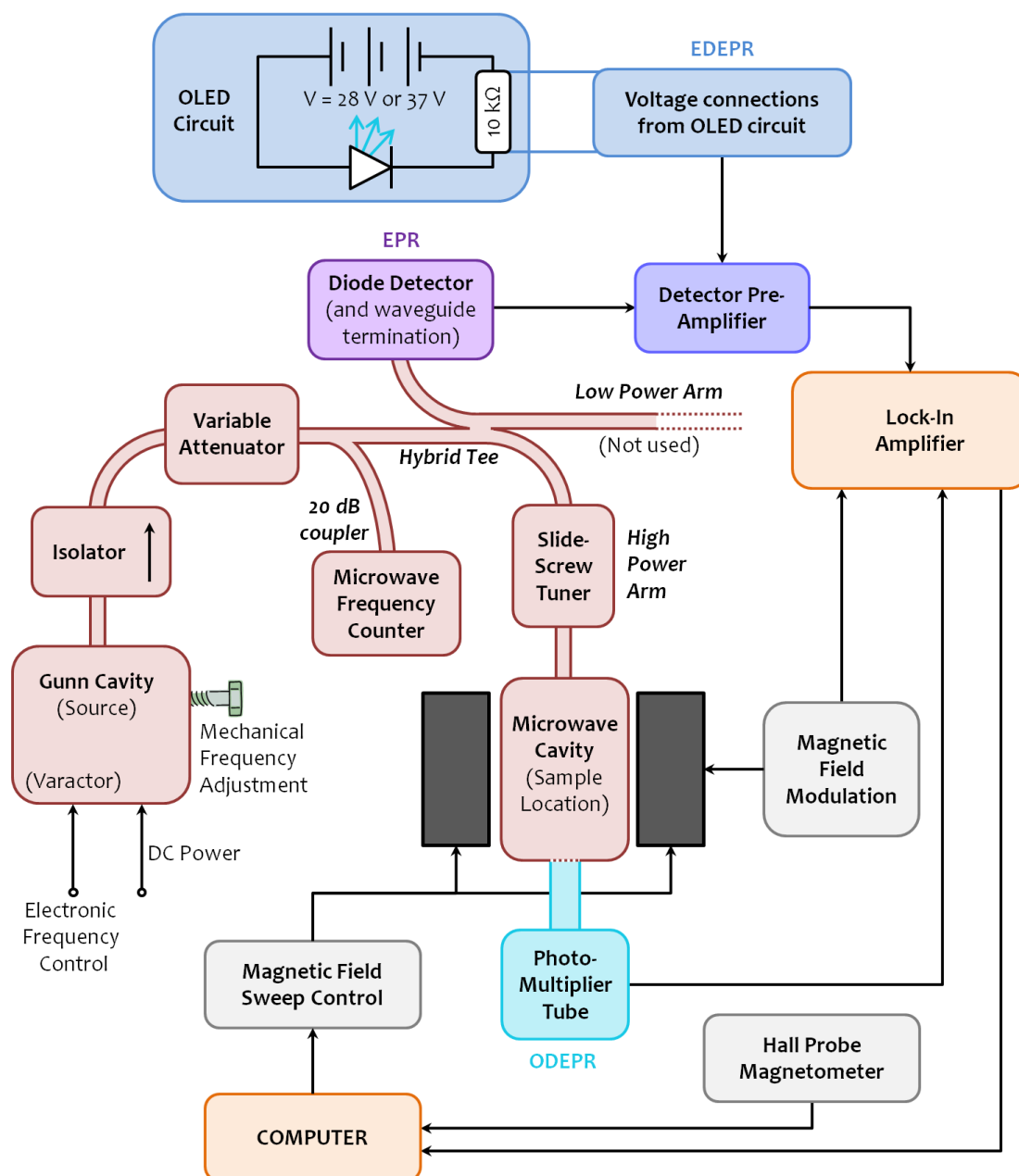


Figure 4.9: A block diagram for the EPR spectrometer. Components of the microwave system are colour coded red, magnetic field components are coloured grey, and other components used for all detection methods are colour coded orange. Components used only for conventional EPR are purple, those for EDEPR are blue, and those for ODEPR are aqua.

Tuning and Phase Dependence

Once the sample is inserted in the centre of the cavity, the Gunn diode mechanical frequency adjustment and bias may be adjusted so that the microwaves are of the precise resonant frequency of the sample-containing cavity. This is as-

sisted by an oscilloscope showing the frequency dependence of the reflected power, where the resonant frequency appears as a 'dip' in the reflected power. An AFC (automatic frequency control) lock-in system then locks onto this resonant frequency as indicated by minimum reflected power.

The amount of reflected power may be controlled with a slide screw tuner, a screw that moves into or out of the microwave waveguide feed to adjust the relative phases of the incident and reflected microwaves. For conventional EPR some microwaves must be reflected, since the detector diode is insensitive at low power, and it is the changes in this reflected power that are measured as the EPR signal. The reflected power may be increased by moving the slide screw tuner either in or out from the position of minimum reflected power. However, the direction of adjustment affects the relative phase of the incident and reflected microwaves, and consequently the phase of the EPR signal, so the EPR signal may be inverted by the direction of detuning.

EDEPR and ODEPR do not require measurement of the reflected microwave power, as they measure changes in sample properties due to the microwave power absorbed by the sample. Hence these spectra are independent of the reflected power, so do not experience the phase dependence described for EPR. However, as EDEPR measures changes in the resistor voltage, the polarity of these connections determine the phase of the measured signal.

To determine whether the current and electroluminescence are increasing ('enhancing') or decreasing ('quenching') at resonance, DC measurements must be made. In practice this is exceedingly difficult as the absolute changes are less than 1%, with noise and drift to further complicate measurement. For this determination an encapsulated red PPV OLED from Darmstadt was used, as the signal-to-noise ratio was excellent and the noise was significantly lower

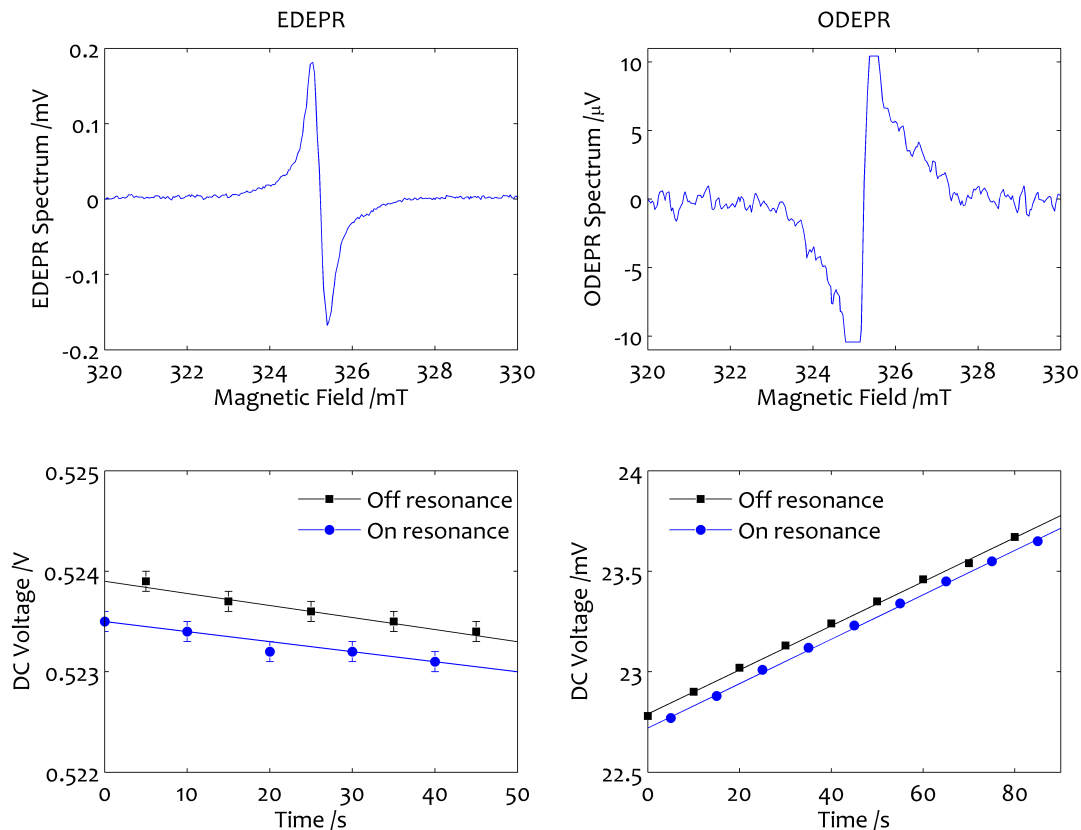


Figure 4.10: Top: Electrically- and optically-detected EPR spectra for a red PPV OLED fabricated in Darmstadt. Bottom: The DC voltages across the current-limiting resistor and photomultiplier resistor on and off resonance (error bars are too small to be visible for optical detection). Hence these spectra correspond to decreases at resonance in the OLED current and electroluminescence respectively, and so are ‘quenching’ resonances.

than the non-encapsulated OLEDs. EDEPR and ODEPR spectra were taken with standard settings (see Table 4.1), and multiple DC readings were taken on and off resonance at regular time intervals to counter drift. The results of these measurements are presented in Figure 4.10 where both spectra are clearly found to correspond to decreases in the DC voltages at the paramagnetic resonance despite a background drift. Hence these are ‘quenching’ resonances. This ‘calibration’ result was then used to determine whether the current and light output increased or decreased at resonance with the VUW-made OLEDs, for which DC measurements were not possible due to the small signal-to-noise ratio.

Chapter 5

OLED Fabrication and Characterisation

This chapter presents a brief overview of some of the material and process considerations before discussing the development of a procedure for fabricating OLEDs at VUW. Key characteristics of the fabricated devices are then presented. Appendix B gives a detailed summary of the specific process which was finally adopted for OLED production.

5.1 A Brief Overview of OLED Fabrication

The first OLEDs were made in the 1960's using anthracene crystals with silver paste contacts [63,64]. In 1987, Tang and van Slyke made OLEDs with thin organic evaporated films [65], a development which was closely followed by spin-coated thin polymer film OLEDs from Burroughes *et. al.* [66]. Since these initial discoveries, many more electroluminescent materials and fabrication techniques have been developed and used to make OLEDs.

It is important to note that the method of fabrication of OLEDs is highly dependent on the choice of organic material(s). For example OLEDs made with small molecules¹ are typically vacuum-deposited, which requires a designated evaporation system. In contrast, some polymers and phosphorescent dopants may be dissolved in volatile organic solvents which may then be spin-coated (see Appendix B.1), blade-coated, or even ink-jet printed, to form a continuous layer or a pixel pattern. These processes occur at room temperature and are easily scaled-up and applied to large areas, and so are of commercial interest. Of these fabrication methods, only the spin-coating method was available at VUW, and the entire fabrication process was open to the air. This required the emissive layers to be made from air-stable and solution-processable materials.

The solution-processable light-emitting materials may be divided into fluorescent and phosphorescent emitters, which may be as light-emitting polymers or dopant molecules (which require additional molecules as hosts). The spin-dependent recombination processes differ between fluorescent and phosphorescent emitters, so OLEDs of each type were fabricated for this research.

Of the fluorescent emitters, fluorescent polymer OLEDs are much simpler to fabricate than OLEDs with fluorescent dopants. There are many fluorescent polymers, with the poly(*p*-phenylene) (PPP), poly(*p*-phenylene vinylene) (PPV), and polyfluorene families as common examples. Of the blue-emitting fluorescent polymers, the polyfluorene PFO (also known as F8) is a solution-processable, commercially available and well-characterised material. There is also considerable interest in PFO as a host material for white OLEDs due to its efficient blue emission and high charge mobility [68]. As PFO was already available from a group within the department this polymer was used to begin the development of the device fabrication process. A yellow-emitting polymer

¹e.g. organometallic chelates, dyes, and conjugated branched molecules (dendrimers) [67].

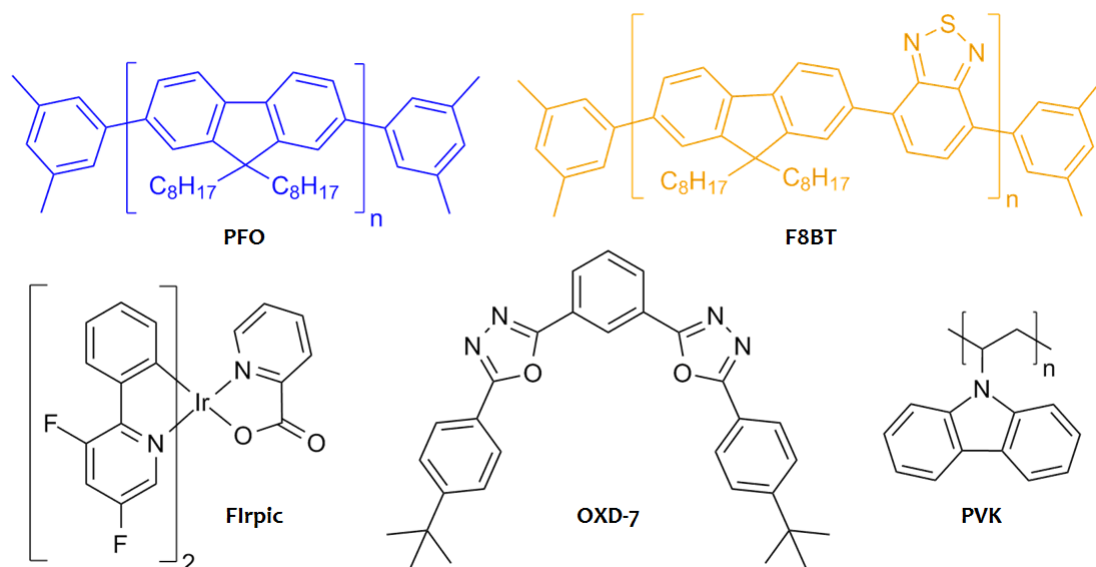


Figure 5.1: Chemical structures for the fluorescent polymers PFO and F8BT, and for FIrpic (phosphorescent dopant), OXD-7 (electron-transporter) and PVK (hole-transporter) [69–71].

derivative of PFO called F8BT was also used to fabricate some devices. The structures of these polymers are shown in Figure 5.1.

The phosphorescent emitters are typically small molecules which are vacuum deposited and/or embedded in a polymer matrix as dopants. An overview of some of the many blue phosphorescent materials for OLEDs is provided by Sasabe and Kido [72]. Many of the common blue-emitting phosphorescent dopants are sky-blue Ir(III) complexes². The first Ir(III) complex was the sky-blue phosphor FIrpic, which was developed in 2001 by Thompson and coworkers [74]. This complex has since been well characterised and incorporated into OLEDs with a variety of host materials, of which many are solution-processable. It is also commercially available, and so was chosen for this project.

The host materials must be able to transport both electrons and holes to the dopant molecules, as well as being chemically compatible with the dopant.

²Most of the ‘blue’ phosphorescent materials in the literature actually fail to meet the criteria for true blue emission [73].

There are many host molecules available, for example from Sigma Aldrich [75], and typically an electron transporting molecule and a hole transporting molecule will be used together as the host. For FIrpic, the hole transporting polymer PVK (which was used in early OLEDs [65]) and an electron transporting molecule OXD-7 were chosen as these materials are solution processable and commercially available, and the combination has been well characterised [69,76,77].

Additional layers that are charge-transporting and/or charge-blocking are often used to improve charge transport and hence device efficiency [76]. However these multi-layer OLEDs often involve vacuum-deposition as spin-coating many layers requires careful consideration of the relative solubilities. Hence the devices in this project have either one or two spin-coated layers.

5.2 Device Fabrication

This section outlines the development of the fabrication processes that were used to make organic light-emitting diodes at VUW. This was a significant challenge since OLEDs had not been fabricated at VUW prior to this project, and especially so since the usual infrastructure of a glove box with integrated spin coater and evaporator was not available. This infrastructure is usually used for OLED fabrication because it allows full device preparation and encapsulation in a clean inert atmosphere, permitting the use of low-work function materials such as calcium for the cathode and significantly increasing the likelihood of successful device fabrication. The infrastructure that was available at VUW was a new clean-room facility, with excellent spin-coaters and thermal evaporator, although all exposed to air. Hence the cathode materials, as well



Figure 5.2: Top view of the device structure. (a) 4 mm \times 25 mm glass substrate with patterned ITO electrode. (b) Spin-coated hole-transporting layer. (c) Spin-coated light-emitting layer. (d) Thermally-evaporated metal cathode. (e) The final structure with the 2 mm \times 1 mm active area highlighted by a red bordered rectangle.



Figure 5.3: A finished OLED with a patterned ITO anode, PEDOT:PSS and PFO layers, and an Al/Ag cathode.

as the emissive materials, were required to be air-stable. Devices made in this facility are likely to contain trapped oxygen and water molecules, accelerating device degradation which could then be studied with EPR in the time frame of this project.

Another significant design consideration was that the device geometry was constrained by the dimensions of the EPR microwave cavity. In order to fit into the 4.2 mm diameter nitrogen flow tube in the EPR cavity, the device must be no wider than 4 mm, allowing for the glass substrate thickness. Also, the active area should be centred in the cavity, and the amount of microwave-absorbing material such as metal and glass should be minimised.

The design that was developed to meet all of the above criteria is shown in Figures 5.2. Figure 5.3 is a photograph of a finished OLED, where faint interference patterns are visible from the transparent polymer layers.

Layers are fabricated onto a long narrow glass substrate in a 'bottom-emitting' structure. The layer structure is shown in Figure 5.4. The first layer is indium tin oxide (ITO), which is transparent and forms the positive anode. In most de-

vices this was covered with a spin-coated hole-transporting layer (PEDOT:PSS). The next, and most important, spin-coated layer was one of three organic light-emitting materials mentioned above: the phosphorescent blue mix of PVK, OXD-7, and FIrpic, the fluorescent blue polymer PFO, or the fluorescent yellow polymer F8BT. An air-stable metal electrode (Al

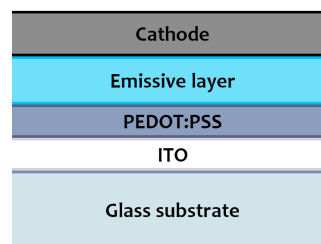


Figure 5.4: Side view cross section showing the OLED layer sequence.

and/or Ag) was then deposited to form the negative cathode; the overlap of this electrode with the ITO electrode defines the active area of the device.

This section will present the fabrication parameters for each of these layers, and discuss some of the considerations made in their development. Once a process was established to fabricate working devices, time constraints limited further process refinements and so the devices were immediately characterised and used for EPR studies.

5.2.1 Substrate and Anode Preparation

ITO coated microscope slides were purchased from Sigma-Aldrich. The slides came as 75 mm × 25 mm × 1 mm sheets with a 15–30 nm ITO layer of resistivity 70–100 Ω per square. To prepare substrates with a width of 3.8–4 mm, the slides were protected with a micron-thick layer of photo-resist then cut to size using a diamond saw. To pattern the ITO electrode, photo-resist was again used, this time with a photolithography and etch technique as it was essential that the ITO pattern was reproducible and well-defined. A printed acetate mask pattern gave excellent edge quality, and the size and shape of the active area could be readily adjusted and reproduced. The excess ITO was etched away with 37% HCl.

The etched substrates were cleaned sequentially in DECON-90 (5% solution in water), water, acetone, and isopropanol, and were dried with a nitrogen spray gun between each of the latter three solutions. Finally the substrates were exposed to an oxygen plasma for 10–20 s to clean and slightly roughen the surface, improving the adhesion of the subsequent spin-coated layer.

5.2.2 Hole-Transporting Layer

A hole-transporting layer was used to improve the charge injection from the ITO layer into the organic layers. Poly(2,3-dihydrothieno-1,4-dioxin)-poly(styrenesulfonate) (PEDOT:PSS) was chosen for this layer as it is commonly used and

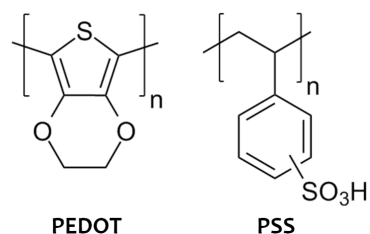


Figure 5.5: Chemical structure for PEDOT:PSS.

readily available. However, this material comes as various mixes of two conducting polymers (chemical structures shown in Figure 5.5) and without a standard ratio, so is highly batch-dependent. Three mixes were tested: high- and low-conductivity grades from Sigma-Aldrich, and 'BaytronP' as given to us by researchers from the Technical University of Darmstadt. Only BaytronP produced working devices.

Two grades of PEDOT:PSS from Sigma-Aldrich were tested and found to form unsatisfactory films. The high conductivity grade (Aldrich 483095) was very viscous and produced 90–100 nm thick films even on the highest spin speed. Conversely, the low conductivity grade material (Aldrich 560596) had a low viscosity and formed very thin films (20–30 nm) even when spun at a slow speed of 2000 rpm with a small acceleration.

Also, an asymmetric ridge of about 800 nm thick formed as depicted in Figure 5.6. The pattern of this ridge was dependent on the spin direction so could be manipulated to avoid the active area of the device. However no devices worked when made with either of these grades of PEDOT:PSS.



Figure 5.6: Asymmetric ridge formed when spinning PEDOT:PSS.

All of the working devices were made with BaytronP, which formed smooth films of 40–50 nm. This solution was filtered with a 0.45 μm PVDF syringe filter before spin-coating at 3000 rpm for 1 minute. The film was heated for 30 minutes at 120 °C and/or kept under house vacuum for at least 2 hours to remove excess water. The excess PEDOT:PSS layer (in the regions away from the active area) was then removed with isopropanol to reduce the risk of direct contact between the PEDOT:PSS layer and the deposited metal electrode.

5.2.3 Emissive Layers

As described in Section 5.1, two blue-emitting materials were used as emissive layers: a phosphorescent mix of three chemicals known as Flrpic, OXD-7 and PVK, and a fluorescent polymer, PFO (F8). For convenience the phosphorescent blue emitting material is here labelled 'PB' for phosphorescent blue. The fabrication parameters are presented after some remarks about the problems that needed to be overcome in developing a successful fabrication process.

Initially, most of the devices fabricated were nearly-perfect Ohmic resistors, or became resistors at voltages below 5 V, and not diodes. The main cause of this failure-at-birth was thought to be short circuits through the emissive layer, either from pinholes in the layer or PEDOT:PSS spikes that pierce through the layer. Hence the quality of this layer was deemed paramount in the fabrication of a successful device.

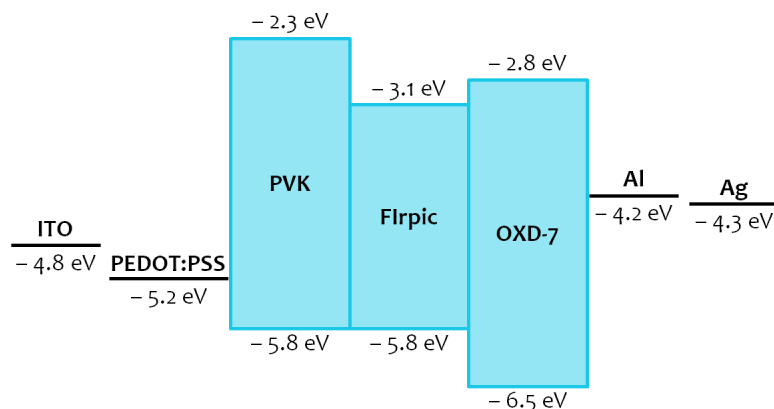
The steps taken to improve the emissive layer and other aspects of the device fabrication process are summarised in Appendix B.2 (Table B.1). A key step was reducing the active area from $\sim 8 \text{ mm}^2$ to $1\text{--}2 \text{ mm}^2$ with photolithography of the ITO electrode. This step together with the removal of the excess PEDOT:PSS regions decreased the likelihood of pinhole contacts between the metal and ITO electrodes, and led to devices with 'non-Ohmic behaviour' in the voltage range -2 to $+5 \text{ V}$. A few of these improved devices showed diode-like behaviour over this voltage range, and two of these devices emitted short-lived flashes of blue light with applied voltages of $\sim 9 \text{ V}$.

After making over 100 devices with only these two short flashes of light, test devices were made with the yellow-emitting fluorescent polymer, F8BT, to see if the devices were failing due to poor device fabrication or due to the inherent instability of the blue-emitting materials. These F8BT devices had clear diode-like current-voltage characteristics and emitted yellow light below 9 V as expected. The PB and PFO devices, which were 'non-Ohmic' below $\sim 5 \text{ V}$, showed no light emission with applied voltages of $\sim 9 \text{ V}$, but also did not break at this voltage like the early devices had done. Crucially, when tested with a high-voltage power supply these devices emitted blue light from about 12 V for the PB devices and from about 35 V for the PFO devices.

Phosphorescent Blue

The phosphorescent devices were made using a polymer mix of PVK (poly(9-vinylcarbazole), Aldrich 182605), OXD-7 (1,3-bis((4-tert-butyl-phenyl)-1,3,4-oxadiazolyl)phenylene, LT-N855 from LumTec, Taiwan), and FIrpic (bis-(3,5-difluoro-2-(2-pyridyl)phenyl-(2-carboxypyridyl)-iridium(III), from LumTec, LT-E607). PVK forms a hole transporting polymer matrix, OXD-7 is an electron

Figure 5.7: The HOMO and LUMO energy band diagram for the phosphorescent emitting OLED [69].



transporter and Flrpic is a blue phosphorescent dopant. The relative HOMO and LUMO levels of these materials are depicted in a schematic electronic energy profile in Figure 5.7. The chemical structures of these materials was shown earlier in Figure 5.1.

These materials were dissolved in anhydrous chlorobenzene using a magnetic stirrer bar at a total concentration of 25 mg/mL and in a 10:4:1 ratio by weight of PVK:OXD-7:Flrpic, following Chen *et. al.* [69], and Li *et. al.* [76]. Once dissolved, the solution was filtered with a 0.45 μm PVDF syringe filter and spin-coated at 2000 rpm for 30 s to give 140 ± 10 nm films which were dried under house vacuum. In the literature this layer is annealed at 80 °C for 30 minutes in an inert atmosphere [69,76]. Some short-lived light-emitting devices were fabricated with annealing under a flow of high-purity nitrogen, but devices with longer lifetimes were fabricated when the annealing step was omitted.

The concentration and spin parameters were established from the tests of film thickness shown in Fig. 5.8, where the thickness was measured with a Dektak profilometer. Solutions with different concentrations of PB were spin-coated onto circular substrates to gain an understanding of the dependence on spin speed of the thickness for the different solution concentrations. On rectangular substrates of the actual OLED dimensions, the layers were slightly thicker and less uniform than on the circular substrates. For a layer thickness of around

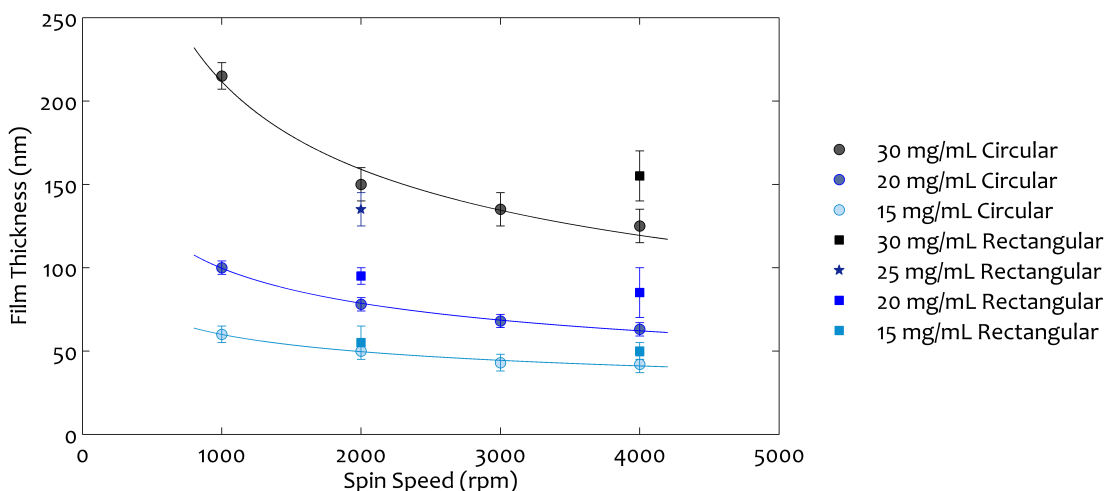


Figure 5.8: Thicknesses of films for different concentrations of organic solid dissolved in chlorobenzene as a function of spin speed, on circular substrates and with some tests on rectangular substrates.

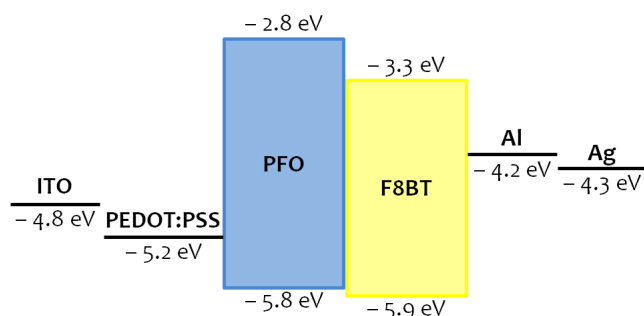
150 nm with a moderate spin speed of 2000 rpm the required concentration was estimated to be about 25 mg/mL.

Fluorescent Blue and Yellow

The fluorescent materials PFO and F8BT are closely-related polymers (see Fig. 5.1 for the chemical structures), and so devices with these materials were fabricated with the same parameters. The blue-emitting fluorescent polymer PFO (or F8) has the chemical name poly(9,9-di-n-octylfluorenyl-2,7-diyl), and was purchased from American Dye Source, Inc. (ADS129BE and Sigma Aldrich Aldrich 571652). The yellow-emitting fluorescent polymer F8BT has the chemical name poly[(9,9-dioctylfluorenyl-2,7-diyl)-co-(1,4-benzo-(2,1,3)-thiadiazole)], and was also purchased from American Dye Source, Inc (ADS133YE). PFO and F8BT have average molecular weights of 58,200–73,000 and 10,000–30,000 respectively, and relative HOMO and LUMO levels as shown in Figure 5.9.

PFO (or F8BT) was dissolved in anhydrous chloroform at a concentration of 15 mg/mL. The vial of solution was continually rotated on a bed of rollers

Figure 5.9: The HOMO and LUMO energy band diagram for the fluorescent emitting OLEDs with either PFO or F8BT emitting layers [70,71].



to aid the dissolving process. Once dissolved, the solution was filtered with a $0.45 \mu\text{m}$ PVDF syringe filter and spin-coated at 2000 rpm for 30 s to give 190 ± 10 nm films. The concentration and spin-coating parameters were determined with the aid of Figure 5.10, such that the PFO (or F8BT) film would be comparable to the PB film in thickness. The effect of the solvent is evident here, as chloroform evaporates faster than chlorobenzene which leaves a thicker PFO (or F8BT) film than for the equivalent PB concentration. The high volatility of chloroform also led to rapid, uneven drying of the film due to the rectangular shape of the substrates (see Fig. 5.6). This was overcome by attaching the substrate to a larger piece of glass for the spin-coating step.

Thin films of PFO and F8BT crystallise at $\sim 90^\circ\text{C}$ and $\sim 115^\circ\text{C}$ respectively, with an intermediate glass transition temperature $\sim 50^\circ\text{C}$ [78]. To avoid these transitions and to minimise exposure to oxygen and water molecules, these films were dried under house vacuum without annealing.

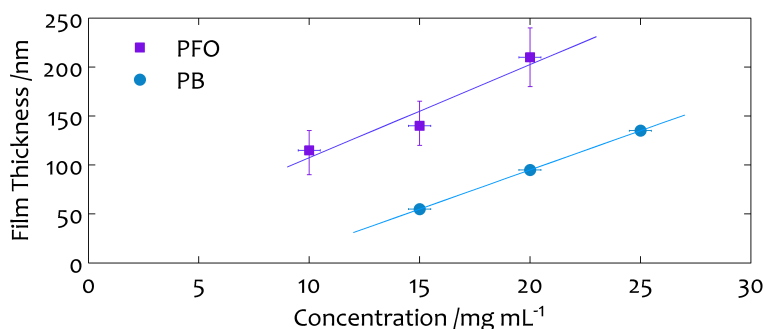


Figure 5.10: Spin-coated thicknesses with different concentrations of PB and PFO, spun at 2000 rpm for 30 s on clean rectangular substrates.

5.2.4 Cathode

The cathode was deposited through a shadow mask in an Angstrom Engineering Nexdep thermal evaporator. The shadow mask was designed by the author to accommodate up to ten devices in each of the two electrode patterns shown in 5.11. Kapton tape and ITO anode patterning were used to create a small active area while developing the fabrication procedure; this could be increased up to 10 mm in length with the appropriate ITO pattern. Wires were attached to the electrodes either with silver conductive paint or with pressed indium contacts.



Figure 5.11: Top view schematic following Figure 5.2, showing the two different cathode patterns. The ITO anode pattern underneath is for an active area of 2 mm length. Active areas (bordered in red) are of (a) 1 mm width (b) 2 mm width.

Silver and aluminium were tested for electrode materials, as either 100 nm Ag or 50 nm Al with a 50 nm capping layer of Ag. Although aluminium can damage the PFO film [79], both the melting temperature and work function of aluminium are lower than those of silver, and it is considerably cheaper. As both options gave working devices it was concluded that Al (50 nm)/Ag (50 nm) was the preferred option.

Usually an encapsulating layer would be applied over the entire device, for protection against water and oxygen. As our OLEDs were fabricated in air, oxygen and water molecules were already trapped in the organic layers so the encapsulation step was omitted. Instead the completed OLEDs were stored in a nitrogen glove box with an atmosphere of <0.1 ppm O_2 and <0.1 ppm H_2O .

5.2.5 Comments on OLED Fabrication

A summary of the successful fabrication process is provided in Appendix B. Once the fabrication of working devices was established a batch of 18 devices (RS160–RS177) was fabricated, of which 16 were light-emitting. These and some of the existing light-emitting devices (from batches RS137–RS147 and RS148–RS159) were used for the following characterisation studies.

5.3 OLED Characterisation

This section presents some of the properties of the OLEDs fabricated at VUW, including the electroluminescence and current-voltage characteristics.

5.3.1 Electroluminescence

Electroluminescence (EL) was observed for devices made with each of the three emissive materials. Figure 5.12 shows the spectral emission of these OLEDs, as evidence of successful OLED fabrication and for comparison with the literature. Peaks in these spectra occur at 500 ± 1 nm for the green-blue phosphorescent PB OLED, at 440 ± 1 nm and 520 ± 1 nm for the fluorescent purple-blue PFO OLED, and at 540 ± 1 nm for the greenish-yellow fluorescent F8BT OLED.

Nakamura *et. al.* [80] measured the EL spectrum of a device with the structure ITO/PEDOT:PSS/PVK:OXD-7:Flrpic/Cs/Al. The PB spectrum in Figure 5.12 has the same overall shape as the spectrum observed by Nakamura *et. al.*. The 500 nm peak observed here is close to the 497 nm peak observed in the literature which was attributed to Flrpic emission.

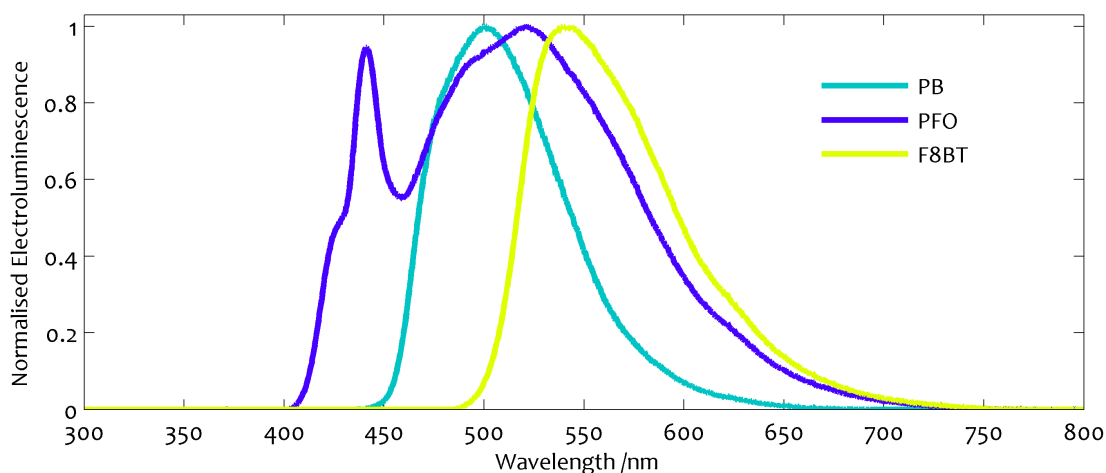
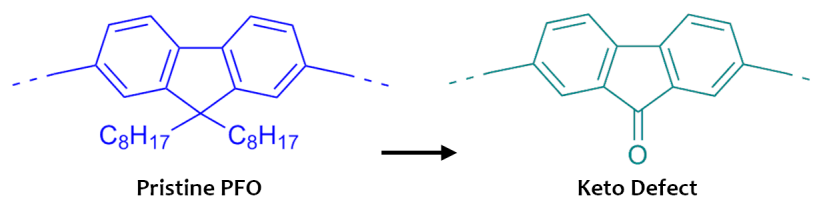


Figure 5.12: Electroluminescence spectra, normalised by the maximum intensity, for three OLEDs fabricated at VUW. These OLEDs were RS148 (PB with PEDOT:PSS), RS152 (PFO with PEDOT:PSS) and RS159 (F8BT only), and were from the same fabrication batch.

The EL spectrum was measured for an ITO/PEDOT:PSS/PFO/LiF/Al device by Oner *et. al.* [81]. A broad structure with peaks at 437, 463, 500, and 530 nm was observed, resembling the PFO spectrum in Figure 5.12. The relative intensities of these peaks changed with bias voltage when tested over the range 6–12 V: for 6 V the high-energy peaks are more intense, whereas the 500–530 nm peaks begin to dominate from 10 V. The PFO spectrum in Figure 5.12 was measured at a bias voltage of ~ 35 V, so it is possible that the broad peak at 520 nm is some combination of the 500 and 530 nm peaks, while the 437 nm peak is observed at 440 nm. Other measurements of the EL spectrum of pristine PFO show a strong peak around 440 nm, with lower intensity peaks at longer wavelengths [82].

Keto defects are known to form in polyfluorenes [83], and these defects have an unstructured blue-green emission around 500–520 nm [81]. Hence the observed broad emission around 520 nm in Figure 5.12 indicates that there may be some keto defects present in the PFO OLED. The keto defects could easily be formed as shown in Figure 5.13 given operation in air and the high applied bias voltage.

Figure 5.13:
Possible keto
defect formation.



Morgado *et. al.* [82] measured the F8BT EL spectrum with a device structure ITO/PEDOT:PSS/F8BT/Ca/Al; the spectrum is qualitatively similar to the F8BT spectrum in Figure 5.12.

Photographs showing these emissions are presented in Figures 5.14 and 5.15. Two brightnesses were photographed for the blue OLEDs to show the colour and apparent brightness for a given applied voltage. Also, spatial variation was seen as bright edges in 5.14a and speckling in 5.14c.

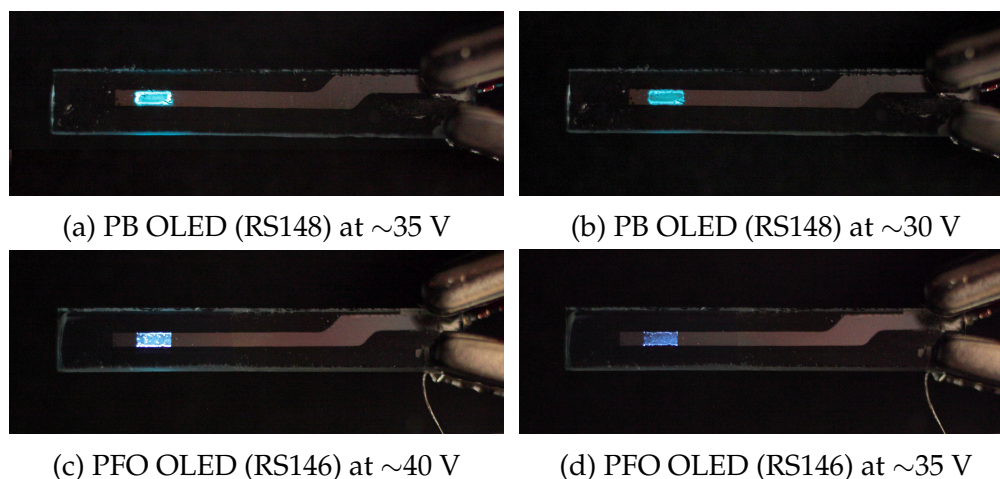
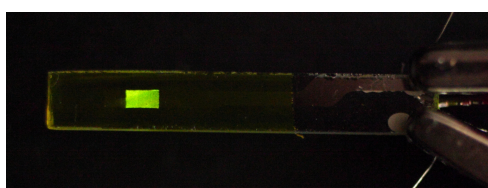


Figure 5.14: Photographs of phosphorescent (top) and fluorescent (bottom) blue-emitting OLEDs at two different voltages showing the relative brightness and colours.

Figure 5.15: A greenish-yellow F8BT OLED (RS159) with strong electroluminescence at 26 V.



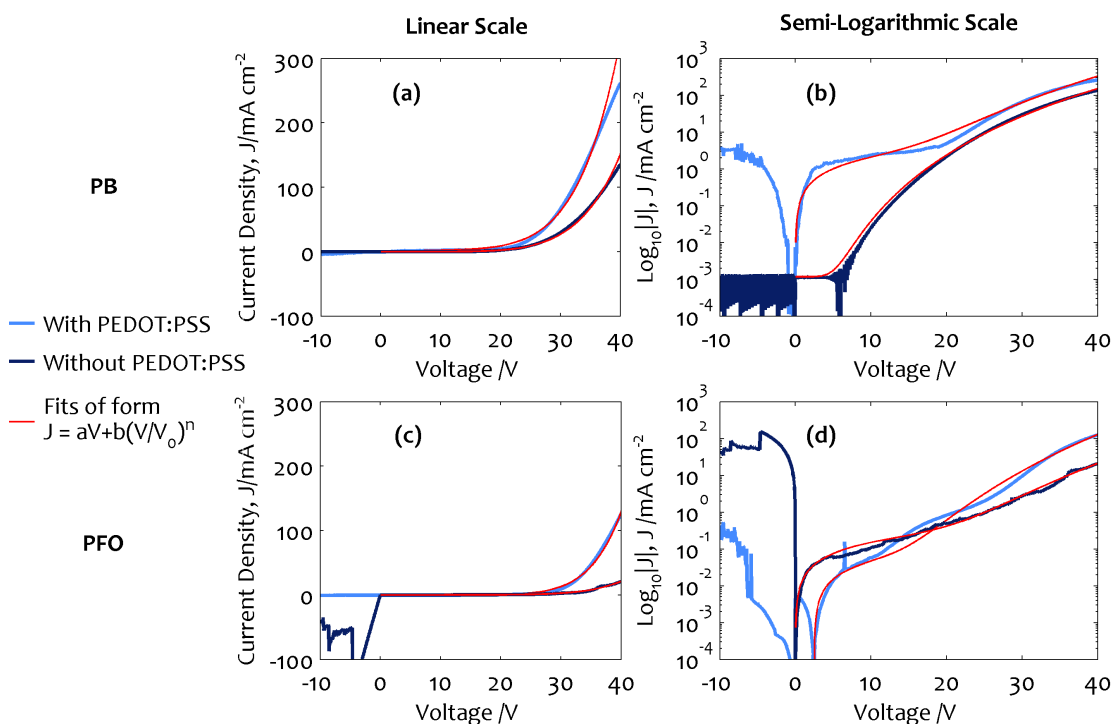


Figure 5.16: Current density as a function of applied voltage for (a) PB devices RS167 and RS175, with and without PEDOT:PSS respectively, with a linear current density axis, (b) As for (a) but with a logarithmic current density axis, (c) PFO devices RS164 and RS170, with and without PEDOT:PSS respectively, with a linear current density axis, (d) As for (c) but with a logarithmic current density axis. These four OLEDs were from the final fabrication batch (RS160–RS177). Fits to the data, in red, are discussed in the text. Note that the measured current density in (a) is lower than that predicted by the fit for voltages above 35 V.

5.3.2 Current-Voltage Characteristics

A standard characteristic of device performance is the current-voltage relationship. Figure 5.16 shows current-voltage data for phosphorescent PB devices with and without PEDOT:PSS, and for fluorescent PFO devices with or without PEDOT:PSS, taken from the best-performing device for each type of OLED.

Several regimes are observed in Figure 5.16. For small forward biases the conduction is Ohmic, which appears on the semi-log plots (b) and (d) as a $\ln V$ section, before the current rises as a high power of the applied voltage. The latter effect can be interpreted as the conduction becoming ‘trap-controlled space-charge-limited’ which may be modelled by a power law term [84]. The expo-

ment of this power term must be greater than two³ and depends on the density and energy distribution of the trapping states, which could be for example an exponential distribution. Typically the exponent increases with increasing temperature.

When the voltage is sufficiently large, the traps empty and conduction becomes effectively ‘trap-free space-charge-limited’ and so follows Child’s law with an exponent of two. However this regime is not always realised, as the current may saturate or the device may suffer dielectric breakdown before this transition voltage is reached. Here Figure 5.16(a) shows a slight tail-off for the phosphorescent devices above ~ 35 V which may be the beginning of a transition to the trap-free space-charge-limited conduction regime.

Therefore fits to the data in 5.16 are of the form

$$J = aV + b(V/V_0)^n \quad (5.1)$$

where aV is an Ohmic leakage current as in Figure 5.16. The fitting parameters for the power law terms are given in Table 5.1. The PB device without PEDOT:PSS shows no Ohmic leakage, but rather a fixed current for small voltages. This is significantly different from the other devices and it is not known why this occurred; both devices showed similar light emission (see Figure 5.12). Here the fit was adjusted empirically by replacing the Ohmic term with a constant. The data for the PFO device with PEDOT:PSS shows an onset of the linear regime at 2.5 V, which may be due to a residual bias from the previous measurement at negative applied voltages. The fit takes this onset into account empirically by replacing the aV term by $a(V - 2.5)$.

³A power term with an exponent of two is known as Child’s law and corresponds to trap-free conduction. For more information, see [7].

OLED Type	PB		PFO	
	V_0 (V)	n	V_0 (V)	n
With PEDOT:PSS	20	6	25	8
Without PEDOT:PSS	25	6	22.5	7.5

Table 5.1: Fitting parameters for Equation (5.3.3) which model the trap-limited conduction regime in Figure 5.17. The V_0 and n parameters have uncertainties of ± 0.5 V and ± 0.2 respectively.

Figure 5.16 shows that the phosphorescent PB devices have a higher current density when compared with the fluorescent PFO devices for the same applied voltage. Many factors may give rise to this higher current density, including that of triplet versus singlet recombination. The fact that the PB emissive layer contains both high mobility electron and hole charge carriers compared to pure PFO which only has high mobility for one charge carrier may also play a role.

The current densities are also much higher for devices with a base layer of hole-transporting PEDOT:PSS, for both phosphorescent and fluorescent devices. This base layer was included for this very reason, as PEDOT:PSS is known to improve charge injection from ITO into the organic layers.

In the literature, Li *et. al.* [76] made a phosphorescent OLED with the structure ITO/PEDOT:PSS/PVK:OXD-7:FIrpic(10:4:1)/CsF/Al where a current density of 20 mA cm^{-2} was achieved with a bias voltage of 12.4 V. A similar device with a structure of ITO/PEDOT:PSS/PVK:OXD-7:FIrpic(7:3:1)/CsF/Al, Mathai *et. al.* [77] found the same current density at 8.6 V. Both of these devices had emissive layer thicknesses of 75 nm. Here current densities of 20 mA cm^{-2} were reached at 25 V and 28.6 V for devices with 140 nm thick PB layers, with and without PEDOT:PSS respectively.

For the PFO devices, Ma *et. al.* [85] studied OLEDs with the structure ITO/PEDOT:PSS/PFO(70 nm)/Al. A current density of 20 mA cm^{-2} was reached with

a voltage of 7 V for these devices. Bradley *et. al.* [86] found the same current density at approximately 14 V for another device structure, ITO/BFA/PFO/Ca where BFA is a hole-transporter and the PFO layer was 200 nm thick. Here current densities of 20 mA cm^{-2} were reached at voltages of 32 V and 40 V for devices with 190 nm thick PFO layers, with and without PEDOT:PSS respectively.

The significantly higher bias voltages required for the VUW devices are most likely due to the open-air fabrication environment. Other factors include the cathode material and the emissive layer thickness.

5.3.3 Electroluminescence-Voltage Characteristics

Figure 5.14 clearly shows that the intensity of electroluminescence (EL) increases with increasing applied voltage, as expected. Here simultaneous current, voltage and EL intensity point-by-point measurements were made on OLEDs of each type to characterise this relationship. Plots of the voltage dependence of the EL intensity are shown in Figure 5.17 with both linear and logarithmic axes. The point-by-point current density measurements are shown for comparison with the EL measurements and with Figure 5.16.

Fits to the data are of the forms:

$$\begin{aligned} EL &= I_{dark} + b_L(V/V_L)^{n_L} \\ J &= aV + b_J(V/V_J)^{n_J} \end{aligned} \quad (5.2)$$

where I_{dark} is the dark current in the photomultiplier, and aV is an Ohmic leakage current as in Figure 5.16. a , b_L and b_J are constants of proportionality.

It is clear from the EL data in Figure 5.17 that the phosphorescent devices are

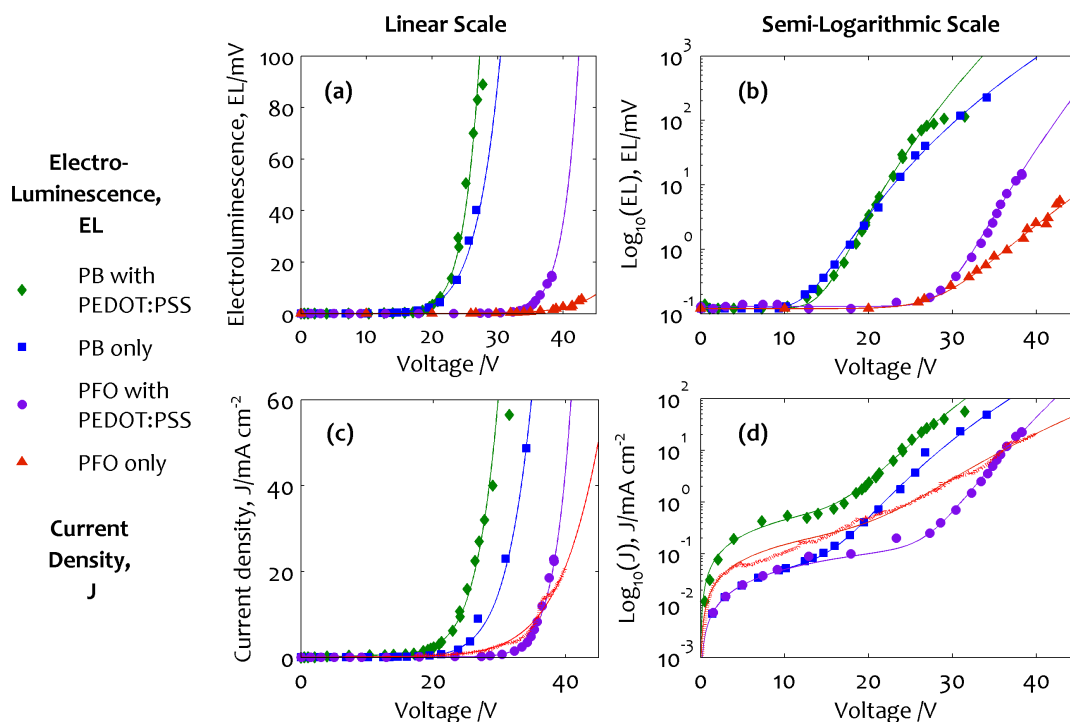


Figure 5.17: Electroluminescence intensity (top) and current density (bottom) as a function of applied voltage with linear (left) and logarithmic (right) current density axes, for each of the four OLED structures: PB with PEDOT:PSS (RS166), PB only (RS175), PFO with PEDOT:PSS (RS165), and PFO only (RS170), all from the final fabrication batch. Fits to the data points are shown as smooth lines; equations and key parameters are given in the text and in Table 5.2. Current density data for the PFO-only device is from Fig. 5.16 as simultaneous EL and J measurements were not possible due to the high resistance of the device. ‘Electroluminescence’ measurements at low applied voltages are non-zero due to the dark current in the photomultiplier tube.

much brighter than the fluorescent devices for the same applied voltage. This is expected based on the data for current density, in both Figures 5.16 and

OLED Type	Electroluminescence		Current Density	
	V_L (V)	n_L	V_J (V)	n_J
PB with PEDOT:PSS	27	11	25	9
PB only	25	8.2	25	9
PFO with PEDOT:PSS	30	18	30	15.5
PFO only	20	10	(22.5)	(7.5)

Table 5.2: Fitting parameters for Equation (5.3.3) which model the trap-limited conduction regime in Figure 5.17. Parameters in parentheses correspond to data taken under different experimental conditions. The V_0 and n parameters have uncertainties of ± 1 V and ± 2 respectively.

5.17. The absolute value of the EL intensity could not be determined with the available equipment, so a comparison with the literature for device efficiency is not possible.

Figure 5.17(b) shows that there is very little difference in EL intensity between PB devices with and without PEDOT:PSS, despite the consistently lower current density in the PB-only device. As discussed for the J–V data, this may be due to the presence of both hole- and electron-transporting species and therefore more balanced charge transport in these devices. In contrast the PFO devices show a marked increase in EL intensity with a PEDOT:PSS layer.

Also of interest are deviations from the $(V/V_L)^{n_L}$ fit at high voltages, which are most apparent in (b) and (d) of Figure 5.17 for the PEDOT:PSS/PB device. This may be the beginning of trap-free space-charge limited conduction, as suggested for Figure 5.16(a). However it is more likely due to measurement error caused by instability in the devices, especially at the higher voltages where drift was significant during the time taken to record the three measurements. Hence an automated measurement system would be of great advantage in this situation. It was noticed that this drift at high voltages had a trend: the current and EL intensity would rapidly increase and then slowly decrease over time. This trend was further investigated and the results are presented in the next section.

5.3.4 Time-dependent Decay

It was found that both the current density and the electroluminescence (EL) intensity are unstable at high voltages, and decay over time. These decays were measured for several ON-OFF cycles of a phosphorescent OLED (RS138) with a PEDOT:PSS layer and an active area of $1 \text{ mm} \times 1 \text{ mm}$. The OLED was

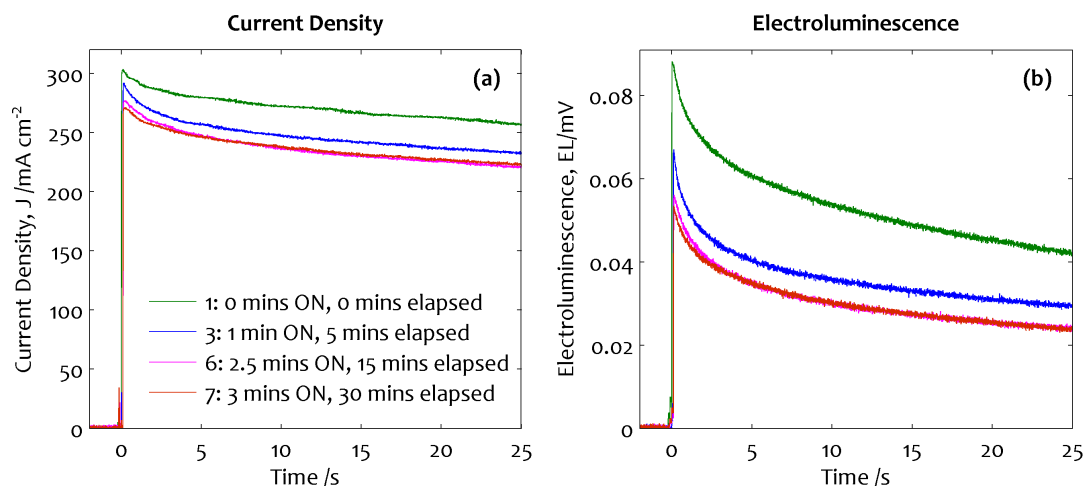


Figure 5.18: Decays of the current density (left) and electroluminescence (right) over time, with constant driving voltage, for a PB OLED (RS138). Measurements 1, 3, 6, and 7 are shown; very little change occurs between the final two measurements so these data appear superimposed. Time points are 'Total time ON, elapsed time' at the start of each measurement.

turned ON for each measurement of 25 s duration and otherwise was OFF. A constant forward bias voltage of 28.55 ± 0.01 V was applied when the OLED was ON.

Measurements 1, 3, 6, and 7 are shown in Figure 5.18. The current density and EL intensity decays are of different scales. In the first 25 s measurement the current density drops by only 15% whereas the EL intensity drops by over half its initial value (53%). In the seventh measurement the current density and EL intensity drop by 18% and 55% respectively over the 25 s measurement.

Also of note is the recovery between measurements. For example the OLED was OFF for nearly 15 minutes between the sixth and seventh measurements, which show current densities and EL intensities that differ by at most 2%.

OLEDs with a PFO emissive layer showed similar decays of the current and luminescence but these decays were not measured quantitatively due to time and sample constraints.

The significant decay in the EL intensity and smaller decay in the current in-

icates that some sort of ageing is occurring during device operation which is leading to non-radiative recombination. The recovery after an OFF period suggests that charges are being progressively trapped. This supports the model of trapped space-charge limited current flow that was discussed in Section 5.3.2.

5.4 Chapter Summary

OLEDs were successfully fabricated in air, with a geometry optimised for EPR experiments. Device structures were as follows, with the PEDOT:PSS layer omitted in some devices:

1. ITO/PEDOT:PSS/PVK:OXD-7:FIrpic/Al/Ag
2. ITO/PEDOT:PSS/PFO/Al/Ag
3. ITO/PEDOT:PSS/F8BT/Al/Ag

These OLEDs produced electroluminescence with spectra in agreement with literature results. The spectrum from a PFO OLED showed signs of partial degradation consistent with the formation of keto defects.

Both the PB and PFO OLEDs showed space-charge-limited conduction with significant trapping. Emission was visible above ~ 12 V and ~ 25 V for the best PB and PFO blue-emitting OLEDs respectively.

The current density and EL intensity were found to decrease during OLED operation, with partial recovery following a period of rest. This behaviour was recorded for the phosphorescent devices but was observed to be of a similar nature for the PFO devices. Hence for EPR studies where ageing was not desired, the OLEDs were turned OFF when not being measured.

Chapter 6

Electrically and Optically Detected Electron Paramagnetic Resonance in PFO OLEDs

Electron paramagnetic resonance techniques were used to study two new PFO OLEDs with the structure ITO/PEDOT/PFO/Al/Ag (RS160 and RS164, from the same fabrication batch). The first part of this chapter outlines the key results, in three sections. The first section presents the characterisation of a new OLED (RS160) with three of the techniques described in Chapter 3: conventional, electrically-detected (ED), and optically-detected (OD) electron paramagnetic resonance (EPR). The second section covers the microwave power dependence of the two signals found in the first section (again with RS160). The third section describes an ageing study on the high-field signal using the second new OLED (RS164). In the second part of this chapter, these results are discussed in terms of the spin-dependent recombination mechanisms of Chapters 2 and 3.

6.1 Results

6.1.1 Comparison of EPR Techniques

Electron paramagnetic resonance spectra using three methods of detection are presented in Figure 6.1. EPR spectra of the quartz nitrogen flow tube, the clean glass substrate, and the OLED (RS160, both ON and OFF) are shown in spectra (a) to (d).

Spectra (a) and (b) were taken to check for any EPR-active species in the flow tube and in the clean glass substrate. These spectra show similar structure between 200 and 300 mT; the broad resonance near 300 mT may be from traces of Cu^{2+} in the cavity or flow tube, since this is the magnetic field region where the $g \approx 2.2$ resonances characteristic of Cu^{2+} may be expected [2]. In spectrum (b) resonances just above 150 mT correspond to a g -value of ~ 4 , which may be attributed to Fe^{3+} impurities in the glass substrate [87].

Spectra (c) and (d) were taken to compare with (b) to see if the polymer film of the OLED gives a visible EPR signal. In spectrum (b) of the clean glass substrate, there is a small signal at 325 mT which corresponds to a g -value of 2.0070 ± 0.0004 . This signal is not seen in spectra (c) and (d) where instead there are small signals near 324 mT with g -values of 2.003 ± 0.001 . These signals are close to the free electron g -value and may arise from free radicals in the OLED film. The comparison of spectra (c) and (d), shown in spectrum (e), shows that there is very little difference between the EPR spectra with the OLED ON and OFF. Hence the presence of the charge carriers necessary for light emission does not result in any new EPR signal.

However for EDEPR and ODEPR, two strong first-derivative resonance signals are seen in spectra (f) and (g), one near zero field and one just above 300 mT in

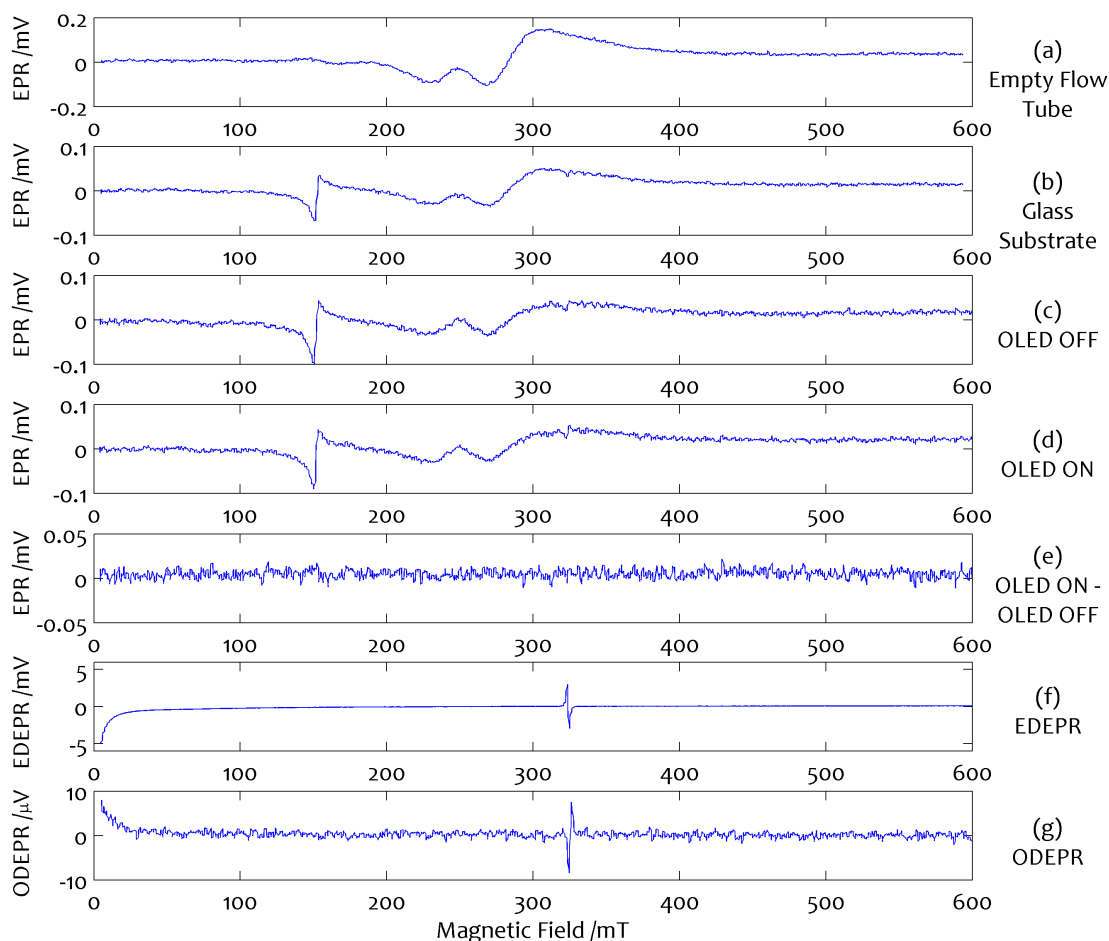


Figure 6.1: Room temperature electron paramagnetic resonance spectra with each of the three techniques. Conventional EPR spectra of (a) the empty quartz flow tube with nitrogen flow (b) a clean ITO-coated glass substrate (c) the OLED (RS160) turned OFF (d) the OLED turned ON (e) the difference between (c) and (d), showing that there is no detectable EPR signal corresponding to the OLED emitting light (f) EDEPR spectrum (g) ODEPR spectrum.

each spectrum. Comparison of the phase of the lineshapes in (f) and (g) with Figure 4.10 shows that both the low and high field signals decrease the OLED current and electroluminescence. Both the EDEPR and ODEPR high field resonances have a g -value of 2.003 ± 0.001 , which is consistent with EDEPR and ODEPR measurements of other polymers (see Sec. 3.4.1, and [17,36,52,53]), and with measurements on PFO using other EPR techniques (see Sec. 3.4.2, and [56,57]).

The signal-to-noise ratio of the EDEPR spectrum is extremely high, illustrating the very high sensitivity that may be achieved with this technique. For ODEPR

the signal-to-noise ratio is good but is currently limited by the low efficiency light collection geometry due to the location of the acceptance face of the light guide outside the cavity. Nevertheless, the spectra in Figure 6.1 show that EDEPR and ODEPR are both viable methods for studying OLEDs.

6.1.2 Effect of Microwave Power

The strong EDEPR and ODEPR signals were further investigated to see if they were both due to electron paramagnetic resonance absorption. As discussed in Chapter 3, the magnitude of a true electron paramagnetic resonance signal is directly proportional to the microwave power incident on the cavity, at least until saturation occurs [2].

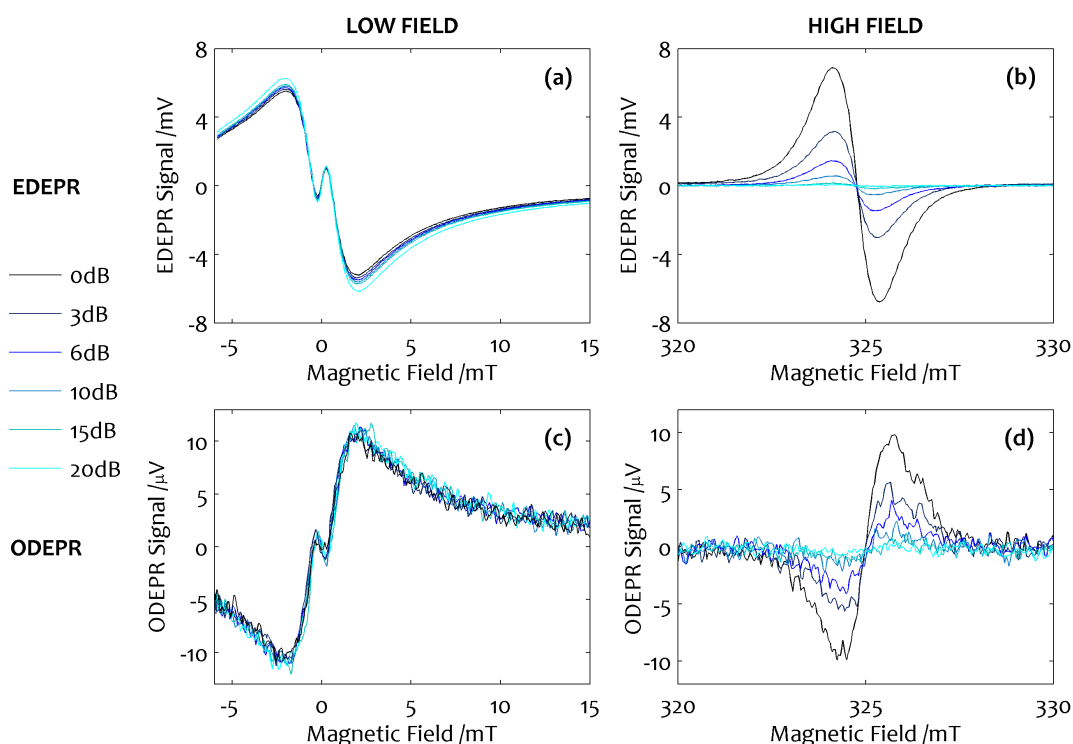


Figure 6.2: Microwave power dependence of low field (left) and high field (right) signals with electrical (top) and optical (bottom) detection. An attenuation of 0 dB corresponds to the maximum microwave power of 80 mW; 20 dB corresponds to 0.8 mW. Spectra were taken at room temperature using the PFO OLED RS160 with a microwave frequency of 9.106 ± 0.001 GHz.

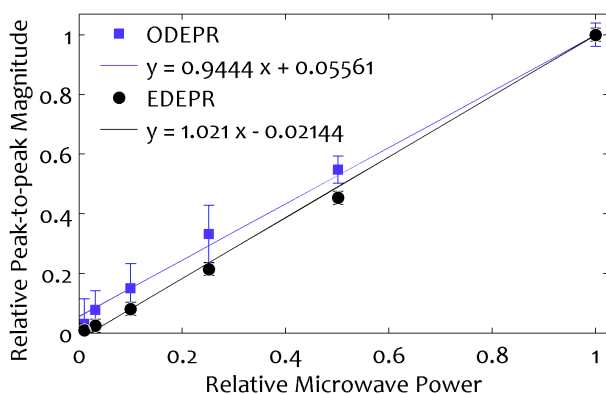


Figure 6.3: Microwave power dependence of the peak-to-peak magnitudes from the high field EDEPR and ODEPR spectra in Figure 6.2. The maximum microwave power was 80 mW.

Figure 6.2 shows the effect of changing the incident microwave power on the EDEPR and ODEPR signals seen in Figure 6.1. The microwave power dependence was measured for the magnetic field ranges of -6 to 15 mT (low field) and 320 – 330 mT (high field). For the low field measurements, auxiliary coils were used to sweep from negative to positive fields. These coils were not used for Figure 6.1, which shows only fields greater than $+5$ mT.

The microwave power has essentially no effect on the low field signals in spectra (a) and (c) of Figure 6.2. Note that for both EDEPR and ODEPR the low field signal comprises a broad quenching signal and a narrow enhancing signal. The lack of dependence of the low field signal on the microwave power indicates that this is not an electron paramagnetic resonance. Instead these signals may be attributed to magneto-resistance and magneto-electroluminescence (see Section 3.3, and [37,41,42]) and arise simply because the light emission and conductivity are particularly field-dependent near $B = 0$ and this is being detected via the effects of field-modulation and lock-in detection.

For the high field spectra (b) and (d), both EDEPR and ODEPR show a single quenching signal which increases in intensity with increasing microwave power. Hence this signal is from a true electron paramagnetic resonance. The change in peak intensity with microwave power is shown in Figure 6.3, where the peak-to-peak values are normalised to the full power (0 dB) spectrum. Lin-

ear fits to the data indicate that no power saturation is occurring.

6.1.3 Effect of Ageing

A pristine PFO OLED (RS164) was turned on in a flow of nitrogen and the high-field EDEPR spectrum monitored as the OLED degraded. A sequence of spectra is given in Figure 6.4.

A clear phase reversal of the peak occurs between 4 and 5 hours of OLED operation, where the resonance changes from current-quenching to current-enhancing. The g -values for the quenching and enhancing resonances are 2.0034 ± 0.0007 and 2.0033 ± 0.0004 respectively.

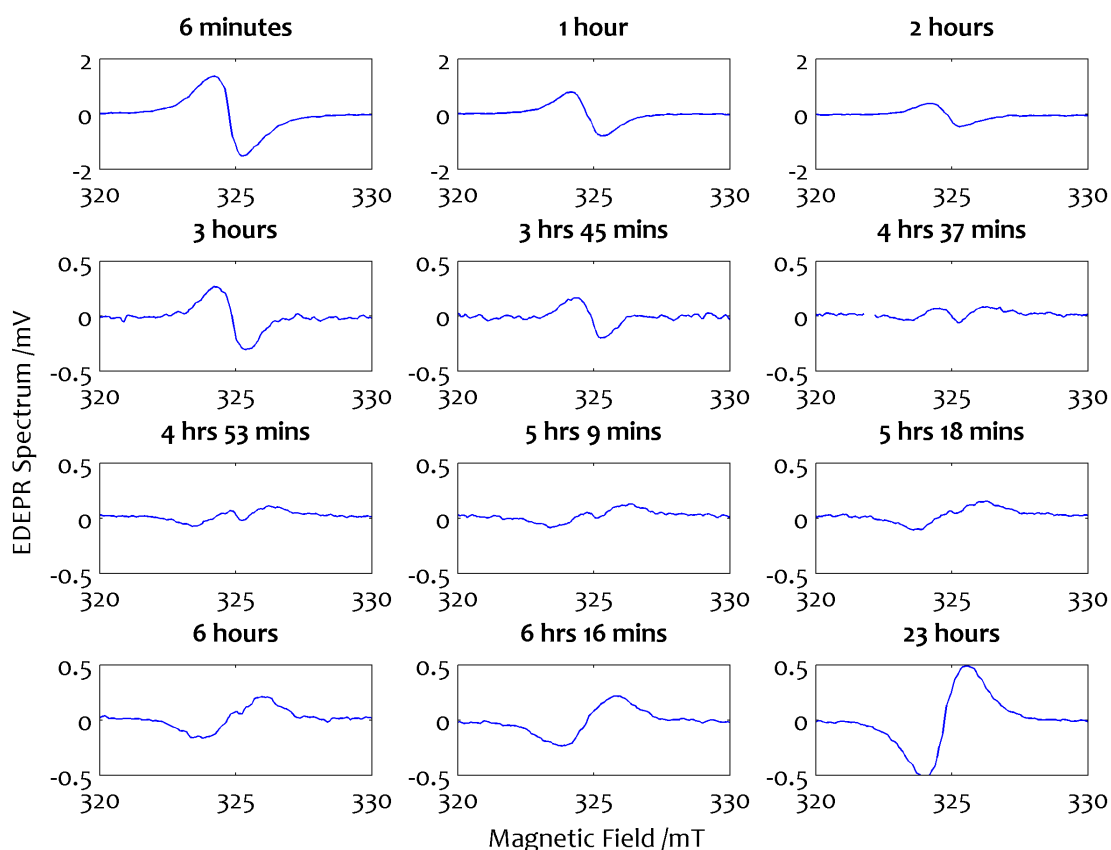


Figure 6.4: Representative EDEPR spectra from throughout the 25-hour-long series of measurements. A switch in phase of the peak occurs between 4 and 5 hours of OLED operation. Spectra were taken at room temperature using the PFO OLED RS164, with a microwave power of 80 mW and a microwave frequency of 9.1061 ± 0.0001 GHz.

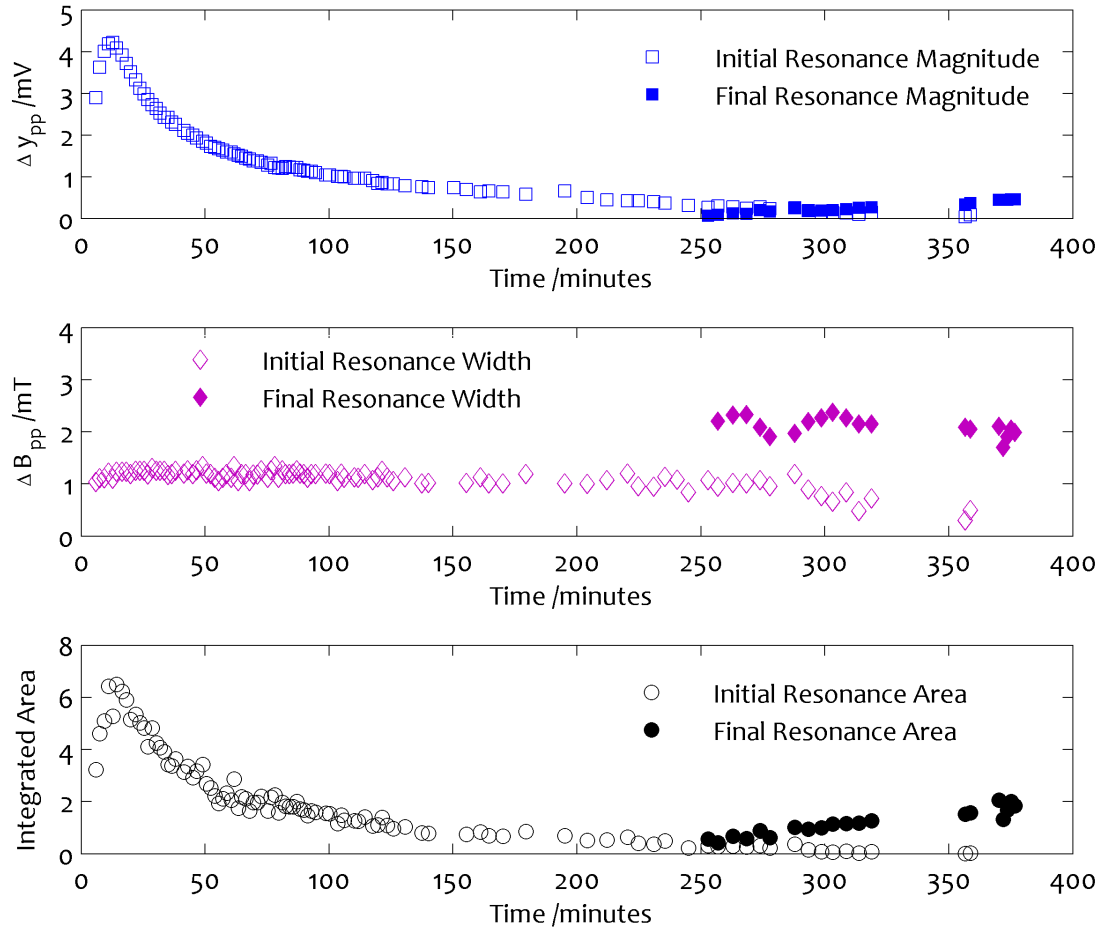


Figure 6.5: Changes in the peak-to-peak magnitude Δy_{pp} and width ΔB_{pp} and the integrated area (arbitrary units) of EDEPR spectra of a PFO OLED (RS164) due to operational ageing. A transition occurs after 4 hours of OLED operation. Note the different widths of the initial quenching resonance and final enhancing resonance.

Peak-to-peak magnitudes and widths, and the integrated area were calculated from these spectra¹ and are shown in Figure 6.5.

The integrated area A is calculated using

$$A = K \frac{\Delta y_{pp}}{2} \left(\frac{\Delta B_{pp}}{2} \right)^2 \quad (6.1)$$

where K is a constant, Δy_{pp} is the peak-to-peak magnitude, and ΔB_{pp} is the peak-to-peak width [88]. The integrated area is proportional to the number of

¹These data were obtained using Gaussian fits to the spectra, and for several of the spectra at least one Gaussian was required for a close fit.

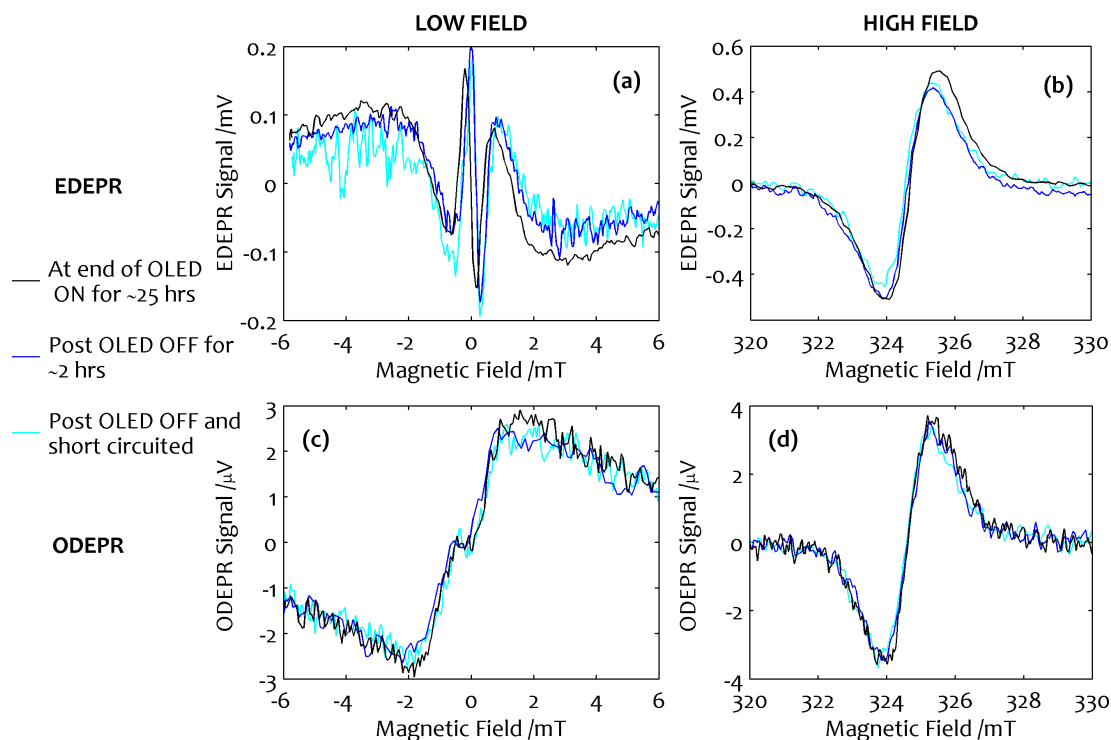


Figure 6.6: Low field (left) and high field (right) spectra with electrical (top) and optical (bottom) detection for an aged PFO OLED (RS164) subjected to various tests. Spectra were taken at room temperature, with a microwave power of 80 mW and a microwave frequency of 9.1062 ± 0.0001 GHz.

spins undergoing resonance.

Both the integrated area and peak-to-peak magnitudes initially rapidly increase, then decrease more slowly until the initial quenching resonance dies away and an enhancing resonance appears after ~ 250 minutes. The final enhancing resonance is broader than the initial quenching resonance, indicating that the centres associated with the signals have different environments.

After the OLED (RS164) had been ON for 25 hours, high and low field signals for both EDEPR and ODEPR were measured, and then the OLED was subjected to a few tests to determine whether the ageing was reversible. The spectra are shown in Figure 6.6. First the OLED was turned OFF and left for 2 hours, then remeasured, with no significant changes apparent. To see if the ageing was due to trapped charge polarisation of the OLED, the OLED was

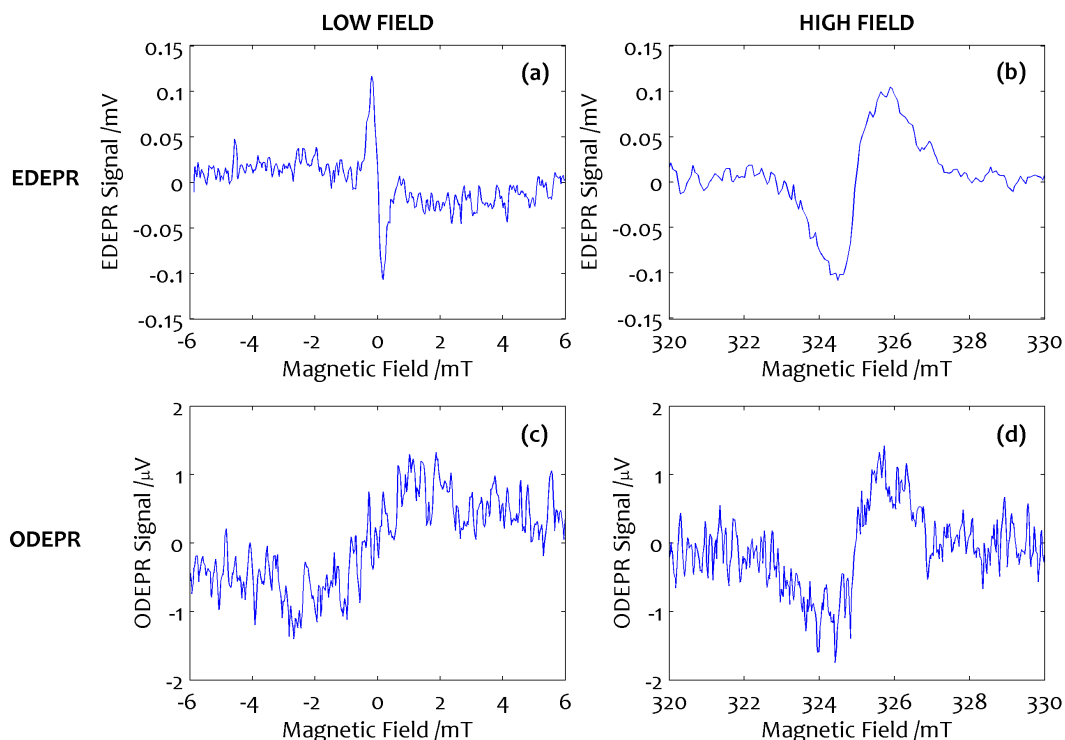


Figure 6.7: EDEPR and ODEPR spectra of a PFO OLED (RS164) after storage in a nitrogen glove box for one week post operational ageing. Spectra were taken at room temperature, with a microwave power of 80 mW and a microwave frequency of 9.1057 ± 0.0001 GHz. OLED: RS164.

then turned OFF and short-circuited for 40 minutes, again with no apparent change in the spectra. These experiments suggest that the ageing was irreversible on this time scale.

Of note is the comparison of each spectrum in Figure 6.6 with the corresponding spectrum in Figure 6.2. These two sets of data are from two OLEDs, RS164 and RS160 respectively, with the same structure and from the same fabrication batch. The ODEPR signals in 6.2(c) and in 6.6(c) are very similar, and likewise for the plots with label (d). In contrast, the EDEPR low field signals in 6.2(a) and 6.6(a) are markedly different, with two signals superimposed in the former, and three in the latter. This will be discussed further in Section 6.1.5.

This OLED was then kept in the glove box and remeasured after a week, giving the spectra shown in Figure 6.7. In the EDEPR spectra the phase reversal

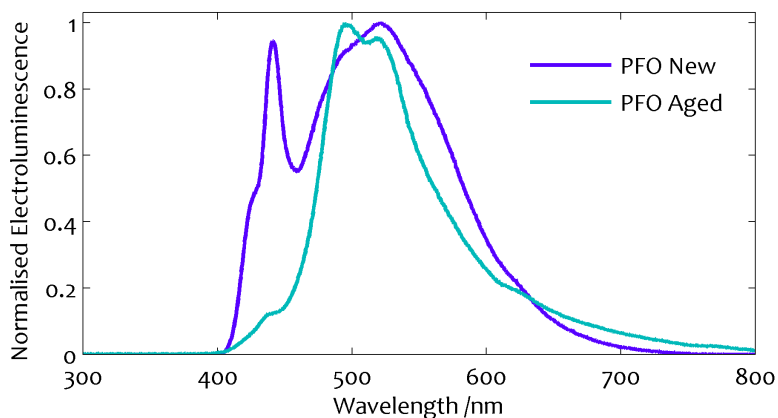


Figure 6.8: Electroluminescence spectra of new and aged PFO OLEDs.

at high field and the new sharp resonance at low field persist. All four of these spectra show greatly reduced signal-to-noise ratios (compared with the spectra in Fig. 6.6 which were taken at the end of a continuous measurement sequence). This type of signal degradation was also observed for other PFO OLEDs that had been exposed to the atmosphere. Noise in the ODEPR spectra would obscure any narrow resonance that may be present at zero field.

6.1.4 Electroluminescence of the Aged OLED

The electroluminescence of the aged OLED (RS164) was measured to see if there was any change in emission due to ageing. A comparison of the electroluminescence of a new PFO OLED (RS152, from Fig. 5.12) and the aged PFO OLED is presented in Figure 6.8.

The aged PFO OLED electroluminescence exhibits a blue-green emission near 500–520 nm which is characteristic of a keto defect (see Fig. 5.13) [81]. Comparing this with the spectrum of the new PFO OLED suggests that the electroluminescence of the new PFO OLED is a composite of electroluminescence from PFO and from keto defects. Hence either the keto defect is the dominant recombination centre and/or most of the PFO has been converted to the keto

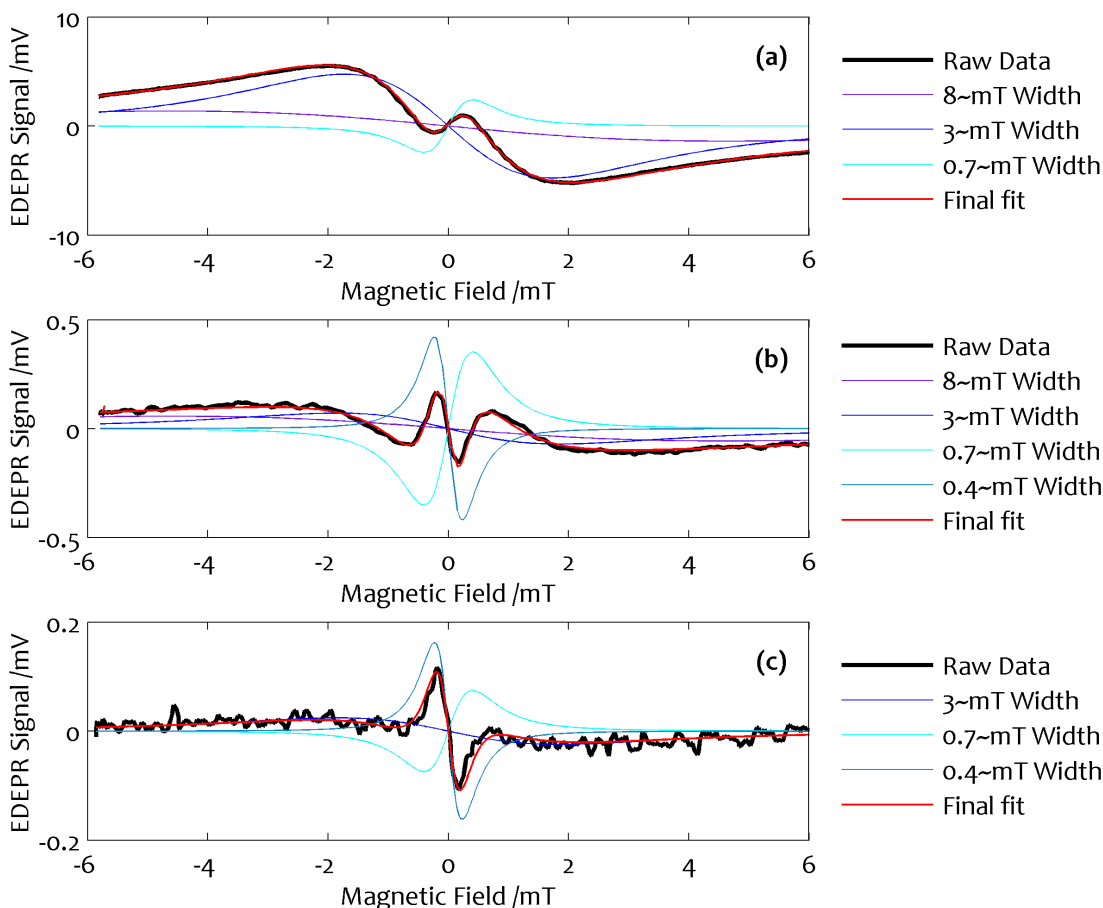


Figure 6.9: Fits to low field data for (a) a new PFO OLED (RS160), (b) a PFO OLED (RS164) after 25 hours of operation, (c) the aged PFO OLED (RS164) after storage for 1 week. Data are from Figures 6.2(a), 6.6(a), and 6.7(a) respectively. The final fit is the sum of the Lorentzians of different widths.

defect form during the 25 hour operational degradation experiment.

6.1.5 Analysis of the Low Field Signals

The low field EDEPR signals in Figures 6.2(a), 6.6(a), and 6.7(a) may each be decomposed into several Lorentzian lines, all centred on zero magnetic field but with varying width. The widths and amplitudes of Lorentzians forming the composite signals are shown in Table 6.1, and fits to the data are shown in Figure 6.9. Completely unconstrained fits were not unique due to the flexibility afforded by the number of composite lines. Hence the fitting was constrained by assuming four component lines of fixed linewidth.

Description	Component	Linewidths \rightarrow				Ratio
		8 mT	3.3 mT	0.7 mT	0.4 mT	
New OLED	Fig. 6.2	17	22	-2.6	0	6.5 : 8.5 : -1 : 0
25 hrs ON	Fig. 6.6	0.7	0.35	-0.38	0.26	1.8 : 0.9 : -1 : 0.7
1 wk storage	Fig. 6.7	0	0.12	-0.08	0.1	0 : 1.5 : -1 : 1.25

Table 6.1: Amplitudes (arbitrary units) of Lorentzian lineshapes with given linewidths in the decompositions of the low field signals from the respective figures. Ratios with the enhancing lineshape amplitude are shown for comparison.

6.1.6 Summary

A high field quenching EDEPR resonance at $g = 2.003 \pm 0.001$ was found for PFO OLEDs. This resonance increased in intensity in the first few minutes of operation but then decayed over several hours to a few percent of its initial value. The linewidth remained the same during this time.

After about 4 hours of operation, an enhancing resonance of opposite sign and larger linewidth appeared and grew steadily with time. This effect was not observed in the ODEPR high field resonance.

The low field signal showed a broad quenching resonance with a narrow enhancing resonance superimposed, in both the EDEPR and the ODEPR. After a long period of operation a third signal appeared in the EDEPR which was even narrower, and quenching. This additional signal was not observed in the ODEPR. These effects were independent of microwave power and so are magneto-resistance (MR) and magneto-electroluminescence (MEL) effects rather than EPR.

6.2 Discussion

6.2.1 The High Field Signal at $g = 2$

The observation of a signal near $g = 2$ at room temperature and with conventional EPR as well as EDEPR and ODEPR is consistent with a signal arising from a free-radical (a molecule with an unpaired electron in a dangling bond). Free radicals may be involved in polymerisation reactions and have been previously suggested [58,60] as playing a role in device degradation. A free radical EPR spectrum would usually be characterised by a fingerprint hyperfine pattern (reflecting the number and location of hydrogens for which the electronic wavefunction has a finite value at the hydrogen nucleus). However for solid polymer films the anisotropic hyperfine pattern is averaged out to a broad lineshape with little structure, as observed here.

In Figure 6.5 an initial rise in EDEPR signal intensity is observed. This may be due to an increase in the free radical concentration as energetic electrons and holes are injected into the organic layers of the OLED.

The J-V characteristics suggest that the current flow is space-charge limited. This may be determined by a variety of traps of various depths, including a particular free radical which is affected by oxygen-induced degradation and chemically converted to some other species. Oxygen may already be present in the polymer film due to preparation in air. However the ITO layer was cleaned with an oxygen plasma, which leaves a residual layer of active oxygen within and between the ITO and the PEDOT:PSS layers. This oxygen may diffuse through the PEDOT:PSS layer into the PFO layer during operation, decreasing the concentration of the EDEPR-active free radicals [59].

From Figure 6.5 it is evident that after 4 hours of operation, a new EDEPR spec-

trum appears, of opposite sign, different linewidth, and similar g -value. This may coincide with the arrival of the diffusing oxygen near the recombination zone, which will be close to the Al electrode and a somewhat different chemical environment. The effect of the diffusing oxygen, and/or the recombination energy, and/or the different chemical environment, is that a new free radical species is generated in the recombination zone. This is supported by the different linewidth of the new spectrum, which indicates a different number or distribution of hydrogen atoms, and the different electroluminescence spectra pre- and post-ageing (Fig. 6.8), which indicates chemical changes in the recombination zone. The free radical in this case is acting as a non-radiative recombination centre, which enhances the recombination rate and hence the current flow, but removes charge carriers which could contribute to radiative recombination and hence quenches the luminescence.

The changes in the electroluminescence are characteristic of keto defects. However a keto defect is a luminescent centre and is NOT a free radical, suggesting that the free radical may instead be a by-product of the keto defect formation reaction. Indeed, for every keto defect formed there are two hydrocarbon chains released from the polymer, which could exist as free radicals in the emissive layer (see Fig. 5.13). In the absence of clear hyperfine structure, the specific nature of these free radicals cannot be resolved.

6.2.2 A Possible Spin-Dependent Mechanism

Recalling the models presented in Chapter 2 (Sec. 2.2), a tentative model is presented here for the spin-dependent trapping by the free radicals discussed above. A schematic diagram is provided in Figure 6.10.

Before trapping, the free radical R is electrically neutral and inert in the poly-

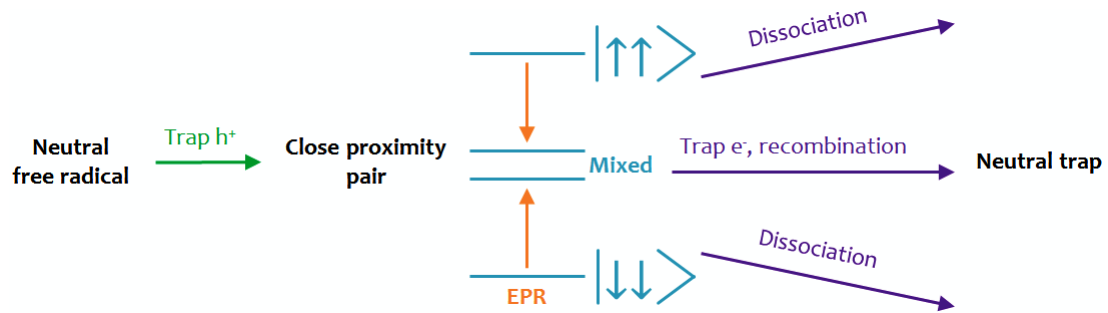


Figure 6.10: A possible spin-dependent recombination mechanism involving free radicals and polaronic holes. The close proximity pair may form a charged trap (spin-dependent), which may remain as a charged trap or may then trap an electron to return the neutral trap if conduction electrons are present.

mer matrix. The free radical may attract a polaronic hole to form a molecular ion R^+ representing the filled trap. As a precursor, the free radical R and the hole may exist as a close-proximity pair. In a magnetic field there are four possible spin states for this pair, three triplet states and one singlet state:

$$\begin{array}{l} \text{Triplet} \\ \text{Singlet} \end{array} \left\{ \begin{array}{ll} |1, 1\rangle = |\uparrow\uparrow\rangle & E = 1/2(g_1 + g_2)\beta B \\ |1, 0\rangle = (1/\sqrt{2}) [|\uparrow\downarrow\rangle + |\downarrow\uparrow\rangle] & E = 0 \\ |1, -1\rangle = |\downarrow\downarrow\rangle & E = -1/2(g_1 + g_2)\beta B \\ |0, 0\rangle = (1/\sqrt{2}) [|\uparrow\downarrow\rangle - |\downarrow\uparrow\rangle] & E = 0 \end{array} \right.$$

Or equivalently the $M_S = 0$ states may be written as mixed singlet and triplet states:

$$\begin{aligned} |\uparrow\downarrow\rangle &= (1/\sqrt{2}) [|1, 0\rangle + |0, 0\rangle] \\ |\downarrow\uparrow\rangle &= (1/\sqrt{2}) [|1, 0\rangle - |0, 0\rangle] \end{aligned}$$

Of these states, the two $M_S = \pm 1$ states cannot result in the formation of the molecular ion due to spin conservation. Therefore these states can only remain as a close-proximity pair, or dissociate. If each of the four states are generated at the same rate, the steady-state populations of the $M_S = 0$ pair states should therefore be less than that of the $M_S = \pm 1$ states.

In this situation the effect of EPR will be to pump populations from the non-

combining $|1, \pm 1\rangle$ triplet states to the combining $M_S = 0$ states and thus increase the rate of trapping. This will result in an increase in the trapped charge R^+ and a decrease in the free hole current, which is seen as a quenching EDEPR signal. As this same current results in light output at the recombination zone, the EPR will also decrease the luminescence and hence give a quenching ODEPR signal.

The R^+ ion could also act as a recombination centre for electrons, but this is unlikely as these ions are formed on the positive side of the recombination zone where there are very few electrons.

The second resonance in Figure 6.5 is thought to arise from an oxygen-generated free radical R_O in the recombination zone. In this case, if EPR leads to an increase in R_O^+ , then this can attract an electron, giving rise to additional recombination which is non-radiative. This increases the current and hence gives an enhancing EDEPR signal, but at the same time detracts from the radiative recombination which decreases the luminescence and is seen as a quenching ODEPR signal. This mechanism accounts for the high field signals seen in Figures 6.2, 6.6, and 6.7 but further experiments are required to test the validity of this model.

6.2.3 The Low Field Signal Near $B = 0$

The signals at low field in Figures 6.2, 6.6, and 6.7 are not true EPR effects because they are independent of microwave power. Instead they are magneto-electroluminescence (MEL) and magneto-resistance (MR) effects.

The current hypothesis for MEL and MR is based on the observation that it occurs at very low magnetic fields, where the magnetic field is so low that

the hyperfine interaction is comparable with the Zeeman interaction and so hyperfine-induced spin mixing is possible. This hypothesis is supported by the study by Nguyen *et. al.* [37] discussed in Section 3.3 where a clear difference in MEL was seen upon replacing H atoms with D atoms in a sample: hydrogen and deuterium have different hyperfine interaction constants and nuclear spins ($I_H = 1/2$ and $I_D = 1$). The MEL is of significant practical interest as the light output may be increased by $\sim 10\%$ by applying small (5–10 mT) magnetic fields. For example it may be possible to use very stable OLEDs with known MEL to map the pattern of surface magnetisation on a hard disk.

In this project the observed MEL was similar to that found by Nguyen, with a narrow (0.7 mT wide) enhancing signal superimposed upon a broad (>3 mT wide) quenching signal. The MR signal initially showed the same features (Fig. 6.2). However after electrical degradation, a third signal appeared (Fig. 6.6) which was intense and quenching, and even narrower (0.4 mT wide). After storage for one week the ratio of these signals changed, with reduced contribution from the enhancing signal compared with the quenching signals.

These results are unusual, as an explanation consistent with the hyperfine interaction would require the pattern of narrow and broad signals, as observed and interpreted by Nguyen *et. al.* [37], to scale up or down together with degradation as only a single centre is involved. This is contrary to the observation here. Hence a more complex explanation than that given for the high field resonances may be required here.

Chapter 7

Conclusions

This chapter presents a summary of the key results and developments in this project, followed by suggestions for further work to clarify and extend these results, and a brief outlook to conclude the thesis.

7.1 Summary

A process has been developed and refined for fabricating OLEDs of the form ITO/PEDOT:PSS/Emissive Layer/Al/Ag, where the PEDOT:PSS layer is optional, with three emissive materials PVK:OXD-7:Flrpic (PB), PFO, and F8BT. These devices were fabricated in air and with a geometry customised for EPR measurements. Critical features for satisfactory devices were found to be a sufficiently thick organic layer, and minimal exposure to the air.

These OLEDs produced electroluminescence with spectra in agreement with literature results. The spectrum from a PFO OLED showed signs of partial degradation due to the formation of keto defects. Emission was visible to the naked eye above 12 V and 25 V for the phosphorescent PB and fluorescent PFO

blue-emitting OLEDs respectively.

Hardware and software have been developed which permits simultaneous measurements of I-V and EL-V curves in an inert glove box environment over a range of ± 9 V. The range for positive voltages may be easily extended to 0–27 V. Both PB and PFO OLEDs showed space-charge-limited conduction behaviour with significant trapping. A gradual decrease of the EL and current during operation was noted, with partial recovery following a period of rest. This behaviour was recorded for a PB OLED and observed to be of a similar nature for the PFO OLEDs.

Both ODEPR and EDEPR signals were observed for PFO OLEDs at both low and high fields. The low field signals are independent of microwave power and so are attributed to magneto-electroluminescence (MEL) and magneto-resistance (MR) effects. Both of the MEL and MR signals show a composite broad quenching and narrow enhancing response around $B = 0$. No change was observed in the MEL following operational ageing. In contrast, a third, narrow quenching line was observed in the MR and the ratio of the initial two MR responses changed substantially with ageing. This changed ratio of broad and narrow components after ageing is inconsistent with the interpretation of Nguyen *et. al.* [37]. Hence these results were unexpected and may require a more complex explanation than the hyperfine-induced spin mixing explanation found in the literature.

The high field signals increased with increasing microwave power so were true EPR signals. These quenching resonances were easily observed at room temperature as a single line with g -value of 2.003 ± 0.001 , which is very close to the free-electron g -value. A very weak line with the same g -value was also observable in the conventional EPR spectra of the PFO OLED (ON and OFF).

Operational ageing was observed over a period of ~ 24 hours by monitoring the EDEPR spectrum around $g = 2$. The initial quenching resonance rapidly increased and then gradually decreased in intensity. After 4 hours of operation an enhancing resonance appeared and slowly increased in intensity. The different linewidths of these two resonances indicate that they are indeed different resonances. The initial quenching EDEPR and ODEPR signals during device operation are ascribed to spin-dependent trapping at a free radical which leaves the free radical as a charged spin-0 molecular ion. This also affects the current flow and light emission through its role as trapped charge, as confirmed by space-charge limited J-V data. The enhancing EDEPR signal observed after several hours of operation is attributed to a second free radical, generated in the recombination zone, which acts as a non-radiative recombination centre.

The EL spectrum of the aged PFO OLED indicated significant keto defect formation, and the degradation was found to be irreversible. The ageing is attributed to chemical changes in the OLEDs rather than damage solely caused by the recombination energy. A possible explanation for these effects is the diffusion of oxygen through the device from the oxygen-plasma-treated ITO.

Measurements of OLEDs with minimal electrical degradation but similar times in the EPR spectrometer revealed no ageing of this kind. Rather, the EDEPR signal gradually weakened and eventually disappeared as the OLED became less electrically stable. Storage in inert atmosphere also reduced the signal-to-noise ratio of the EDEPR signal in a similar way. This suggests that there are two different degradation processes occurring; that which occurs during operation and that which occurs due to residual trapped gas.

A working model has been tentatively proposed which can explain the ob-

served effect as spin-dependent trapping and recombination at free radicals, although this model requires further experimentation to test its validity.

7.2 Further Work

Due to time constraints and sample availability, the electrical degradation of only one PFO sample was studied. Ideally several more PFO OLEDs should be studied under the same conditions, and with strategic variations. For example it would be useful to confirm the interpretation of spin-dependent trapping by constructing devices which are unipolar in operation and free of recombination effects. This would require an appropriate choice of cathode which is electron blocking (e.g. gold). In this case there would be no observable ODEPR, but there should still be observable EDEPR. Bipolar and unipolar devices could also be used to test alternative degradation mechanisms such as light-induced degradation.

The optimisation of the devices would most likely be limited given the fabrication process in air, and the impracticality of using reactive low work function cathode materials such as calcium in air. Nevertheless, some improvements to the device fabrication could include the addition of a thin layer of an electron-injecting material such as LiF, CsF, or MgO before the Al cathode. For devices with hole-dominated charge transport this would improve electron injection and so lower the operating voltage [76,89]. Further reduction in operating voltage could come from reducing the emissive layer thickness, although this would also increase the likelihood of pinhole formation.

The hypothesis that oxygen-induced formation of free radicals gives rise to the enhancing resonance could be tested by a study which varies the length of

time the OLED is exposed to oxygen, both in the atmosphere and in the oxygen plasma treatment. If the oxygen is indeed diffusing from the oxygen-plasma-treated ITO, omitting this step should significantly reduce or even preclude formation of the second free radical. If possible, measurements of the amount of adsorbed oxygen and water in the organic layers would provide additional insight, as would chemical analysis of the aged OLED. Other parameters that should affect the appearance of the enhancing resonance are the total layer thickness, and the presence of the PEDOT:PSS layer¹.

Also, it may be possible to generate the free radicals by X-ray irradiation, and then examine them with EDEPR. This would be done most simply in unipolar devices, and may reveal information about the two different free radicals. Reverse bias measurements may also provide interesting EDEPR and ODEPR spectra.

Other related experiments are possible, which may provide complementary information. For example, it was noted that the emission was spatially uneven across the active area, with brighter edge regions. The optically and electrically detected EPR effect could be 'mapped out' across the active area surface with a high-resolution camera to see if the effect is location-specific.

For any further time-dependent operational ageing experiments it would be beneficial to record, as functions of time, the EDEPR and ODEPR spectra at both high and low field and the spectral output $EL(\lambda)$ for several fixed voltages, as well as the I-V and EL-V characteristics. This would require considerable redesign of the experimental apparatus but would give a much more complete picture of the processes occurring during operational degradation. It would also be useful to extend the voltage range of the LIV Tracer to measure

¹This parameter may prove problematic as OLEDs with only a PFO layer had even higher turn-on voltages so may not be as stable.

the VUW-made OLEDs as described in Section 4.1.3.

The fixed modulation frequency for each EPR method was chosen during preliminary experiments to give maximal signals. Measuring the modulation frequency dependence of the signal (e.g. both the in-phase and out-of-phase components) may provide further information, for example the composite low field signals may show different phase dependence and hence be able to be separated in phase [90].

A low-temperature study may be of interest, for three reasons. Firstly it may reduce line broadening due to spin-lattice relaxation, so may enable hyperfine structure to be resolved². Secondly, the intensity versus temperature data could be used to test the validity of the proposed recombination models, as mechanisms such as dissociation have an associated temperature dependence. Thirdly, there may be completely different EPR effects in short-lived states such as excitons that could be observed at low temperatures.

A comprehensive study on the phosphorescent OLEDs would be of considerable interest, as phosphorescent OLEDs are much more efficient and of current commercial interest. The triplet emission should have a very different spin-dependent mechanism (see [91]) and a comparison with PFO may also provide some clarity regarding the radical species present in PFO. The phosphorescent OLEDs have a higher electroluminescent intensity (when compared with PFO OLEDs at the same operating voltage), and so the ODEPR can be measured at a lower operating voltage which may prolong the life of the device.

²However orientational broadening due to the amorphous polymer film may still prevent observation of any hyperfine structure.

7.3 Outlook

This project has shown that it is possible to detect EDEPR and ODEPR signals from OLEDs made in air, and that the degradation of these devices may be observed within the time-scale of a day. The process for OLED fabrication that has been established at VUW can be easily adapted to make use of new materials, and the home-built EPR spectrometer is also readily customisable, for example for the further work discussed above. The mechanisms of spin-dependent recombination are under active debate in the literature, and so it is anticipated that these techniques and apparatus described here will form the nucleus of a new activity at VUW which may make a substantial contribution to OLED research.

Appendix A

LIV Tracer: Design Details

A.1 Sample Holder Design

A sample holder was designed to hold and make contacts to the OLED during measurements with the LIV Tracer. The design is outlined in Figure A.1 and a diagram depicting the light collection geometry is provided in Figure A.2. Photographs of the finished holders are shown in Figure A.3. Two gold-coated pads which contact the ITO and Al electrodes of the OLED are attached to a piece of Veroboard and held in place by the two screws on the right-hand side. These screws connect the contact pads to the circuit inside the box, as well as securing the holder to the die-cast box. Mini crocodile clip connections were added to the Veroboard to enable quick connections to OLEDs with existing wire contacts.

The Darmstadt PPV OLEDs are encapsulated, 5 mm longer than those made at VUW, and mostly with existing wire contacts. The holder for these OLEDs needs only crocodile clip connections; the gold-coated contact pad presses on the encapsulating layer to hold the OLED in place.

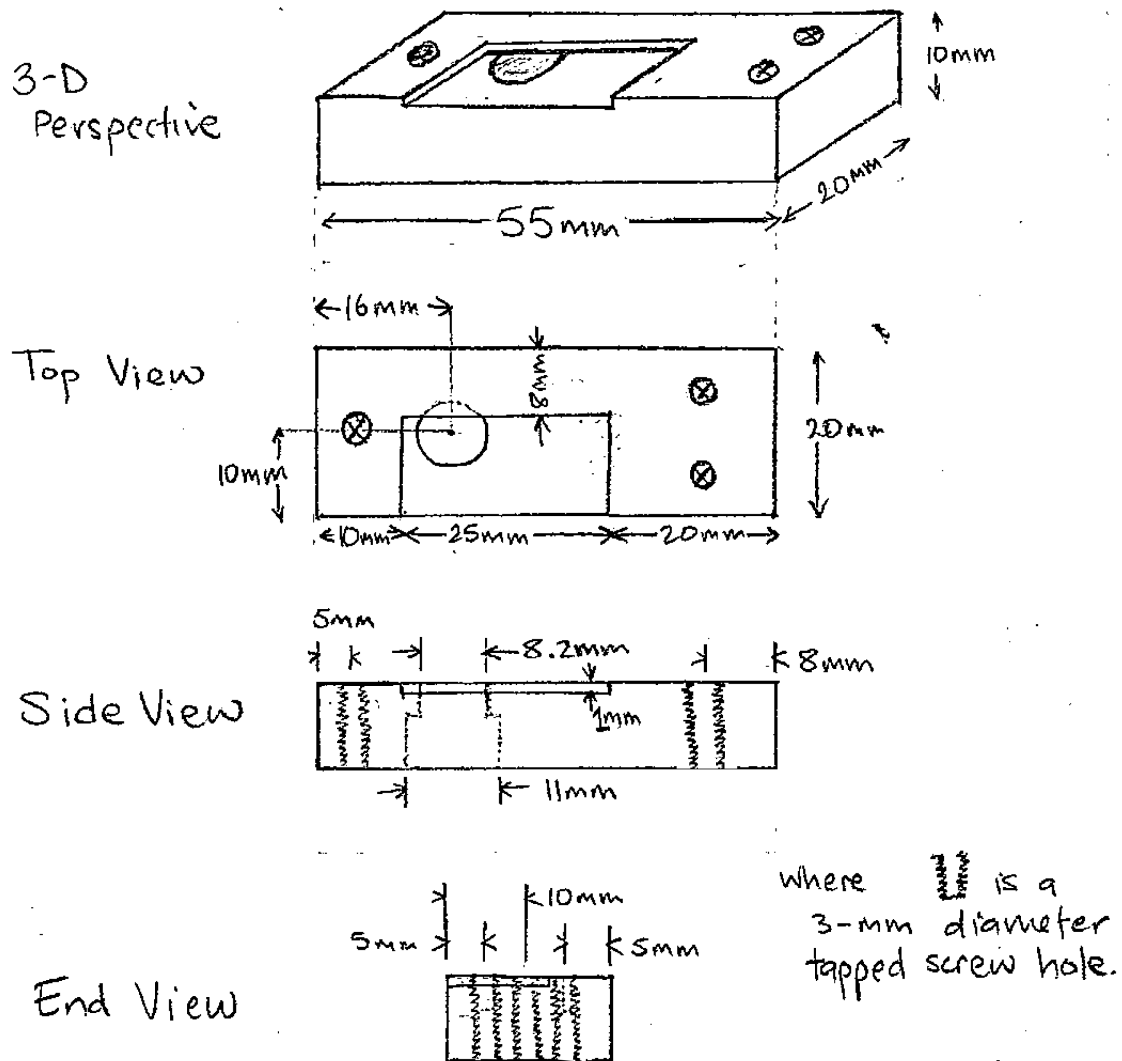


Figure A.1: Holder designed for the OLEDs fabricated at VUW. Diagram approximately to scale. The sample holder for the Darmstadt diodes is almost identical except that it is longer by 5 mm to accommodate the 30 mm Darmstadt diodes.

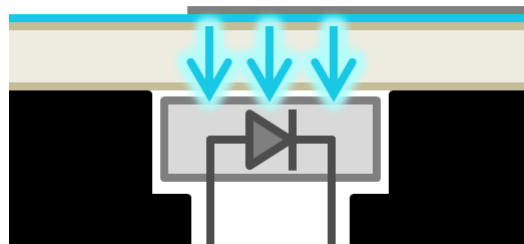
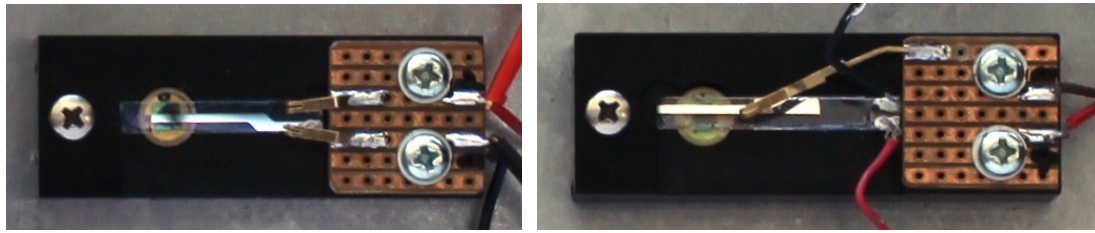


Figure A.2: A diagram of the light collection geometry for the LIV Tracer. The silicon photodiode is located directly under the centre of the light-emitting region of the OLED.



(a) Holder for VUW OLEDs, with OLED included. (b) Holder for Darmstadt OLEDs, with OLED included.

Figure A.3: OLED holders for (a) OLEDs fabricated at VUW, and (b) OLEDs fabricated in Darmstadt.

A.2 Electronic Circuit Block Diagram

The electronic circuit for the LIV Tracer may be represented by a block diagram, as shown in Figure A.4.

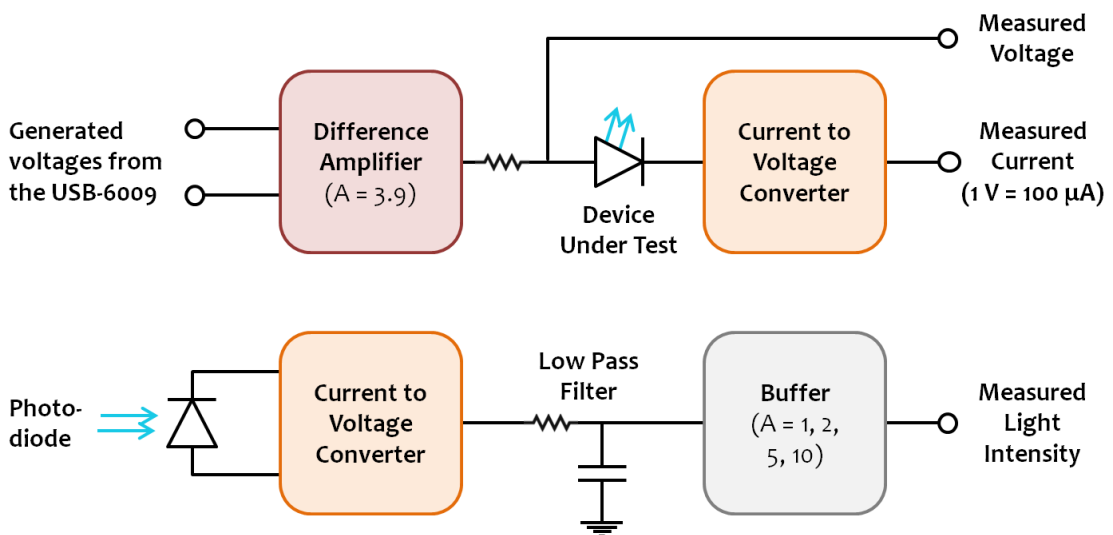


Figure A.4: A block diagram for the electronic circuit shown in Figure 4.2.

A.3 LabVIEW Program for the LIV Tracer

The LabVIEW program itself is called a 'virtual instrument' (VI), and is viewed as a pictorial block diagram which is read from left to right. The block diagram is shown in Figure A.5. A flat sequence structure (the outermost grey film-strip frames) is used to separate the program into two parts that run sequentially.

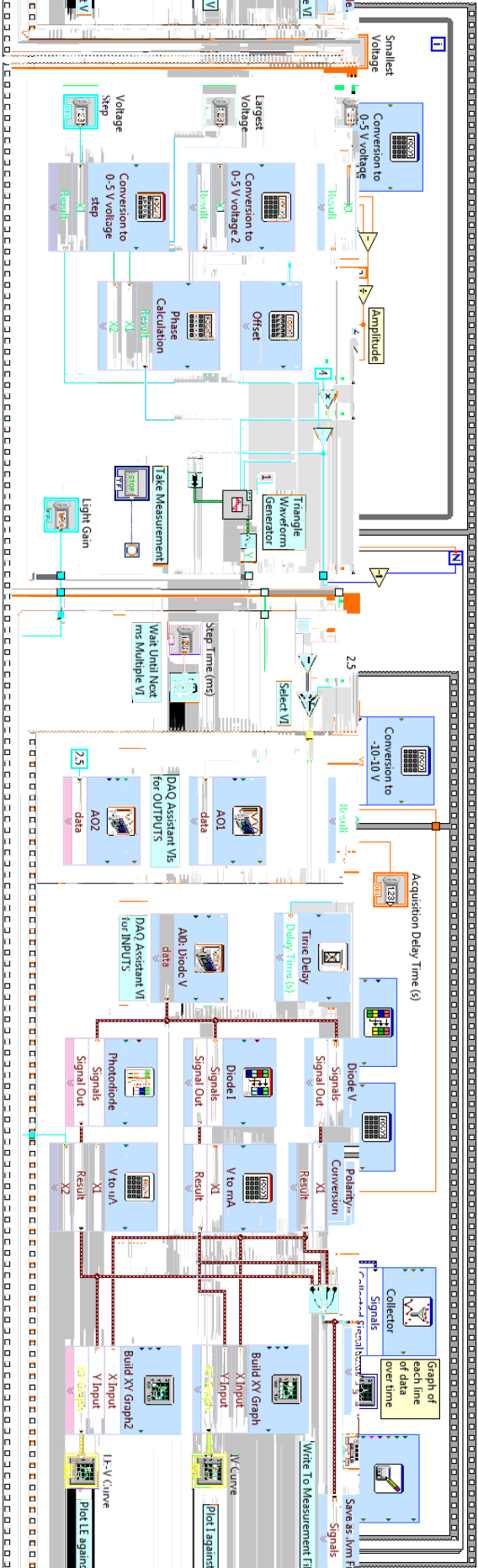


Figure A.5: The block diagram that controls the flow of the program. The first frame (left-most grey box) generates a triangle waveform of the desired range and step size. This is sent to the second frame (second grey box) which has a subframe that controls communication with the output device. A second subframe then waits for a specified time before acquiring data which is plotted on the graphs on the front panel and saved to a .lvm file.

In the first frame a triangle waveform is generated, which is used in the second frame to apply a series of stepped voltages to the diode. On the far left the maximum, minimum and step size values of the applied voltage are linked to user controls, for which numeric inputs are provided by the front panel. The small grey box is the triangle waveform generator VI, and the rest of the boxes are formula VIs that convert the numbers from the user inputs into amplitude, phase, offset and sampling information for the triangle waveform generator. Here the equations in the formula VIs manipulate the triangle waveform so that the output voltage across the diode always starts at zero, steps up to the maximum voltage, down to the minimum voltage, and back to zero, with the desired voltage step.

There is a subtlety here: As discussed in Section 4.1.1 the voltage across the diode is the amplified voltage difference across TP1 and TP2, two output pins of the USB-6009. Two voltage output pins are needed in order to generate negative voltages because the voltage at each pin is restricted to the range 0 to 5 V. Here we use one varying output of between 0 and 5 V and one constant output of 2.5 V so that the difference between the two voltages ranges from -2.5 V to $+2.5$ V. This voltage difference is then amplified ~ 4 times by U1 to give a -10 V to $+10$ V voltage across the diode. Thus the very first set of VIs in the first section convert the -10 V to $+10$ V user input voltages to the corresponding value between 0 to 5, where 0 V corresponds to 2.5, 10 V to 5, etc. The triangle waveform is then generated in the range 0 to 5, and the output converted in the second frame of the program.

The second frame will start running when the Take Measurement button (on the front panel) is pressed and all of the VIs contained within the second frame have the information they need. Here the second frame saves measurement

data to a file, so a file dialogue immediately opens requesting a file name. Once the program has this vital piece of information, the real measurement begins. This is a timed, iterative process, which is controlled by a Wait Until Next ms Multiple VI and another flat sequence structure within a For Loop. For each iteration, the triangle-shaped Select VI compares the current iteration number with the total loop count, N . If the iteration has reached $N-1$, the Select VI will send the value 2.5 to the first frame of the flat sequence, otherwise it will send the next data point in the triangle waveform that is waiting at the auto-indexed tunnel from the triangle waveform generator VI.

In the first frame of the flat sequence, two DAQ Assistant VIs send output information to the USB-6009 to create a voltage across the two analogue output pins of the USB-6009, which is then converted to a larger voltage across the diode by an operational amplifier. One DAQ Assistant has a constant value of 2.5 to send; the other calls the triangle-shaped Select VI to find out which output value to send. Also in this frame is a user-friendly VI that converts the output voltage back into the -10 V to $+10\text{ V}$ range for display on the Signals over Time graph on the front panel and writing to file.

The second frame of this flat sequence controls the measurement of diode voltage and current, and light output, using the analogue input pins of the USB-6009 in differential mode. The measurement is delayed by the Time Delay VI according to the value from a numerical user input on the front panel. The three measured signals are split and converted into true values depending on the amplification from the electronic circuit, then written to a .lvm (LabVIEW measurement) file and displayed on the front panel graphs.

Appendix B

OLED Fabrication: Spin Coating, Problem Solving and Final Process

B.1 Spin-Coating

In spin-coating, the substrate is secured in the centre of the spin-coater by vacuum suction (see Figure B.1). The polymer solution is pipetted onto the substrate to coat the entire surface. The spin-coater then spins the substrate, which pushes excess solution off the substrate and evaporates the solvent to leave a thin film of polymer. The film thickness is determined by the rate of revolution and the solution concentration. The desired combination of acceleration(s), speed(s) and time(s) is saved and run as a program.



Figure B.1: SPIN150 spin-coater from SPS Europe.

B.2 Problem Solving

Table B.1 summarises the main reasons for device failure, and how they were overcome in order to fabricate working devices.

Problem	Proposed Solution(s)	Result
Patterning of ITO with tweezers and cotton buds leaves a messy edge	Use a printed acetate mask and lithography to pattern ITO	ITO pattern neat, reproducible, and easily controllable
Polymer not dissolving in solvent	Increase dissolving time; Use a magnetic stirrer bar; Use a different solvent	Solutions dissolve well
Polymer films too thin, even with slow spin speed	Increase concentration of polymer	Film thickness controllable with spin speed
Air flow around substrate causes solvent to evaporate too fast, leaving an uneven film	Attach substrate to a microscope slide with carbon tape	Reproducibly smooth and even films
Short circuits from PE-DOT:PSS lumps in film or pinholes in emissive layer	Filter all solutions, make active area smaller and emissive layer thicker	High resistance light-emitting devices
Short circuits from punching through to PEDOT:PSS layer under electrode	Remove the excess PE-DOT:PSS film before spinning the emissive layer	High resistance light-emitting devices
Devices are fabricated in air which accelerates degradation of the device	Dry films in desiccator rather than on a hot plate and use a glove box for device storage	Longer-lasting light-emitting devices

Table B.1: Device fabrication trouble-shooting

B.3 OLED Fabrication Process

The successful fabrication process is outlined in the following set of steps:

B.3.1 Substrate Preparation

Cutting of Substrates to Size

1. Spincoat a protective layer of photoresist onto the conductive side (4000 rpm for 1 minute) and bake for 1 min at 95°C
2. Attach other side to backing pad with wax; secure on lever arm parallel with diamond saw blade
3. Cut to size using diamond saw (move 4.183 mm to get 18 strips with width of just under 4 mm)
4. Unstick, and smooth any sharp edges/corners with silicon carbide paper
5. Clean with acetone, dry with nitrogen gun (repeat if needed)

Etching of ITO Pattern

1. Use ohmmeter to check which side is coated with ITO
2. Spincoat a layer of photoresist onto the conductive side (4000 rpm for 1 minute) and bake for exactly 1 min at 95°C
3. Place under acetate mask in mask aligner and expose to UV for 11 s
4. Develop pattern in solution of 3:1 developer:water for 40 s
5. Check pattern has developed properly; if not, clean well with acetone and repeat photolithography steps
6. Etch with 37% HCl for 90 s and wash at least twice with DeI water

Cleaning of Substrates

1. Sonicate in DECON 90 5% using a high-power sonicator
2. Rinse with deionised water until no bubbles appear, then sonicate in clean deionised water
3. Sonicate in acetone, then in isopropanol
4. Expose to O₂ plasma for 15 s

B.3.2 Hole Transport Layer

1. Attach substrate to a microscope slide with carbon tape (ITO side upwards) and remove any loose particles with nitrogen gun
2. Place on vacuum chuck and ensure substrate is centered
3. Spread 50 μL filtered PEDOT:PSS onto the substrate (drop from micropipette)
4. Spin-coat at 3000 rpm for 1 minute
5. Remove excess film with tweezers and/or a cotton bud and isopropanol, leaving a film across the active area only
6. Dry in vacuum desiccator for at least 1 hour, ideally 2 hours

B.3.3 Emissive Layer

1. Dissolve solutions overnight:

Phosphorescent Blue Mix Dissolve 1 mg FlrPic, 4 mg OXD-7 and 10 mg PVK in 600 μL anhydrous chlorobenzene in an amber vial using a (thoroughly clean) magnetic stirrer

PFO Dissolve 15 mg/ml PFO in anhydrous chloroform in an amber vial using roller-based agitation

F8BT Dissolve 12 mg/ml F8BT in anhydrous chloroform in an amber vial using roller-based agitation

2. Filter using a 0.45 μm PVDF filter
3. Check substrate is secure on backing slide and remove any loose particles with nitrogen gun as before; secure on spin coater
4. Spread 45 μL filtered solution onto the substrate (drop from micropipette)
5. Spin-coat at 2000 rpm for 30 s
6. Remove film outside of active area with tweezers, leaving a smooth film which covers and extends $\sim 3\text{--}4$ mm past the PEDOT edge on each side
7. Dry in vacuum desiccator while preparing other samples and evaporator

B.3.4 Cathode

1. Place substrate(s) in substrate holder (use blanks if needed) and masking across the top of the electrode to match the ITO pad
2. Position electrode mask onto substrate
3. Screw together onto evaporation stage
4. Put into evaporator with Al and Ag evaporation sources and follow evaporator instructions. The pump down to 5×10^{-6} Torr takes 2 hours but is best if left overnight, and deposition takes ~ 10 – 20 minutes with a rate of ~ 2 Å/s
5. Deposit 100 nm of metal, preferably aluminium; a capping layer of silver may be used to reach the desired thickness if needed

B.3.5 Contacts

1. Cut a length of wire of about 50 mm. If insulated, remove ~ 6 – 8 mm of insulation at each end e.g. with solvent or with a scalpel, using a glass slide to press on. Bend the ends into hooks (~ 3 mm long, ~ 0.5 – 1 mm wide).
2. Attach to ends of ITO and Al/Ag electrodes with either pressed indium or silver paint:

Pressed indium contacts: Cut a small (~ 0.5 mm) slice of indium, melt it with a soldering iron on low heat, and wrap it around the hook to form a ball. Use the flat side of blunt tweezers (with teflon tape wrapped around them if needed) to gently press the ball onto the electrode until it forms a mechanical and electrical contact.

Silver paint contacts: Place the OLED in a suitable storage container. Position the contact wires in the container such that the hooks of the wires sit on the electrodes where contact is desired, without needing to hold them there. Move the wires away and put a small drop of silver paint onto the end of the electrode at the contact point. Reposition the hooks, ensuring full coating with the silver paint. Leave the contacts to dry for at least 30 minutes in a well-ventilated place where they will not be moved.

References

- [1] Weil, J. A., Bolton, J. R. & Wertz, J. E. *Electron Paramagnetic Resonance* (Wiley-Interscience, 1993).
- [2] Abragam, A. & Bleaney, B. *Electron Paramagnetic Resonance of Transition Ions* (Dover Publications, Inc., 1986).
- [3] Skotheim, T. A. & Reynolds, J. R. *Handbook of Conducting Polymers* (CRC Press, 2006), 3rd edn.
- [4] Nanomarkets. The latest advances changing the prospects for OLED materials (2013). URL http://nanomarkets.net/articles/article/the_latest_advances_changing_the_prospects_for_oled_materials.
- [5] Universal Display Corporation. Technology; OLED Marketplace (2012). URL www.universaldisplay.com.
- [6] Cambridge Display Technology. Technology Status (2013). URL www.cdtltd.co.uk/technology/status/.
- [7] Schwoerer, M. & Wolf, H. C. *Organic Molecular Solids* (WILEY-VCH, Weinheim, 2007).
- [8] LG Electronics. OLED TV by LG (2013). URL www.lg.com/au/oled-tv.
- [9] Liao, Z., Zhu, T., Mi, B., Gao, Z., Fan, Q. & Huang, W. Molecular iridium (III) complexes and their corresponding electrophosphorescent devices. *Huaxue Jinzhan* **23**, 1627–1643 (2011).
- [10] D'Andrade, B. White phosphorescent LEDs offer efficient answer. *Nature Photonics* **1**, 33–34 (2007).
- [11] Park, J., Shin, D. & Park, S. Large area OLED lightings and their applications. *Semiconductor Science and Technology* **26**, 034002 (2011).
- [12] Metalgrass Software. OLED-Info.com (2013). URL www.oled-info.com.
- [13] SAMSUNG. Samsung Galaxy Note II (2013). URL www.samsung.com/nz/consumer/mobile-phone/mobile-phone/galaxy-note/GT-N7100RWDNZC-spec.

- [14] Malliaras, G. & Friend, R. An organic electronics primer. *Physics Today* **58**, 53–58 (2005).
- [15] Boehme, C. & McCamey, D. *Investigating Spin-Dependent Processes in Organic Semiconductors*, 257–299 (CRC Press).
- [16] Baker, W. J., McCamey, D. R., van Schooten, K. J., Lupton, J. M. & Boehme, C. Differentiation between polaron-pair and triplet-exciton polaron spin-dependent mechanisms in organic light-emitting diodes by coherent spin beating. *Physical Review B* **84**, 165205 (2011).
- [17] Shinar, J. Optically detected magnetic resonance studies of luminescence-quenching processes in π -conjugated materials and organic light-emitting devices. *Laser & Photonics Reviews* **6**, 767–786 (2012).
- [18] Spaeth, J.-M. & Overhof, H. *Point Defects in Semiconductors and Insulators* (Springer, 2003).
- [19] Myers, J. D. & Xue, J. Organic semiconductors and their applications in photovoltaic devices. *Polymer Reviews* **52**, 1–37 (2012).
- [20] Jacoboni, C., Canali, C., Ottaviani, G. & Quaranta, A. A. A review of some charge transport properties of silicon. *Solid-State Electronics* **20**, 77–89 (1977).
- [21] Bredas, J. L. & Street, G. B. Polarons, bipolarons, and solitons in conducting polymers. *Accounts of Chemical Research* **18**, 309–315 (1985).
- [22] Singh, J. (ed.) *Optical Properties of Condensed Matter and Applications* (Wiley, 2006).
- [23] Pope, M. & Swenberg, C. E. *Electronic Processes in Organic Crystals and Polymers* (Oxford University Press, 1999), 2nd edn.
- [24] Atkins, P. & de Paula, J. *Atkins' Physical Chemistry* (Oxford University Press, 2006), 8th edn.
- [25] Rausch, A. F., Homeier, H. H. & Yersin, H. Organometallic Pt(II) and Ir(III) triplet emitters for OLED applications and the role of spin-orbit coupling: A study based on high-resolution optical spectroscopy. *Photophysics of Organometallics* **29**, 193–235 (2010).
- [26] Morrison, J. *Modern Physics: for Scientists and Engineers* (Elsevier Science, 2009).
- [27] Lépine, D. J. Spin-dependent recombination on silicon surface. *Physical Review B* **6**, 436–441 (1972).
- [28] Shockley, W. & Read, W. T. Statistics of the recombinations of holes and electrons. *Physical Review* **87**, 835–842 (1952).
- [29] Hall, R. N. Electron-hole recombination in germanium. *Physical Review* **87**, 387–387 (1952).
- [30] Boehme, C. *Dynamics of spin-dependent charge carrier recombination*. Ph.D. thesis, Fachbereich Physik der Philipps-Universität Marburg (2002).

- [31] D. Kaplan, I. S. & Mott, N. F. Explanation of the large spin-dependent recombination effect in semiconductors. *Journal de Physique Lettres* **39**, 51–54 (1978).
- [32] Rong, F., Buchwald, W., Poindexter, E., Warren, W. & Keeble, D. Spin-dependent Shockley-Read recombination of electrons and holes in indirect-band-gap semiconductor p-n junction diodes. *Solid-State Electronics* **34**, 835–841 (1991).
- [33] Solomon, I. Spin physics of recombination centers in amorphous silicon. *Journal of Non-Crystalline Solids* **35-36**, Part 2, 625–631 (1980).
- [34] McCamey, D. R., Lee, S.-Y., Paik, S.-Y., Lupton, J. M. & Boehme, C. Spin-dependent dynamics of polaron pairs in organic semiconductors. *Physical Review B* **82**, 125206 (2010).
- [35] Frankevich, E. L., Lymarev, A. A., Sokolik, I., Karasz, F. E., Blumstengel, S., Baughman, R. H. & Hörhold, H. H. Polaron-pair generation in poly(phenylene vinylenes). *Physical Review B* **46**, 9320–9324 (1992).
- [36] Swanson, L. S., Shinar, J., Brown, A. R., Bradley, D. D. C., Friend, R. H., Burn, P. L., Kraft, A. & Holmes, A. B. Electroluminescence-detected magnetic-resonance study of polyparaphenylenevinylene (PPV)-based light-emitting diodes. *Physical Review B* **46**, 15072–15077 (1992).
- [37] Nguyen, T. D., Hukic-Markosian, G., Wang, F., Wojcik, L., Li, X.-G., Ehrenfreund, E. & Vardeny, Z. V. Isotope effect in spin response of π -conjugated polymer films and devices. *Nature Materials* **9**, 345–352 (2010).
- [38] Jiang, W.-L., Cong, L., Meng, Z.-H., Wang, J., Han, Q., Meng, F.-C., Wang, L.-Z., Ding, G.-Y. & Gang, Z. The role of magnetic fields on organic light-emitting devices based on aluminum tris(8-hydroxyquinoline) (Alq3) at room temperature. *Wuli Xuebao* **59**, 3571–3576 (2010).
- [39] Wagemans, W. & Koopmans, B. Spin transport and magnetoresistance in organic semiconductors. *physica status solidi (b)* **248**, 1029–1041 (2011).
- [40] Niedermeier, U., Vieth, M., Patzold, R., Sarfert, W. & von Seggern, H. Enhancement of organic magnetoresistance by electrical conditioning. *Applied Physics Letters* **92**, 193309 (2008).
- [41] Hu, B. & Wu, Y. Tuning magnetoresistance between positive and negative values in organic semiconductors. *Nature Materials* **6**, 985–991 (2007).
- [42] Lupton, J. M. & Boehme, C. Magnetoresistance in organic semiconductors. *Nature Materials* **598** (2008).
- [43] Hu, B. & Wu, Y. Reply to “Magnetoresistance in organic semiconductors”. *Nature Materials* **7**, 598–599 (2008).
- [44] Sheng, Y., Nguyen, T. D., Veeraraghavan, G., Mermer, Ö., Wohlgenannt, M., Qiu, S. & Scherf, U. Hyperfine interaction and magnetoresistance in organic semiconductors. *Physical Review B* **74**, 045213 (2006).

- [45] Castro, F. A., Silva, G. B., Nueesch, F., Zuppiroli, L. & Graeff, C. F. O. Influence of doping on spin-dependent exciton formation in Alq₃-based OLEDs. *Organic Electronics* **8**, 249–255 (2007).
- [46] Hellerich, E., Chen, Y., Cai, M. & Shinar, J. Electroluminescence-detected magnetic resonance study of OLEDs containing a mixed N,N'-diphenyl-N,N'-bis(1-naphthylphenyl)-1,1'-biphenyl-4,4'-diamine (NPB)/tris(quinolinolate) Al (Alq₃) layer. *SPIE Proceedings* **7415**, 741522 (2009).
- [47] Li, G., Kim, C. H., Lane, P. A. & Shinar, J. Magnetic resonance studies of tris-(8-hydroxyquinoline) aluminum-based organic light-emitting devices. *Physical Review B* **69**, 165311 (2004).
- [48] Li, G. & Shinar, J. Electroluminescence- and electrically-detected magnetic resonance studies of spin one-half-polaron and singlet-exciton dynamics in multilayer small molecular organic light-emitting devices. *SPIE Proceedings* **4464**, 113–121 (2002).
- [49] Li, G., Shinar, J. & Jabbour, G. E. Electroluminescence-detected magnetic resonance studies of Pt octaethyl porphyrin-based phosphorescent organic light-emitting devices. *Physical Review B* **71**, 235211 (2005).
- [50] Son, D., Marumoto, K., Kizuka, T. & Shimoi, Y. Electron spin resonance of thin films of organic light-emitting material tris(8-hydroxyquinoline) aluminum doped by magnesium. *Synthetic Metals* **162**, 2451–2454 (2012).
- [51] Swanson, L. S., Shinar, J., Ding, Y. W. & Barton, T. J. Photoluminescence, electroluminescence, and optically detected magnetic resonance study of 2,5-dialkoxy derivatives of poly(p-phenyleneacetylene) (PPA) and PPA-based light-emitting diodes. *Synthetic Metals* **55**, 1–6 (1993).
- [52] Castro, F. A., Silva, G. B., Santos, L. F., Faria, R. M., Nüesch, F., Zuppiroli, L. & Graeff, C. F. O. Electrically detected magnetic resonance of organic and polymeric light emitting diodes. *Journal of Non-Crystalline Solids* **338-340**, 622–625 (2004).
- [53] Wang, F., Yang, C. G., Ehrenfreund, E. & Vardeny, Z. V. Spin dependent reactions of polaron pairs in PPV-based organic diodes. *Synthetic Metals* **160**, 297–302 (2010).
- [54] Yang, C. G., Ehrenfreund, E., Wang, F., Drori, T. & Vardeny, Z. V. Spin-dependent kinetics of polaron pairs in organic light-emitting diodes studied by electroluminescence detected magnetic resonance dynamics. *Physical Review B* **78**, 205312 (2008).
- [55] Behrends, J., Schnegg, A., Lips, K., Thomsen, E. A., Pandey, A. K., Samuel, I. D. W. & Keeble, D. J. Bipolaron formation in organic solar cells observed by pulsed electrically detected magnetic resonance. *Physical Review Letters* **105**, 176601 (2010).
- [56] Marumoto, K., Kato, M., Kondo, H., Kuroda, S., Greenham, N. C., Friend, R. H., Shimoi, Y. & Abe, S. Electron spin resonance and electron nu-

- clear double resonance of photogenerated polarons in polyfluorene and its fullerene composite. *Physical Review B* **79**, 245204 (2009). PRB.
- [57] Wohlgenannt, M. & Vardeny, Z. V. Photophysics properties of blue-emitting polymers. *Synthetic Metals* **125**, 55–63 (2001).
- [58] Kondakov, D. Y., Pawlik, T. D., Nichols, W. F. & Lenhart, W. C. Free-radical pathways in operational degradation of OLEDs. *Journal of the Society for Information Display* **16**, 37–46 (2008).
- [59] So, F. & Kondakov, D. OLEDs: Degradation mechanisms in small-molecule and polymer organic light-emitting diodes. *Advanced Materials* **22**, 3762–3777 (2010).
- [60] Pawlik, T. D., Kondakov, D. Y., Begley, W. J. & Young, R. H. Charge carriers and charge-transfer reactions in OLED devices studied by electron paramagnetic resonance. *Journal of the Society for Information Display* **18**, 277–284 (2010).
- [61] Gunn, J. Microwave oscillations of current in III–V semiconductors. *Solid State Communications* **1**, 88–91 (1963).
- [62] Krzystek, J., Sienkiewicz, A., Pardi, L. & Brunel, L. C. DPPH as a standard for high-field EPR. *Journal of Magnetic Resonance* **125**, 207–211 (1997). URL <http://adsabs.harvard.edu/abs/1997JMagR.125..207K>.
- [63] Pope, M., Kallmann, H. P. & Magnante, P. Electroluminescence in organic crystals. *The Journal of Chemical Physics* **38**, 2042–2043 (1963).
- [64] Helfrich, W. & Schneider, W. G. Recombination radiation in anthracene crystals. *Physical Review Letters* **14**, 229–231 (1965).
- [65] Tang, C. W. & VanSlyke, S. A. Organic electroluminescent diodes. *Applied Physics Letters* **51**, 913–915 (1987).
- [66] Burroughes, J. H., Bradley, D. D. C., Brown, A. R., Marks, R. N., Mackay, K., Friend, R. H., Burns, P. L. & Holmes, A. B. Light-emitting diodes based on conjugated polymers. *Nature* **347**, 539–541 (1990).
- [67] Wikipedia. OLED: Material Technologies (2013). URL http://en.wikipedia.org/wiki/OLED#Small_molecules.
- [68] Nicolai, H. T., Wetzelaer, G. A. H., Kuik, M., Kronemeijer, A. J., de Boer, B. & Blom, P. W. M. Space-charge-limited hole current in poly(9,9-dioctylfluorene) diodes. *Applied Physics Letters* **96**, 172107 (2010).
- [69] Chen, F.-C., Chen, Y.-S., Chien, S.-C., Liao, C.-H. & Chuang, S.-T. Suppression of phase separation through blending of electron transporting materials in polymer electrophosphorescent devices. *Journal of Luminescence* **131**, 565–569 (2010).
- [70] Tseng, S.-R., Li, S.-Y., Meng, H.-F., Yu, Y.-H., Yang, C.-M., Liao, H.-H., Horng, S.-F. & Hsu, C.-S. High-efficiency blue multilayer polymer light-emitting diode based on poly(9,9-dioctylfluorene). *Journal of Applied Physics* **101**, 084510 (2007).

- [71] Zaumseil, J., Donley, C., Kim, J.-S., Friend, R. & Sirringhaus, H. Efficient top-gate, ambipolar, light-emitting field-effect transistors based on a green-light-emitting polyfluorene. *Advanced Materials* **18**, 2708–2712 (2006).
- [72] Sasabe, H. & Kido, J. Multifunctional materials in high-performance OLEDs: Challenges for solid-state lighting. *Chemistry of Materials* **23**, 621–630 (2011).
- [73] Fu, H., Cheng, Y.-M., Chou, P.-T. & Chi, Y. Feeling blue? Blue phosphors for OLEDs. *Materials Today* **14**, 472–479.
- [74] Adachi, C., Kwong, R. C., Djurovich, P., Adamovich, V., Baldo, M. A., Thompson, M. E. & Forrest, S. R. Endothermic energy transfer: A mechanism for generating very efficient high-energy phosphorescent emission in organic materials. *Applied Physics Letters* **79**, 2082–2084 (2001).
- [75] Sigma-Aldrich Co. Phosphorescent host materials (2013). URL <http://www.sigmaaldrich.com/materials-science/material-science-products.html?TablePage=107232556>.
- [76] Li, L., Liu, J., Yu, Z. & Pei, Q. Highly efficient blue phosphorescent polymer light-emitting diodes by using interfacial modification. *Applied Physics Letters* **98**, 201110 (2011).
- [77] Mathai, M. K., Choong, V.-E., Choulis, S. A., Krummacher, B. & So, F. Highly efficient solution processed blue organic electrophosphorescence with 14 lm/W luminous efficacy. *Applied Physics Letters* **88**, 243512 (2006).
- [78] Campoy-Quiles, M., Sims, M., Etchegoin, P. G. & Bradley, D. D. C. Thickness-dependent thermal transition temperatures in thin conjugated polymer films. *Macromolecules* **39**, 7673–7680 (2006).
- [79] Crispin, A., Jonsson, A., Fahlman, M. & Salaneck, W. R. Aluminum–barium interfaces on some processable poly(p-phenylene vinylene) polymers studied by photoelectron spectroscopy. *The Journal of Chemical Physics* **115**, 5252–5257 (2001).
- [80] Nakamura, A., Tada, T., Mizukami, M. & Yagyu, S. Efficient electrophosphorescent polymer light-emitting devices using a Cs/Al cathode. *Applied Physics Letters* **84**, 130–132 (2004).
- [81] Oner, I., Stathatos, E. & Varlikli, C. White light electroluminescence by organic-inorganic heterostructures with CdSe quantum dots as red light emitters. *Advances in Optical Technologies* **2011**, 710628 (2011).
- [82] Morgado, J., Moons, E., Friend, R. & Cacialli, F. Optical and morphological investigations of non-homogeneity in polyfluorene blends. *Synthetic Metals* **124**, 63–66 (2001).
- [83] List, E., Guentner, R., Scanducci de Freitas, P. & Scherf, U. The effect of keto defect sites on the emission properties of polyfluorene-type materials. *Advanced Materials* **14**, 374–378 (2002).

- [84] Mark, P. & Helfrich, W. Space-charge-limited currents in organic crystals. *Journal of Applied Physics* **33**, 205–215 (1962).
- [85] Ma, L., Xie, Z., Liu, J., Yang, J., Cheng, Y., Wang, L. & Wang, F. Sodium hydroxide/aluminum bilayer cathode for enhancing the performance of blue polymer light-emitting diodes. *Applied Physics Letters* **87**, 163502 (2005).
- [86] Lane, P. A., Palilis, L. C., O'Brien, D. F., Giebeler, C., Cadby, A. J., Lidzey, D. G., Campbell, A. J., Blau, W. & Bradley, D. D. C. Origin of electrophosphorescence from a doped polymer light emitting diode. *Physical Review B* **63**, 235206 (2001).
- [87] Brodbeck, C. M. Investigations of g-value correlations associated with the $g = 4.3$ ESR signal of Fe^{3+} in glass. *Journal of Non-Crystalline Solids* **40**, 305–313 (1980).
- [88] Poole, J., C. P. *Electron Spin Resonance* (Wiley Interscience Publishers, 1967).
- [89] Hung, L. S., Tang, C. W. & Mason, M. G. Enhanced electron injection in organic electroluminescence devices using an Al/LiF electrode. *Applied Physics Letters* **70**, 152–154 (1997).
- [90] Lee, S.-Y., Paik, S., McCamey, D. R. & Boehme, C. Modulation frequency dependence of continuous-wave optically/electrically detected magnetic resonance. *Physical Review B* **86**, 115204 (2012).
- [91] Reineke, S. & Baldo, M. A. Recent progress in the understanding of exciton dynamics within phosphorescent OLEDs. *physica status solidi (a)* **209**, 2341–2353 (2012).